2013

Single-crystal metal oxides and supported metal nanoclusters as model catalyst sytems

Matthew C. Patterson
Louisiana State University and Agricultural and Mechanical College, mpatt15@tigers.lsu.edu

SINGLE-CRYSTAL METAL OXIDES AND SUPPORTED METAL NANOCLUSTERS AS MODEL CATALYST SYSTEMS

A Dissertation

Submitted to the Graduate Faculty of the
Louisiana State University and
Agricultural and Mechanical College
in partial fulfillment of the
requirements for the degree of
Doctor of Philosophy

in

The Department of Physics and Astronomy

by
Matthew C. Patterson
B.A., Rice University, 2007
April 2013

Acknowledgements

It is not possible to do science by yourself. Any worthwhile work can never exist in isolation from the people who came before you, the ones who worked next door to you, or those who come after you. So in that spirit, here are a few of the people without whom this work wouldn't have happened.

Phillip Sprunger and Richard Kurtz have been the best professors anyone could ask for. Experimental physics can often feel like trying to build a car while driving it, but working for Phil and Rich has at least shown that it's possible to do that without crashing. My other committee members, Erwin Poliakoff and Juana Moreno, have likewise given incredibly valuable feedback, support, and encouragement to go back and do better science when necessary. Fellow grad students Indrajith Senevirathne, Frank Womack, Fei Wang, Ziyu Zhang, and undergraduate ~~minions~~ workers Jordan Frick, Hunter McDaniel, Mark DiTusa, and many more LSU Physics colleagues have helped build the car while barreling down the road.

The portions of this work done at CAMD would not have been possible without the heroic efforts of their staff to keep the light on. In particular Orhan Kizilkaya and Eizi Morikawa have over the years taught me as many tricks about synchrotron radiation as I could keep up with, and it's really Orhan's enthusiasm for the work that made me think graduate school in physics might be a good thing to do in the first place.

Our collaborators through LSU's Superfund Research Center and Energy Frontier Research Center have consistently pushed the boundaries of science and pushed me to expand my own boundaries as a scientist. In no particular order, I thank Erwin Poliakoff, Barry Dellinger, Randall Hall, Slawo Lomnicki, Li Liu, Lucy Kiruri, and Chad Thibodeaux for teaching me how to speak chemistry, and Aravind Asthagiri, John Flake, Ye Xu, Xiaowa Nie,

and Evan Andrews for teaching me how to think engineering, or at least for being able to claim a nodding understanding of what people are talking about.

I'm not sure when I started this process that I ever thought life outside the lab would exist, but through a curious chain of circumstances I seem to have found myself thoroughly enmeshed in local and statewide progressive causes, and for that the thanks and blame go to all my partners in crime: Bruce Parker, Tucker Barry, Micah Caswell, Dylan Waguespack, Michael Beyer, Adrian Serio, Mary Catherine Roberts, Tim West, Frances Kelley, Dave Samuels, Carrie Wooten, Melissa Flournoy, state Rep. Patricia Haynes Smith, and on and on across the state. Speaking of doing the impossible, these folks do more good with no resources than almost anyone else you'll meet.

No acknowledgements are complete without the people who remind me that I'm not just a lab machine or political animal. To old friends Josh Hesterman, Kathleen Hesterman, Jason Altobelli, Dorothy Koveal, Austin Barclay, thanks for putting up with me for many years. To newer friends Sheri Thompson, Jeff Snell, Zac Thriffiley, Liz Eads, Sulakshana Thanvanthri, Clark McMillan, thanks for not running away screaming. And to all the Patterson and Zerangue (but not Zeringue) relatives across the world, thanks for indulging your crazy science cousin. And to my dad, Charles Patterson, for being very patient with me when I could have just as easily gotten an engineering degree and a job a very long time ago.

Finally, the one person who has supported me more than any other, Bobby Beaird. For years he's dealt with my weird cat Spot, my own neuroses, and all the slings and arrows of life with nary a complaint. I think I'll keep him! And I have been waiting my entire life to be able to make this joke: I can officially say that now, the two of us are a paradox.

Table of Contents

Abstract

We have investigated the morphology and electronic structure of two basic classes of systems: metal oxide surfaces that catalyze the formation of environmentally persistent free radicals (EPFRs) from aromatic precursors, and Au and Cu nanoparticles that may be suitable catalysts for the catalytic oxidation of CO or hydrogenation of CO_2.

First, we examine the adsorption behavior of phenol on rutile TiO_2(110) and ultrathin films of alumina prepared on a NiAl(110) substrate. Electron paramagnetic resonance studies show that exposure of both γ-alumina and titania powder to phenol at 250°C results in the formation of persistent phenoxyl radicals. EELS studies of phenol dosed on single-crystal titania and alumina show that phenol adsorbed at elevated temperature demonstrates a significantly narrower HOMO-LUMO gap than molecular phenol in the gas phase or physisorbed molecular phenol. Ultraviolet photoelectron spectroscopy shows direct evidence of charge transfer from high-temperature adsorbed phenol to electronic states of TiO_2(110) usually associated with the accumulation of charge at surface oxygen vacancies, providing direct evidence of a frequently-hypothesized radical formation mechanism.

Second, we deposit and characterize Au nanoparticles on the self-assembled hexagonal boron nitride "nanomesh" prepared on a Rh(111) substrate. STM studies show that at all levels of coverage, Au clusters almost always remain confined to the nanomesh "pores" and are restricted in size to < 3 nm diameter. XPS studies suggest that the resulting Au clusters are negatively charged, and for < 1 ML Au coverage, the electronic properties of most of the clusters formed are dominated by final-state effects that arise from the reduced dimensionality of the smallest clusters (one or two Au layers). A similar morphology for Au deposited on ZnO($10\bar{1}0$) has been previously observed; however, we find that the Au-ZnO interaction instead results in

positively charged clusters. Cu on ZnO($10\bar{1}0$) grows as three-dimensional clusters even at very small coverage and shows positive charging similar to Au. It is clear that catalytically relevant properties of supported metal nanoclusters are strongly influenced by interactions with the support, even if the cluster morphology is identical for particles on various different substrates.

Chapter 1: General Introduction

The idea of creating a "catalyst by design" is a current topic of fundamental interest to a wide variety of research fields that traditionally have existed in silos apart from each other. Almost any kind of chemical reaction of large-scale industrial interest is in some way enabled by a catalyst; if one is not necessary in order to make a reaction energetically favorable at all, it is almost always to one's economic and environmental advantage to find a way to make a particular reaction faster, cheaper, more efficient, or less polluting.

From the perspective of a physicist, the challenge in understanding catalytically active materials is not necessarily in the understanding of the particular reaction pathway it enables, but to understand the intrinsic properties of a particular material that enable it to catalyze a reaction of interest. That is, what about the morphology, charge state, occupation of electronic states, allowed electronic or vibrational excitations, or other features of a particular material make it suitable for a particular purpose? Or, to ask the question the other way around, if it is known that a particular set of materials properties (for example, metal nanoparticles of diameter <5 nm with a net negative charge) is desirable for a particular reaction, how can we prepare a system that is tailored to have that particular set of properties?

In the present work, we will actually ask both versions of that question – the first, by examining the reactivity of metal oxides towards the formation of environmentally persistent free radicals (EPFRs), and the second by attempting to prepare and characterize supported metal nanoparticles that have properties making them suitable for various catalytic processes. Surface science techniques involving the use of single-crystal materials and ideal ultra-high vacuum conditions can serve as a bridge between the totally idealized and artificial world of a computer simulation and the messy and complicated realm of real-world chemistry – while on the one

hand it enables us to control the growth and study of materials with much greater precision than "real-world" conditions could ever permit, on the other we are able to use actual materials as model systems for their real-world counterparts rather than relying on our ability to adequately simulate them.

The first problem of interest we will examine involves the formation of EPFRs through chemisorption on metal oxides. In general, a radical is just a molecule with an unpaired electron. Usually such species are extremely reactive and have lifetimes on the order of microseconds under environmental conditions, as it is extremely favorable for them to "rob" electrons from other molecules in order to pair off their unpaired electrons, often leading to a series of chain reactions. A prime example of this sort of process is the destruction of ozone in the upper atmosphere by chlorofluorocarbons such as CCl_3F; ultraviolet light exposure splits these into $CCl_2F\bullet$ and $Cl\bullet$, after which the $Cl\bullet$ undergoes a chain reaction with molecular ozone O_3 to generate O_2 and regenerate the chlorine radical to start the cycle again.

However, various processes within molecules may work to stabilize unpaired electrons and significantly extend radical lifetimes. In particular, aromatic organic radicals may be significantly longer-lived due to resonance. Radicals formed from many species of substituted benzenes are easily formed in aqueous solution and stabilized through resonance with π orbitals in the aromatic ring [1-3]. But in addition to their formation in solution, experimental studies have recently shown that such radicals may form from aromatic precursors in combustion reactions, and remain chemisorbed to particulate matter generated in such reactions. These fly ash-bound species have been implicated and studied as precursors to the formation of dioxins or furans, which are themselves known to be potent organic toxins [4-9].

These EPFRs in and of themselves, however, have been observed to have half-lives of hours or days, long enough to persist on particulate matter in the environment and ultimately find their way into biological tissues [10,11]. These species have been shown to generate reactive oxygen species in aqueous solutions [12,13], and introducing them to living tissue has been demonstrated to result in oxidative stress and cell death [14,15]. An understanding of the fundamental mechanism of the formation of these EPFRs is therefore of paramount importance in understanding environmental toxicity associated with airborne particulate matter.

It is known that various metal oxides make up a significant fraction of the inorganic components of fly ash [4,5,16]. SiO_2, which tends to be the dominant inorganic moiety, is inert for EPFR formation, but copper (II) oxide [10] and iron (III) oxide [11] nanoparticles supported on silica have been shown to promote the formation of EPFRs from aromatic precursors. CuO nanoparticles have been studied extensively with XANES, which has shown the formation of Cu(I) oxide after exposure to aromatic EPFR precursors at elevated temperatures [17,18]. Electron paramagnetic resonance spectroscopy has detected the formation of *F*-centers in iron (III) oxide after exposure to EPFR precursors, which is suggestive of a trapped unpaired electron in the oxide, implying a local reduction [11].

In this work, we take a surface science approach to the study of EPFR formation on metal oxides, using single-crystal materials as models for the particulate oxides that are known to be active for EPFR formation. We choose to examine the adsorption behavior of phenol, one of the simplest aromatic EPFR precursors, on rutile TiO_2(110) and single-crystal thin films of Al_2O_3 grown by oxidation of a NiAl(110) substrate. Alumina and titania both have significant abundance in the inorganic component of fly ash, so these studies are of significant importance to the understanding of the larger research problem. Additionally, these surfaces are well-studied

in the surface science literature [19,20] and have well-understood structural and electronic properties, so we are able to unambiguously determine properties that result from phenol chemisorption and EPFR formation. Because the key feature in the formation of an EPFR is the electron transfer from the precursor aromatic to the metal oxide, we focus on studying the electronic properties of the phenol/oxide systems above and below the threshold temperature that has been shown to be necessary for EPFR formation, in order to simultaneously elucidate changes in the electronic structure of both the adsorbed species and the substrate. We study low-lying electronic transitions and vibrational modes of these surfaces with EELS, and photoemission spectroscopy (both of the valence bands and of core-level peaks) is used to determine the occupied electronic states of these systems. The use of surface science techniques to examine these model systems permits us to examine in much greater detail the mechanisms that underlie radical formation under environmental conditions.

In the second half of this work, we prepare and characterize noble metal nanoclusters supported on novel materials. The catalytic activity of nanostructured materials is one of the most dramatic examples of the idea that "more is different" that underlies condensed matter physics. Bulk Au displays excellent ductility, malleability, and thermal and electrical conductivity, but is incredibly resistant to oxidation under atmospheric conditions, and in general is one of the least chemically reactive metals encountered in everyday life. But although bulk Au one of the least reactive (noblest) metals [21] in existence, it is by now well-established that Au clusters supported on various metal oxides show strong catalytic activity for a wide variety of oxidation reactions. In particular, the low-temperature oxidation of CO by molecular O_2 has been observed to occur for Au supported on first-row transition metal oxides [22-25]. The most dramatic and well-known factor known to influence the catalytic activity of such systems is the

size and shape of the Au nanoparticles, with catalytic properties virtually absent for particles larger than a few nm [23]. In addition to particle size, charge transfer between the support and Au clusters, particularly dependent on the dimensionality (0D, 2D, vs 3D), plays a key role in the adsorption of reactants and the selectivity of reactions [22,26-29]. Cluster nucleation and charge transfer are often facilitated by defects in the support [30-32]. These experimental findings underlie the key idea that it is not merely the existence of nanometer-sized Au clusters that brings about the remarkable properties of these systems: The choice of support exerts critical influence over the nucleation, morphology (size, shape, and distribution), charge state, and other properties of deposited metal clusters, and Au catalysts can almost never be considered in isolation of the support.

The deposition of Au onto patterned substrates has recently become a subject of interest for the preparation of well-dispersed Au nanoparticles with characteristics appropriate for catalysis. Simultaneously, we also desire a substrate that is not itself altered by reaction conditions, so that the nanoparticle catalysts maintain the properties that made them attractive in the first place. One avenue toward the goal of growing metal nanoparticles on patterned, inert substrates has been through metal deposition on nanostructured single-layer materials such as graphene or hexagonal boron nitride films on transition metal substrates [33-40] [41]. The intrinsic electronic and magnetic properties of graphene are themselves a hot topic of research [42], but for these purposes the property of interest is the tendency of graphene to form a “moiré” overlayer with periodicity of ~3 nm on various transition metal surfaces [34,37,38,43-45]. Various transition metals have been shown to form well-dispersed 3D clusters when deposited on this moiré structure [39], and Au has shown an interesting tendency to form extended 2D islands showing enhanced CO adsorption compared to the bare graphene [35].

Hexagonal boron nitride is isoelectronic with graphene, but rather than forming a moiré superstructure on surfaces such as Ru(0001) and Rh(111), shows instead a distinct "nanomesh" structure more resembling a honeycomb, with nearly flat hexagonal "pores" residing close to the surface separated by "wires" residing farther away [46-53]. The extent to which an *h*-BN monolayer exhibits this "nanomesh" superstructure rather than a commensurate (1x1) layer is governed by the degree of lattice mismatch between the *h*-BN and the metal surface, and the hybridization between electronic states in the *h*-BN and the metal. The *h*-BN nanomesh, featuring thermal stability, resistance to chemical etching, and a periodic array of "pores" to confine deposited metal nanoparticles is a seemingly perfect material to act as a model support for nanoparticle catalysts. Some experimental studies have taken place for Au/*h*-BN/Ru(0001) prepared by physical vapor deposition of Au [54,55], and Co/*h*-BN/Rh(111) prepared by buffer layer assisted growth of Co [56,57], but in general the field is wide open for studies of the nucleation and growth of metal nanoparticles suitable for catalytic applications using *h*-BN as a template.

In the present work, then, we make a detailed study of the nucleation and growth of Au nanoparticles supported on *h*-BN/Rh(111), starting with sub-monolayer coverages of Au at 115 K and proceeding to higher coverages deposited at 115 K and subsequently warmed to room temperature. We perform STM studies to determine the growth mode adopted by the clusters (layer-by-layer, confinement or lack thereof to the pores, degree of pore filling) as a function of temperature and coverage, and XPS measurements to elucidate the electronic structure and charge state of deposited Au and the underlying *h*-BN. As referenced above, control over the morphology, dimensionality, and charge of nanoclusters is essential to understanding and controlling their catalytic activity. We also extend our XPS studies to Au and Cu nanoclusters

supported on single-crystal ZnO($10\bar{1}0$) that have been previously examined with STM [58,59]. In general, we should expect to see that support effects play a profound role in determining various properties of the deposited metal clusters – even clusters of similar size and shape may exhibit very different electronic properties depending on their interaction with the support.

We begin with a brief introduction to the specific techniques and methodology used to prepare samples and perform various experiments in Chapter 2, "Methods." Chapter 3, "EPFR Formation from Phenol on TiO_2(110) and Ultrathin Al_2O_3/NiAl(110)," describes preliminary studies of low-level excitations for phenol on single-crystal titania and alumina, looking for electronic hallmarks of phenoxyl radical formation that correspond to radicals observed from electron paramagnetic resonance studies of aromatic precursors dosed on oxide powders. We extend and deepen these studies of phenol on TiO_2 in Chapter 4, "Photoemission Studies of Phenol Adsorption on TiO_2(110)," in which we examine in detail the occupied electronic states of the phenol/TiO_2(110) system under various dosing condition. Chapters 5 and 6, by contrast, examine not particular catalytic processes but the intrinsic properties of supported metal nanoclusters that may make them suitable for partiuclar reactions of interest. Chapter 5, "Nanoclusters for Catalysis: Au/*h*-BN/Rh(111)," presents studies of the morphology and core-level electronic structure of Au confined to the 3-nm-wide "pores" of a hexagonal boron nitride nanomesh grown on Rh(111), while Chapter 6, "Nanoclusters for Catalysis: Au/ ZnO($10\bar{1}0$), Cu/ ZnO($10\bar{1}0$)," extends prior studies of these two systems by providing core-level photoelectron spectroscopy to correlate trends in the observed charge state of Au and Cu nanoclusters with their previously observed morphology.

Chapter 2: Methods

2.1 Introduction

The experimental studies described in this work rely on our ability to prepare and characterize samples with well-defined, atomically flat surfaces with extremely low amounts of contamination, to dose them with precisely known quantities of ultra-pure gases or with physical vapor deposition sources of metals, and to perform various measurements. In this chapter, we describe the general techniques of sample preparation in ultra-high vacuum, the methods we use to study surface morphology (LEED and STM), and spectroscopic methods of investigating surface electronic structure (XPS, UPS, and EELS).

2.2 Principles of Ultra-High Vacuum (UHV)

Without some method of achieving UHV conditions, most surface science experiments would be impossible to conduct. There are two basic properties of gases that are essential for understanding why UHV conditions are hard to achieve but necessary for surface science: The mean free path of ideal gas molecules and the rate at which gas molecules impinge on a surface.

The kinetic theory of gases provides a convenient way to estimate the mean free path of an ideal non-interacting molecule. If we imagine a gas molecule to be a rigid sphere of diameter *d,* then the effective cross-section for collision of two identical gas molecules is a circle of area πd^2. In some time t, a gas molecule moving at average velocity v_{avg} will thus sweep out a cylinder of volume $\pi d^2 v_{avg} t$ in which collisions may occur. We can then define the mean free path λ for a gas molecule as the total distance a molecule can travel before undergoing a collision, for which we may write down an expression:

$$\lambda = \frac{v_{avg} t}{\pi d^2 v_{avg} t \rho} \qquad (2.1)$$

where ρ represents the total number of molecules per unit volume. Dimensionally, equation (2.1) gives units of distance per molecule.

However, (2.1) has implicitly assumed through its definition of the interaction volume $\pi d^2 v_{avg} t$ that only one molecule is moving and the molecules with which it collides are stationary. In fact, molecules in a gas at finite temperature are usually moving quite rapidly with respect to each other, so the average relative velocity is really the quantity that is needed to define the volume inside which molecules will interact in a given time. Fortunately, the Maxwell speed distribution of molecules in an ideal gas gives the simple relationship that the mean relative velocity of molecules in an ideal gas is just $\sqrt{2}v_{avg}$, which permits us to write (2.1) more accurately. Using this substitution and the ideal gas law to rewrite ρ in terms of measurable quantities as P/k_bT, we can thus define the mean free path as

$$\lambda = \frac{k_B T}{\sqrt{2}\pi d^2 P} \qquad (2.2)$$

where k_B is Boltzmann's constant, T is the temperature, and P is the gas pressure. Equation (2.2) permits us to estimate that at room temperature and atmospheric pressure, the mean free path of a typical gas molecule is on the order of nanometers, but as the pressure drops to the UHV region of 10^{-10} Torr, some 12 orders of magnitude lower, the mean free path increases to several kilometers. As UHV chambers are typically not on the order of kilometers long, this implies that gas molecules are vastly more likely to strike the walls of the chamber than they are to strike each other, and this has consequences for pumping – pumps that operate on the usual principles of viscous flow will fail to produce UHV.

Thus, to achieve UHV conditions (by which we typically mean pressures $<10^{-9}$ Torr), pumping setups are usually quite elaborate and take a long time to bring a chamber down from atmospheric pressure. Some sort of roughing pump is used to bring the chamber down from

atmosphere to 10^{-3} Torr, which is limited by the compression of gas into the pump. The next stage is usually a turbo pump, which is depicted in cutaway view in Figure 2.1. The angled turbine blades impart momentum to gas molecules that strike them, driving them farther down the stack and out of the chamber. The ultimate pressure of a turbo varies depending on the make of the pump, but they are typically able to maintain a system at 10^{-9} Torr or lower.

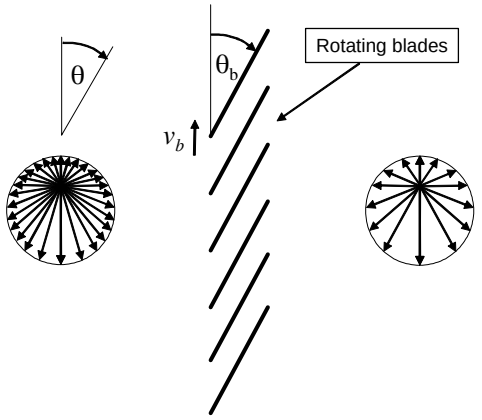

Figure 2.1 Cutaway view of turbo pump showing turbine blades rotating with speed v_b. Arrows indicate thermal velocity of gas molecules with respect to the blades on either side [60].

Many UHV systems also include ion pumps, which need no backing from a roughing pump and operate on a different principle entirely, as depicted in Figure 2.2. An ion pump applies a large potential difference (3-7 kV) across a small region between an anode and cathode. The large electric field at the cathode surface causes electrons to be emitted from the cathode. Applying a magnetic field as depicted in Figure 2.2 causes these electros to move in helical trajectories, increasing the probability they will collide with and ionize incoming gas molecules, which are subsequently accelerated towards the cathode by the electric field. This causes the cathode material (often titanium) to sputter off and ultimately deposit on the collector, which effectively traps gas molecules and prevents them from being released back to the gas phas into

the chamber. Ion pumps cannot be operated at high pressures due to plasma discharge (roughly $>10^{-3}$ Torr), but will easily maintain a system at 10^{-10} Torr or lower.

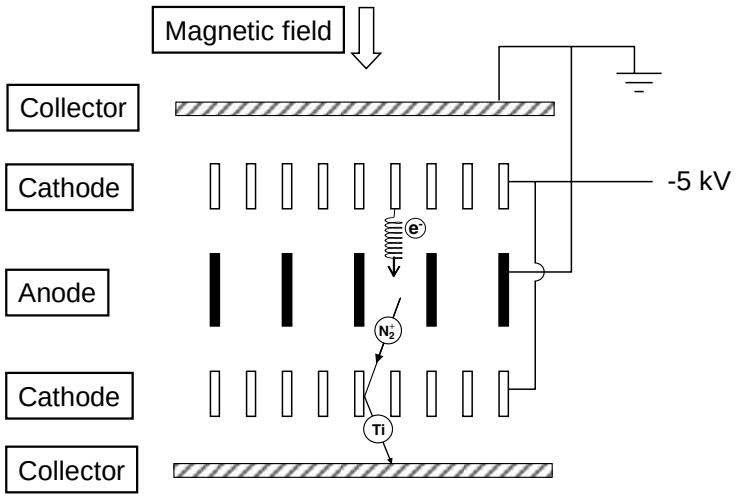

Figure 2.2 Schematic of triode ion pump [60].

As mentioned above, gas molecules at very low pressures are vastly more likely to interact with the walls of a chamber than with each other. Gases present in atmosphere tend to adsorb to the walls of a chamber and outgas slowly over time as the chamber is pumped down. In particular, water adsorbs readily to the stainless steel walls of a UHV chamber and does not pump easily. To speed the removal of unwanted residual gases from a chamber, it is usually necessary to heat the chamber to approximately 100-150°C for a number of hours in order to increase the desorption rate of unwanted species and pump them out of the system. The entire process of pumping down from atmosphere, baking, and cooling down can take 24-48 hours depending on the exact composition of the UHV system.

These elaborate procedures are necessary, however, in order to prepare and maintain clean and well-defined samples to study. If we again refer to the kinetic theory of gases, it can be calculated that the rate of molecules impinging on a given area is given by

$$R = \frac{P}{\sqrt{2\pi m k_B T}} \qquad (2.3)$$

where m is the molecular mass of the gas, and P, T, and k_B are as defined above [61]. For typical atmospheric gases such as H_2O, CO, CO_2, O_2, etc., equation 2.3 gives a rate on the order of 10^{14} – 10^{15} molecules/cm^2/s at room temperature and 10^{-6} Torr. In other words, at 10^{-6} Torr, molecules striking a surface will cover it at a density of approximately 10^{15} molecules/cm^2 in one second if all of them stick. This is comparable to the density of atoms in a surface plane. Thus, even if the probability that a given molecule will stick is much less than 1, the only way to ensure that a clean surface remains clean is to maintain a system at very low pressures so that the sticking rate is very low. For example, at 10^{-10} Torr, assuming a sticking probability of 1, it would take nearly three hours for the background gas to completely cover a clean surface with a contamination layer – long enough to do an experiment before cleaning a sample again.

Equation 2.3 also provides the basis for a useful experimental unit. We typically measure gas dosages in units of Langmuir, abbreviated L, where 1 L = 10^{-6} Torr • s. That is, multiplying the gas pressure and time of exposure gives the total dose in L. As sticking coefficients for many gases are much smaller than 1, typical gas exposures for our experiments can be on the order of 10^2 – 10^4 L.

To measure pressures in the UHV regime, we typically use hot filament ion gauges ("nude" Bayard-Alpert type gauges). These use a heated filament (thoriated tungsten is common) to emit electrons, which are accelerated toward a positively biased grid. Inside the grid, the electrons ionize background gas molecules, which are then attracted toward a negatively biased collector wire. The current measured at the collector is proportional to the number of ions created, which is proportional to the pressure in the chamber. Ion gauges have an upper limit of about 10^{-4} Torr to avoid burning the filaments, and a lower limit below 10^{-10} Torr (if the pressure

is this low, electrons will strike the grid before colliding with background gas, producing X-rays which cause noise in the collector).

Our samples are typically purchased from commercial vendors such as MaTecK GmbH or MTI Corp. They are aligned, cut, and polished to appropriate tolerances by the manufacturer, but after loading into UHV they typically require extensive cleaning cycles before a true atomically flat and pristine surface is available for experiments. We mount samples by attaching them to Ta or stainless steel plates before loading them into a chamber. They are cleaned of contamination through cycles of ion sputtering (typically 1.5 kV Ne^+ ions are used) and annealing to promote diffusion of atoms from the bulk to restore the surface plane. Our chambers typically feature sample manipulators that have a W filament mounted directly behind the sample holder, in order to enable both radiative heating and electron bombardment of the back of the sample (accomplished by biasing the sample several hundred volts positive of the filament). In this way we can heat samples as high as ~1200°C with little difficulty. Some samples require additional steps to restore a stoichiometric surface after sputtering and annealing (e.g. annealing TiO_2(110) in O_2 to restore surface oxygen vacancies), which are discussed in the appropriate chapters.

2.3 Sample Morphology and Surface Atomic Structure

The first question that is natural to ask about a sample after preparation is "what does it look like?" We cannot see atoms directly with visible light, but various techniques nonetheless permit us to determine the nanoscale structure of materials with great precision. The studies described in this work principally rely on LEED and STM, both of which we describe here.

2.3.1 Low Energy Electron Diffraction (LEED)

Low Energy Electron Diffraction (LEED) is an extremely surface-sensitive technique that exploits on the wave nature of electrons to generate diffraction patterns showing the symmetry of the topmost surface planes of a sample. Figure 2.3 gives a generic schematic of a LEED apparatus:

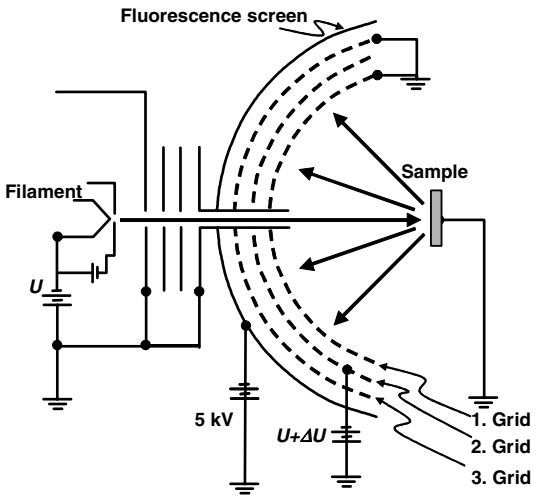

Figure 2.3 Schematic of LEED system [60].

Electrons emitted from a filament are focused and accelerated by the grids to kinetic energies of tens to hundreds of eV before striking a sample positioned at the center of the hemisphere described by the grids and screen. Electrons interacting with atoms at the surface diffract according to Bragg's law and backscatter, striking the fluorescent screen and producing a map of the reciprocal lattice of the topmost surface plane. Knowledge of the electron's de Broglie wavelength, given by

$$\lambda = \frac{h}{p} = \frac{h}{\sqrt{2mE}} \qquad (2.4)$$

where h is Planck's constant, p is the electron momentum, m is the electron mass, and E is the electron's kinetic energy, along with the diffraction angle of each bright spot on the screen, allows a user to calculate the spacings of periodic features at the surface from Bragg's law:

$$n\lambda = d \sin\theta \qquad (2.5)$$

Often these calculated distances correspond to atomic spacings, but not always – for example, Figure 2.4 below shows an image of contaminated Rh(111), with the principal spots from the Rh(111) lattice circled. The complex pattern surrounding the main spots arises from the superstructure created by the contaminants. (A superstructure with a larger real-space periodicity than the main atomic spacings will be imaged as having a correspondingly smaller reciprocal space periodicity.)

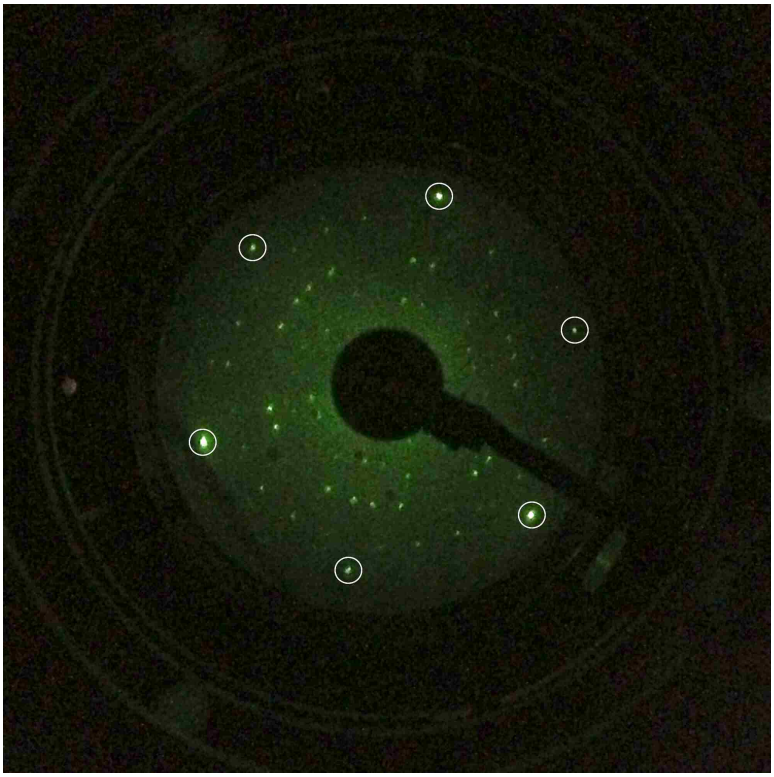

Figure 2.4 LEED pattern of contaminated Rh(111), with principal Rh(111) spots circled.

It is obvious that symmetry may be immediately inferred from simple observation of a LEED pattern. In addition to this, the quality of the pattern itself gives some indications about

the cleanliness of the sample and degree to which the surface is well-ordered. In general, the sharper the diffraction spots and the lower the diffuse background intensity, the flatter and more contamination-free the sample is.

Quantitative determination of atomic structure is much more difficult with LEED, and involves measuring the intensity of diffraction spots as a function of incident beam energy (LEED I-V) and fitting calculated models to the measured curves. This is both computationally intensive and very sensitive to the precise details of the chosen model due to the necessity of calculating multiple scattering events (dynamic scattering theory). A full description of LEED I-V is outside the scope of this work.

2.3.2 Scanning Tunneling Microscopy (STM)

STM is a technique that in the ideal case permits the direct observation in real space of the atomic structure of the topmost layer of a sample. In general, it relies on the phenomenon of quantum mechanical tunneling. Classically, if a particle with some defined kinetic energy is incident onto a barrier with potential energy greater than its kinetic energy (for example, a ball thrown at a wall that isn't moving fast enough to smash through), it will not penetrate the barrier. Quantum mechanics, however, permits solutions to the Schrödinger equation that allow there to be a nonzero probability for a particle to actually penetrate through the barrier and emerge on the other side. An STM exploits this property by bringing a sharp conductive tip very close (within angstroms) to the surface under investigation, scanning the tip in two dimensions over the surface, and measuring the current through the tip. Typically a feedback loop is used to maintain a constant current through the tip by continuously adjusting the height of the tip above the surface; the height of the tip above the surface as a function of lateral position then corresponds to the contours of the electron density at the surface, which is presumed to correspond to the

atomic positions. An STM can also work in constant height mode, in which the current through the tip is measured as a function of lateral position and the current map is read as a map of surface electron density. Figure 2.5 presents an extremely simplified schematic of this procedure.

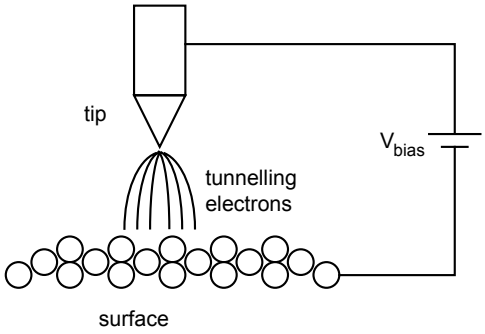

Figure 2.5 Cartoon schematic of basic STM experiment [62].

An expression for the tunneling current that makes some simple assumptions and still captures some relevant physics is given by Ref. [63]. Rigorously, first-order perturbation theory gives the tunneling current:

$$I = \frac{2\pi e}{\hbar}\sum_{\mu\nu} f(E_\mu)[1 - f(E_\nu + eV)]\left|M_{\mu\nu}\right|^2 \delta(E_\mu - E_\nu) \quad (2.6)$$

Here *f(E)* is the Fermi function, *V* the applied voltage, $M_{\mu\nu}$ the tunneling matrix element between states indexed by μ in the tip and ν in the surface (an expression can be written for this quantity that depends on the tip and sample wavefunctions), and $E_{\mu,\nu}$ the energy of the respective states in the absence of tunneling. Ref. [63] simplifies this expression by assuming that tunneling takes place at relatively low temperatures and relatively low voltages (generally valid for reasonable tunneling conditions), and that the tip's wave function is characterized by spherically symmetric functions with a relatively small (~few Å) radius of curvature (generally not necessarily valid, but not bad for tips approaching the "ideal" shape of one or relatively few atoms sharp). Without

presenting the detailed derivation of tunneling matrix elements, we summarize qualitatively the functional form of the tunneling current involving terms of experimental interest:

$$I \propto Vexp\left(-\frac{\sqrt{8m\varphi}}{\hbar}z\right)(terms \propto sample\ and\ tip\ DOS)(terms \propto tip\ geometry) \qquad (2.7)$$

Here ϕ really stands for the average of tip and sample work functions; it is possible to write out an explicit expression involving each separate work function but it is much more involved, and the functional dependence on tip-surface separation z is the same. For reasonable values of ϕ (around 4 eV), changing the tip height by 1 Å will change the tunneling current by roughly an order of magnitude. This is what gives STM its tremendous sensitivity to small variations in surface height. We see also qualitatively that the derivative *dI/dV* of the tunneling current carries information about the tip and sample density of states, such that mapping this quantity for a range of tunneling voltages near the Fermi energy may be used to determine features of the surface local density of states near the tip. (Particularly if the tip density of states is known or assumed to be flat over an energy region of interest, *dI/dV* spectroscopy is often used to probe the local density of states of the sample near the Fermi energy.) The tip geometry matters in the sense that a large, blunt tip will exhibit poorer resolution than a sharp tip with only one or a few atoms at the very end. Effectively, a large tip averages the tunneling current over a larger region of the surface due to electrons tunneling through many tip atoms at the same height z, destroying one's ability to resolve periodic lateral features on the order of atomic spacings.

The STM data presented in this work was entirely taken using an Omicron VT STM XA, which has been thoroughly described in the PhD thesis of previous group member Fei Wang [58]. We typically electrochemically etch homemade tips from 0.010" diameter tungsten wire using a recipe supplied by Omicron [62]; a tip etching device is reasonably simple to construct using a ring stand to hold and stabilize the tip wire, a ring-shaped counter-electrode made out of

Pt wire, a small Pyrex dish to hold just enough etching solution to immerse the tip wire and Pt electrode, and a variac to serve as an AC current source.

2.4 Spectroscopic Techniques

2.4.1 Photoelectron Spectroscopy

One of the early theoretical developments in the conceptual understanding of quantum mechanics was Einstein's explanation of the photoelectric effect. Originally observed by Hertz in 1887, Einstein was able to marry the experimentally observed features of the photoelectric effect (the onset of electron emission being dependent on frequency, not intensity, of incident light) with Planck's concept of energy quantization to arrive at a simple and profound relationship describing the kinetic energy *KE* of an electron emitted from a material after exposure to light of some frequency ν:

$$KE = h\nu - \Phi \qquad (2.8)$$

Φ is introduced as a quantity that describes the minimum amount of energy needed to remove an electron from a material, which is referred to as the material's work function. Incident light of energy greater than Φ can excite electrons no matter how intense; incident light of energy less than Φ can never excite electrons no matter how intense. Planck's constant *h* is what makes this a quantum theory, and what made this a revolutionary idea at the time it was introduced – energy from incident light cannot come in arbitrary increments; it must always come in quantities that are multiples of *h*.

Some more knowledge of atomic and condensed matter physics leads to a modification of equation 2.8:

$$KE = h\nu - BE - \Phi \qquad (2.9)$$

Here *BE* refers to the binding energy of a particular electron within a solid, which is a consequence of its interactions with nuclei and other electrons. This is the quantity we would like to measure in order to be able to say something about the behavior of electrons in a solid.

So in order to conduct an experiment to determine the binding energies of electrons within a material, we need a source of photons of known energy, some way of measuring the kinetic energies of photoelectrons, and some knowledge of "the work function." At first glance, the naïve assumption is that one has to know the *sample's* work function in order to properly do an experiment. However, this proves not to be the case, which is convenient for the experimentalist as it means an independent measurement of every single sample's work function is not required in order to get useful data. Figure 2.6 illustrates why this is so.

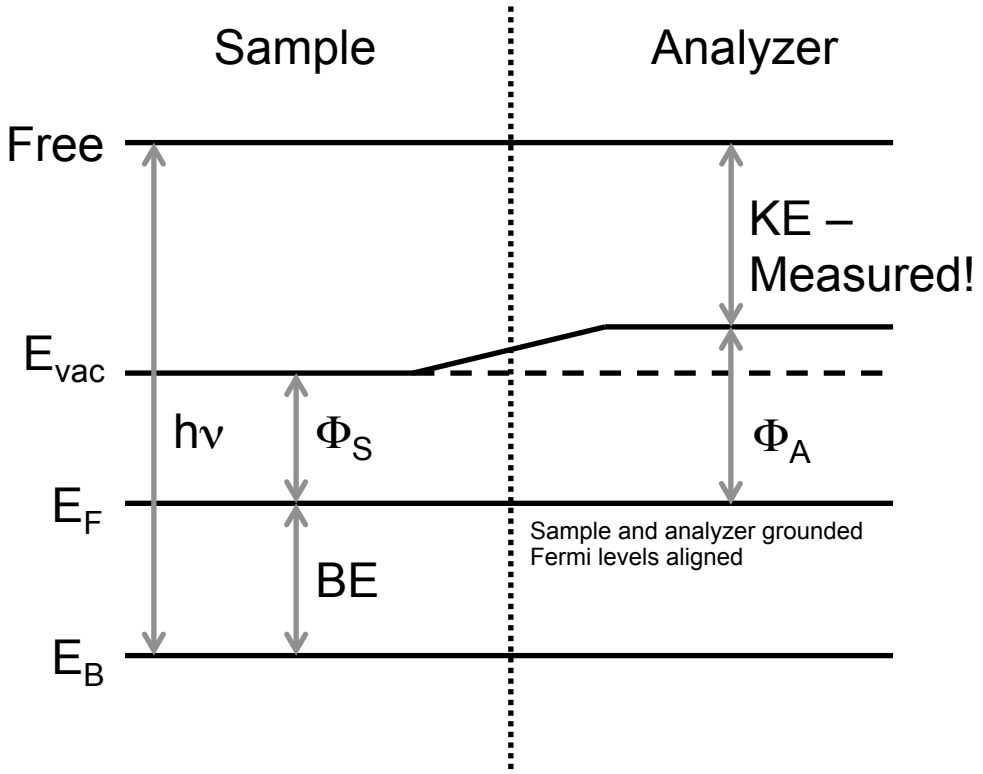

Figure 2.6 Schematic showing relevant energy scales in a generic photoemission experiment.

Figure 2.6 presents a generic energy level diagram showing the salient details of measurable energies in a photoemission experiment. On the left side of the vertical dashed line,

we label the total photon energy available as $h\nu$. The energy difference between the bound state we want to measure (E_B) and the sample's Fermi level E_F is what we call "the binding energy" *BE,* and the sample's work function (the energy required to excite the most shallowly bound electron to the vacuum level E_{vac}) is labeled as Φ_S. The analyzer, on the other hand, has work function Φ_A, and the final kinetic energy of the emitted electron is the energy the analyzer actually measures. Thus, if an electron in the solid originates in state E_B and can have a maximum energy of $h\nu$ imparted by a photon, we can count up from the bottom of the energy level diagram in Figure 2.6 to determine its final kinetic energy:

$$KE = h\nu - BE - \Phi_S - (\Phi_A - \Phi_S)$$

$$KE = h\nu - BE - \Phi_A \qquad (2.10)$$

Then the work function for the experimentalist to worry about is the analyzer's, not the sample's. This accounting relies on the assumption that the sample and analyzer Fermi levels are aligned, which is true for a grounded conducting sample. This is *not* a correct way to think about the experiment if there is a potential difference between the sample ground and analyzer ground – they both need to be tied to the same ground, and any sample charging will induce a potential difference that changes Figure 2.6 completely. Thus it can be challenging to work with samples that are not sufficiently conducting to replenish the charge lost during a photoemission experiment, as sample charging will result in measured binding energies that are greater than their actual value.

Quantum mechanically, we can describe the photoemission process as we would any other transition between quantum mechanical states, using Fermi's golden rule (derived from time-dependent perturbation theory) [64] to describe the probability of making a transition between some initial state to a continuum final state in response to the perturbation of a photon:

$$w_{if} \propto |\langle f|\mathcal{H}_{ext}|i\rangle|^2 \delta(\hbar\omega - E_f + E_i) \qquad (2.11)$$

$$\mathcal{H}_{ext} = \frac{e}{2mc}(\boldsymbol{A}\cdot\boldsymbol{p} + \boldsymbol{p}\cdot\boldsymbol{A}) \qquad (2.12)$$

Equations 2.11 and 2.12 taken together are quite general. The vector potential $\boldsymbol{A}$ and momentum $\boldsymbol{p}$ of the incident photon will vary depending on the incident photon energy, and the initial and final states $|i\rangle$ and $|f\rangle$ may be any pair of states (subject to selection rules depending on their symmetries and the symmetries of the perturbation Hamiltonian). When describing photoemission processes, we generally mean that the final state $|f\rangle$ is a free electron state outside the sample (as opposed to, for example, an X-ray an absorption process in which an electron in a bound state is excited to an unoccupied bound state within the sample).

The process by which photoelectrons are generated and escape a solid is generally thought of as consisting of three steps; though this is entirely qualitative and imprecise, it gives a conceptual understanding of features observed in a photoemission experiment [60]. The three steps are as follows: 1) Absorption of a photon to excite an electron from an occupied state into an unoccupied state (discussed above), 2) Propagation of the excited electron to the surface, and 3) Crossing the potential barrier at the surface and escaping the material.

The second step, propagation of the excited electron, is responsible for the inherently surface-sensitive nature of photoemission experiments. In general the mean free path of an excited electron depends on the electron's kinetic energy; Figure 2.7 depicts the calculated "universal" mean free path curve plotted against selected data for several elements for kinetic energies lower than 2 keV (note the logarithmic scales). It is evident that the mean free path of photoelectrons is quite short (< 30 Å) for reasonably accessible kinetic energies from a photoemission experiment between 10 – 2000 eV, and there is a broad minimum of about 5 Å between kinetic energies of 50-100 eV.

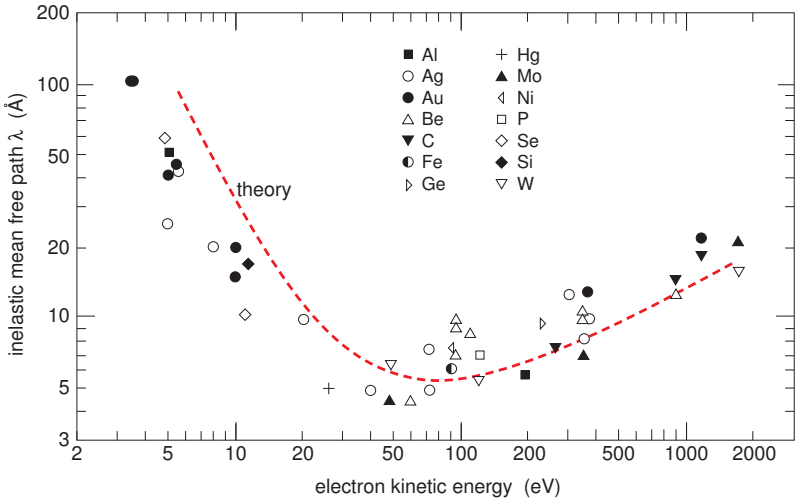

Figure 2.7 Universal mean free path curve [61]

Any electrons that are able to escape the surface before undergoing a scattering event thus will originate within at most a few tens of angstroms of the sample's surface. Electrons originating deeper in the material that undergo one or more scattering events and lose energy to various intrinsic excitations of a material (phonons, plasmons, etc) may still escape the sample, but they give rise to a broad secondary electron background rather than distinct peaks. Finally, the final step in the photoemission process involves crossing the potential barrier at the sample surface (see Figure 2.6); this step necessarily involves the electron losing some momentum as it crosses the barrier, so the component of an electron's momentum perpendicular to the surface is not conserved, and that component measured at the detector cannot be taken as an indication of what the electron's momentum must have been inside the sample. The component of the electron's momentum *parallel* to the surface is conserved, however, and its wave vector k can be determined easily:

$$k = \frac{p}{\hbar} = \frac{\sqrt{2m * KE}}{\hbar} \quad ; \quad k_{\parallel} = \frac{\sqrt{2m * KE}}{\hbar} \sin\theta \qquad (2.13)$$

where θ here is the angle between the sample normal and analyzer and KE is the measured electron kinetic energy. Angle-resolved photoemission spectroscopy, or ARPES, involves

carefully mapping the dispersion relationship *E(k)* for photoelectrons and thus developing a picture of the band structure near the surface. Although we only mention this technique in passing here, it has developed into an enormously rich and valuable technique for understanding the band structure of materials. Plummer and Eberhardt review the basics in Ref. [65], while Ref. [66] gives an overview of modern advanced techniques.

We perform core-level XPS measurements using an Omicron XM1000 monochromatic X-ray source in combination with a SPECS PHOIBOS 150 hemispherical analyzer. The XM1000 source, depicted in Figure 2.8, contains two separate filaments (long and short) to bombard with an aluminum anode with 15 keV electrons, producing characteristic X-rays, which are emitted such that they travel to the quartz crystal monochromator contained in the hemispherical steel housing (domed housing on the top of Figure 2.8), and are then diffracted such that only X-rays of the characteristic Al $K\alpha_1$ energy, 1486.6 eV, are focused to the sample position – bremsstrahlung and other satellite lines are diffracted elsewhere and ultimately absorbed by the thick stainless steel housing. The X-ray anode, monochromator, and sample plane lie on a Rowland circle of diameter 500 mm, with the entire system installed in the chamber and calibrated such that the focal position on the sample coincides with the focus of the SPECS hemispherical analyzer. The spot size focused on the sample for the short filament is approximately 1.5 x 2.5 mm, and for the long filament approximately 2.5 x 4.5 mm. The monochromator reduces the intrinsic linewidth of the incident X-rays to <300 meV and totally removes satellites, which permits high-resolution studies of core-level peaks, albeit at the expense of total flux. The ultimate combined system resolution of the XM1000 source and SPECS PHOIBOS 150 analyzer is approximately 0.6 eV for a core-level XPS peak (measured at the Ag $3d_{5/2}$ level), or ~0.3 eV measured from a metallic sample Fermi edge at low temperature

(after thermal broadening is deconvoluted). The typical procedure we use for fitting peaks to measured XPS data are described in Appendix B.

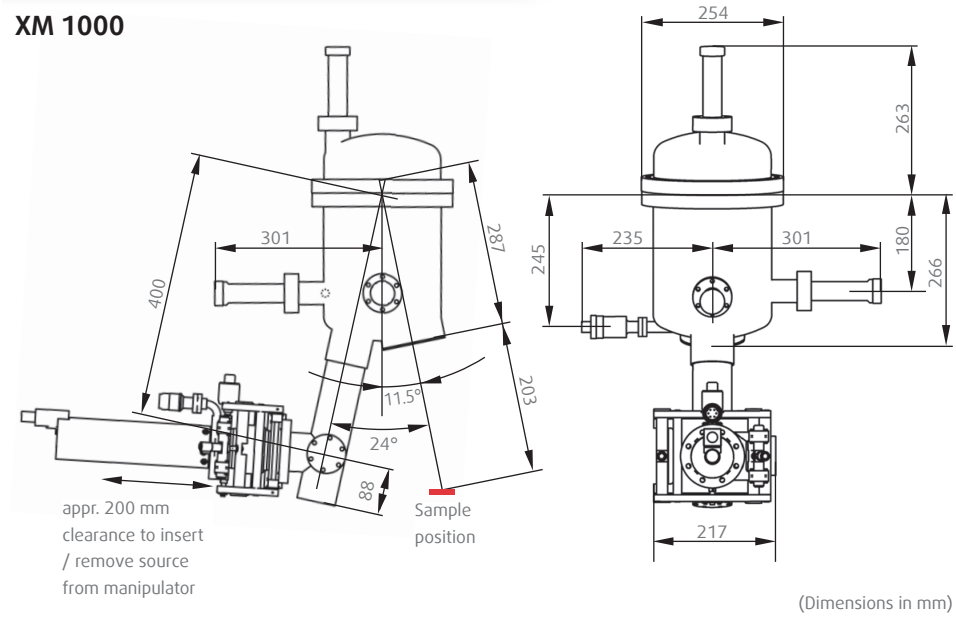

Figure 2.8 Schematic of Omicron XM1000 source [67].

Valence band photoemission data in this work were all taken at the 5-meter Toroidal Grating Monochromator (5m-TGM) beamline at LSU's Center for Advanced Microstructures and Devices (CAMD), depicted in Figure 2.9 below. Ref. [68] gives a brief review of the characteristics of synchrotron radiation and the history of dedicated synchrotron sources. Essentially, a synchrotron exploits the fact that accelerating charged particles radiate electromagnetic energy by accelerating electrons to high energies (~a few GeV) and forcing them to travel around a circular (approximately; actually polygonal with large magnets used to bend the beam around) ring, where they emit an intense beam of radiation around every bend. As electrons in a storage ring are traveling at relativistic speeds, we observe in the lab frame a very narrow cone of radiation of opening angle proportional to $\sim 1/\gamma$, where γ is the usual Lorentz factor – thus the angular spread of the photon beam is quite small. In brief, synchrotron radiation

is substantially brighter than laboratory sources by several orders of magnitude (particularly for X-rays), offers very high energy, momentum, and spatial resolution, is continuously tunable to any desired photon energy with suitable monochromators and insertion devices (it is possible for a synchrotron to generate photon energies from ~100 meV through tens or hundreds of keV, though not on the same beamline), and allows for the exploitation of its intrinsic polarization. However, synchrotrons are typically large, expensive user facilities, and experimental time is often limited or inconvenient. The work presented in this dissertation represents some of the first data taken during and after the commissioning of the 5m-TGM beamline, which is described more extensively in Ref. [69].

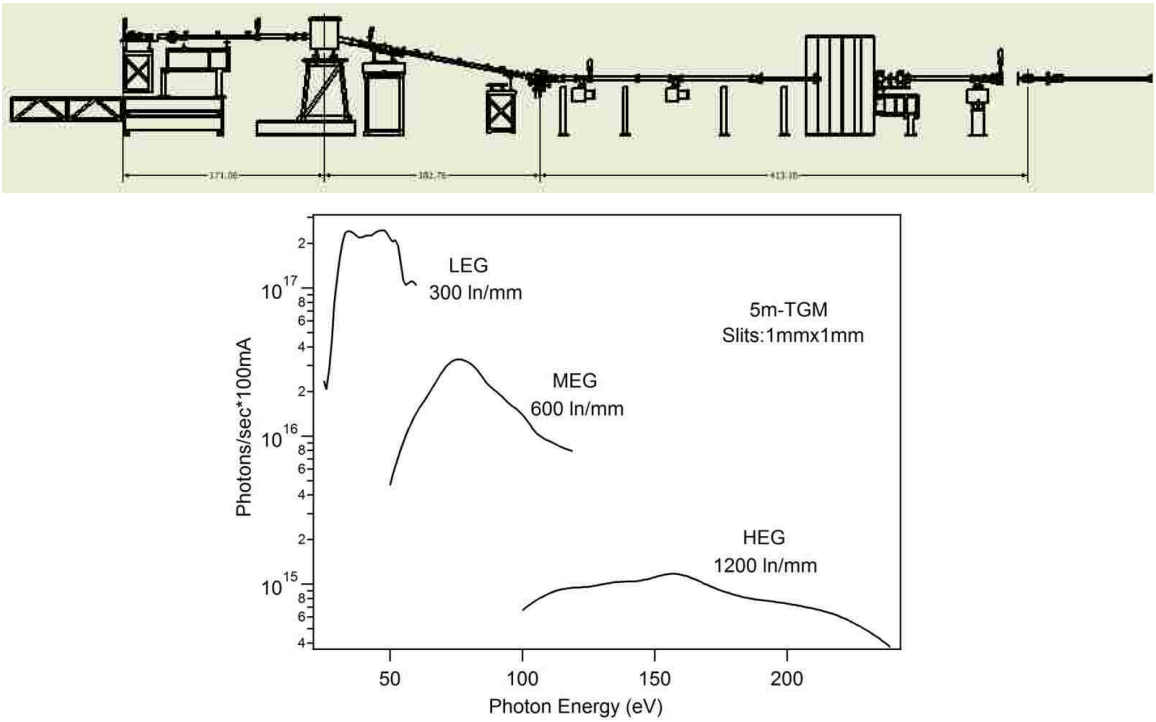

Figure 2.9 Schematic of 5m-TGM beamline and flux curves for each grating.

2.4.2 Electron Energy Loss Spectroscopy (EELS)

High Resolution Electron Energy Loss Spectroscopy (HREELS, or just EELS for short) is a powerful and exquisitely surface-sensitive tool for the study of physical and chemical properties of surfaces. The basic idea is simple: A monochromatic electron beam is incident on a

sample at some fixed angle. Electrons undergo various scattering events at the surface, some of which are inelastic processes in which electrons give up energy to various excitations at the surface (phonons, plasmons, vibrational modes of adsorbates, interband transitions, etc). The kinetic energy of the electrons scattered off the surface in a given direction is measured, and the resulting spectrum shows the intensity of electrons scattered off the surface as a function of energy loss. Generally the primary beam energies in an HREELS experiment are in the range of a few eV to tens of eV, and the energy losses measured on the order of meV to eV.

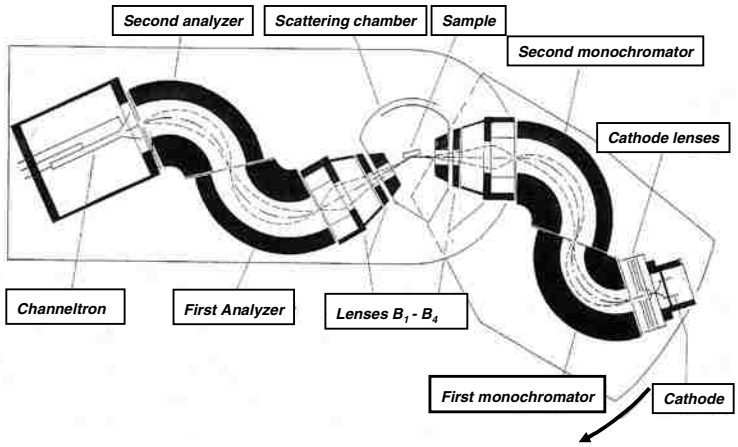

Figure 2.10 Schematic of EELS spectrometer, from Ref. [60].

We generally consider two different kinds of scattering mechanisms in a vibrational EELS experiment: Dipole scattering (scattering off long-range electric fields), and impact scattering (scattering off short-range atomic potentials). Ref. [60] contains full analyses of the theory of each; here we briefly review some relevant results. If we look at excitations at the Γ point of a sample in specular geometry (incident beam angle equal to exiting angle), in general (for reasonably conductive surfaces) we only observe energy loss peaks occurring via the dipole scattering mechanism when the corresponding modes have some dipole moment perpendicular to the surface, while parallel components are screened by their induced image dipoles. Modes only possessing a significant dipole moment parallel to the surface are only visible if the sample is

rotated with respect to the analyzer to an off-specular geometry. The intensity of purely dipole-active modes is sharply peaked about the specular direction, whereas impact scattering mechanisms display a much more complicated angular dependence. In general the intensity of peaks in the dipole scattering regime falls off as $\sim 1/\omega^2$, so peaks at higher frequency or energy are generally much less intense.

The LK2000 spectrometer used for experiments in our lab has been described in detail elsewhere [58]. The instrument provides a primary electron beam of energies from 1-240 eV; in this work we consistently operate at a primary beam energy of 7 eV when studying vibrational modes and 30 eV when studying higher-energy electronic excitations. Resolution is limited to ~8 meV with the 7 eV beam energy and ~20 meV with the 30 eV beam. The "standard position" of the spectrometer puts the incident and exiting angles of the beam at 30° with respect to the sample normal, but the sample may be rotated to off-specular geometries. The sample manipulator provides no heating, but can be cooled down to 90 K with liquid nitrogen.

Chapter 3: Persistent Free Radical Formation from Phenol on TiO_2(110) and Ultrathin Al_2O_3/NiAl(110)

3.1 Introduction

Recent experimental evidence has demonstrated the formation of environmentally persistent free radicals (EPFRs) associated with airborne particulate matter generated in combustion reactions. Laboratory studies have demonstrated the formation of EPFRs from substituted benzene precursors on systems such Cu(II) oxide and Fe(III) oxide supported on silica used as model fly ash, with half-lives of hours to days under ambient conditions [10,11], and virtually indefinite lifetimes under vacuum. *Ab initio* calculations attribute this stability and low reactivity to resonance stabilization including both carbon- and oxygen-centered radical structures [70]. Evidence of EPFRs has been found in soil samples from a Superfund wood treating site [71], and it has been demonstrated that EPFRs derived from the reaction of 2-monochlorophenol (2-MCP) on CuO/silica particles can form reactive oxygen species in aqueous solutions [12,13]. These EPFR-containing particles in turn have been demonstrated to lead to oxidative stress and increased cell death in both animal [14] and human [15] tissues.

Precursors such as phenol, 2-MCP, catechol, 1,2-dichlorobenzene, and other substituted benzenes have been proposed to form EPFRs over metal oxides at elevated temperatures (375-775 K) by a mechanism involving initial physisorption, elimination of H_2O or HCl to chemisorb to the metal ion, and electron transfer from the precursor to the metal oxide resulting in the reduction of the metal accompanied by EPFR formation [10].

This chapter has previously appeared as M. C. Patterson, N. D. Keilbart, L. W. Kiruri, C. A. Thibodeaux, S. Lomnicki, R. L. Kurtz, E. D. Poliakoff, B. Dellinger, and P. T. Sprunger, "EPFR formation from phenol adsorption on Al_2O_3 and TiO_2: EPR and EELS studies," Chemical Physics **422**, 277 (2013). It is reprinted by permission of Elsevier, per their Author Rights document (http://www.elsevier.com/journal-authors/author-rights-and-responsibilities): "Authors can use either their accepted author manuscript or final published article for… inclusion in a thesis or dissertation"

The formation of EPFRs from several aromatic precursors has been experimentally shown through electron paramagnetic resonance (EPR) spectroscopy on both CuO [10] and Fe_2O_3 [11] particles supported on silica. The EPR spectra of the dosed precursors show three common features – an F-center formed in the metal oxide after electron transfer from the precursor, and either a phenoxyl-type or semiquinone-type radical (see Figure 3.1 for a generic mechanism of phenoxyl radical formation). As further evidence of this proposed mechanism, Cu K-edge XANES spectroscopy of 2-MCP, chlorobenzene, and 1,2-dichlorobenzene adsorbed on micron-sized CuO supported on silica directly shows the reduction of Cu(II)O to a mixture of Cu(II), Cu(I), and small amounts of Cu(0) after exposure to these precursors at elevated temperature [17].

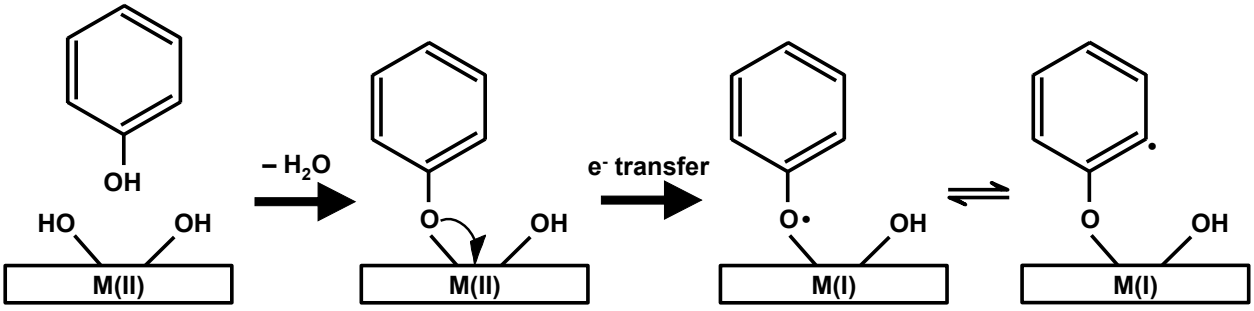

Figure 3.1 Schematic of radical formation from phenol adsorbed on a generic metal oxide.

In this chapter, we use EELS to investigate the mechanisms of EPFR formation from aromatic precursors on the surface well-characterized metal oxides of interest, specifically TiO_2 and Al_2O_3. Alumina is, along with silica, the highest concentration species in complex combustion systems [4,5,16], making it a system of interest along with copper oxides and other transition metal oxides. EPR studies clearly demonstrate the formation of EPFRs on these systems, while EELS studies on single-crystal alumina and TiO_2 guide a more fundamental understanding of the changes in the electronic structure and morphology of both the metal oxide

and the adsorbed molecule. The combination of techniques leads us toward a more detailed atomic-scale picture of the radical formation.

3.2. Experimental Methods

EELS experiments were performed using single-crystal rutile TiO_2(110) and ultrathin alumina grown by oxidizing single-crystal NiAl(110) using standard methods [72-74]. Experiments were performed in a UHV system with base pressure 10^{-10} Torr consisting of two chambers connected by a gate valve. The preparation chamber contained a sputter gun, leak valves to dose various gases, LEED, and a single-pass cylindrical mirror analyzer with coaxial electron gun for Auger electron spectroscopy measurements. The EELS chamber contained an LK Technologies LK2000 EELS spectrometer. Samples were checked for cleanliness by looking for clean and sharp LEED patterns and ensuring that Auger spectra showed no adventitious carbon or other species.

To dose our chosen EPFR precursor, solid phenol was loaded into Pyrex tubes attached to standard leak valves through a mini-conflat flange and purified by freeze-pump-thaw cycles, after which sublimated vapor was able to be dosed into the chamber. For high pressure (10^{-3} Torr) dosing, used for exposures of 10^6 Langmuir or greater (1 L = 10^{-6} Torr • s), samples were transferred into a separately pumped cell (base pressure ~$5x10^{-6}$ Torr) that could be isolated from the main chamber to avoid contaminating the UHV system. The cell was equipped with a sample stage that could be radiantly heated with a nearby glass-enclosed tungsten filament, with temperature measured by a type K thermocouple in contact with the sample stage. When dosing at elevated temperature, samples were first heated under vacuum and maintained at constant temperature for 10 minutes before dosing the desired quantity of gas. After dosing, we transferred the sample to the main chamber when the pressure in the cell dropped to ~10^{-5} Torr.

Vibrational and low-level electronic excitations of the clean and prepared surfaces were measured with high-resolution electron energy loss spectroscopy (HREELS) as described in Chapter 2. Experiments were performed in both specular (incident beam angle equal to exiting beam angle) and off-specular (incident beam angle different from exiting beam angle) in order to probe both dipole-active and Raman-active vibrational modes, respectively. Unless otherwise noted, EELS spectra displayed here were normalized to the height of the elastic peak, with offsets added for clarity.

3.3. Results and Discussion

3.3.1 EPR Studies of Phenol Adsorption on Particulate Titania and Alumina

Collaborators from the group of Barry Dellinger in the LSU Department of Chemistry performed electron paramagnetic resonance studies of phenol adsorption on titania and alumina powders to establish a baseline for radical formation and set the stage for EELS studies on the single-crystal materials. Adsorption of phenol on the surface of both γ-alumina and titania resulted in formation of surface species with a distinct observable paramagnetic signal, whose properties are depicted in Table 3.1 and Figure 3.2. Adsorption of phenol over γ-alumina produced a paramagnetic signal typical of that observed earlier for transition metal oxides, with a g-value of 2.0043 and peak width of 9.6 gauss. The broadness of the peak suggested the formation of a combination of more than one type of paramagnetic species. The mechanism of radical formation developed for metal oxides suggests formation of phenoxyl type radicals, in line with observed g-values. In contrast, adsorption of phenol on titania resulted in a very narrow signal with a peak width of ~5 gauss, indicative of the presence of a single type of radical species with a radical yield ~10 times higher than γ-alumina. The observed g-value of 2.0032 is characteristic of the radical with an electron present on a carbon atom with a nearby oxygen.

Table 3.1 EPR spectral characteristics of the signal measured upon exposure to phenol at 505 K.

Substrate	g-values	ΔH_{p-p} (Gauss)	Spins/gram
γ-alumina	2.0043	9.6	7.51×10^{16}
Titania	2.0032	4.92	6.00×10^{17}

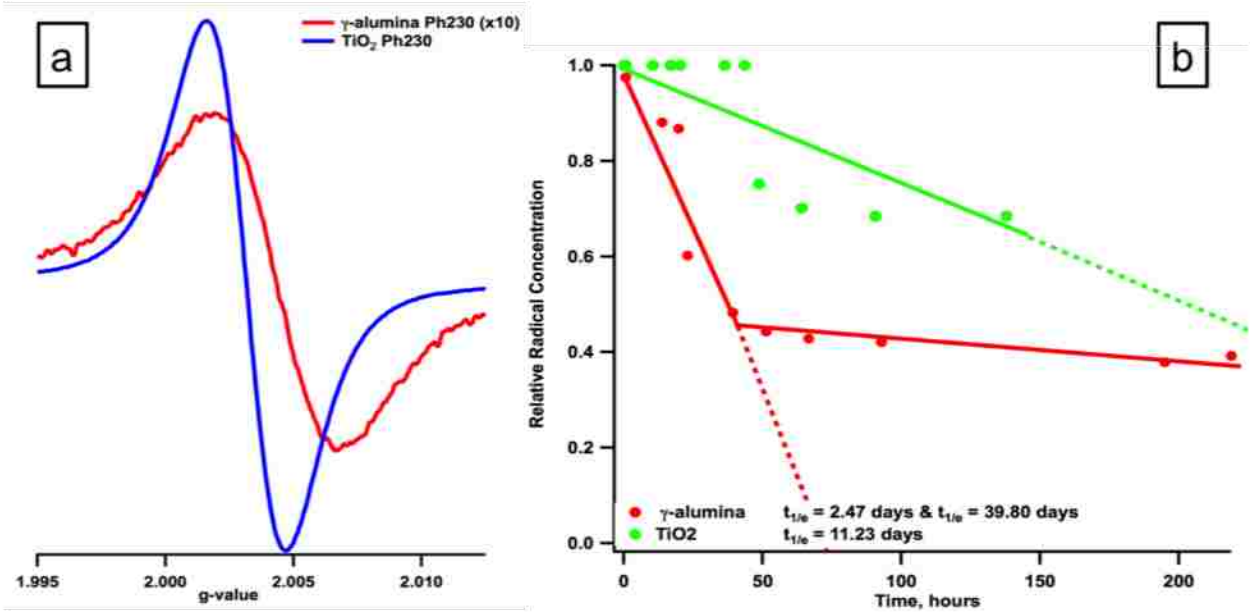

Figure 3.2 (a) EPR spectrum of phenol adsorbed on the surface of γ-alumina (red) and titania (blue); (b) Semi-log plot of the time decay of EPFRs from alumina (red) and titania (green).

A closer look at the decay curves of the EPFRs on both surfaces confirms the differences between the adsorption on titania and alumina surfaces. Though no significant peak width or g value change was detected upon the exposure of titania-bound radicals to air, two different decay behaviors were observed with a 1/e half-lives of 4.3 days and 57.4 days. Two explanations are plausible: i) two different radical species with a very similar spectral parameters are present, though with distinguishable decays or ii) two types of surface sites on alumina are responsible for stabilization of radicals. Since a relatively low g value was observed, the EPFR signal may have a contribution from a phenyl radical, resulting from the flat interaction of the aromatic ring with the titania surface and pπ-d electron back donation.

Radicals associated with the γ-alumina surface revealed two separate decay profiles: one with a 1/e half life of only ~2.5 days and a second with a 1/e half-life ~40 days. A correlation between the decay profiles and changes in g values and peak width could be observed. The ΔH_{p-p} gradually decreased from 9.6 to 8.7 gauss with a simultaneous increase in g-value from 2.0043 to 2.0046. This suggested a low g-value component of the paramagnetic signal was decaying relatively rapidly. The width of the remaining signal suggested a superposition of two species. Based on the shift in the g-value towards 2.0046, the species remaining on the surface were likely phenoxyl and even more persistent o-semiquinone type radicals. Semiquinone radicals result from a reaction between the chemisorbed phenoxyl radical and a surface lattice oxygen atom from the metal oxide [10,11]. Upon electron transfer between the newly formed surface bidentate species and the metal center, a semiquinone radical is formed.

3.3.2 EELS studies of Phenol Adsorption

3.3.2a Single-Crystal TiO_2(110)

In order to determine the changes in electronic structure of adsorbed phenol that indicate radical formation, it is essential to understand the electronic structure of the neutral phenol molecule. Figure 3.3 shows the electronic excitations characteristic of phenol adsorbed at low temperature on both partially reduced and fully oxidized TiO_2(110) The presence of oxygen vacancies on the clean TiO_2 surface is signaled by the loss peak at 0.8 eV (blue spectrum), and these vacancies can be filled, producing a fully stoichiometric TiO_2 surface, by dosing ~200 L of O_2 at room temperature after sputtering and annealing in vacuum (black spectrum). Surprisingly, after dosing phenol at 90 K, a clear difference between the reduced and oxidized TiO_2(110) surfaces is apparent. When phenol is dosed on the reduced surface, shown in the pink spectrum in Figure 3.3, we observe loss peaks consistent with those measured for physisorbed benzene on

alumina [75] and for phenol in the gas phase [76], which have been assigned to various allowed transitions between molecular orbitals. On the oxidized surface, shown in red, we see a large peak at lower energy (~ 3 eV) which does not appear in the gas phase data from the literature. In light of subsequent experimental investigations of this surface, however, we suspect that in fact the sample may not have maintained at 90 K throughout the entire measurement time, such that the measured spectrum is actually a sum of multilayer "phenol ice" and a single layer of phenol at room temperature. (Compare, for example, to the black spectrum in Figure 3.4 below, where phenol was dosed at 90 K and then deliberately warmed to room temperature.)

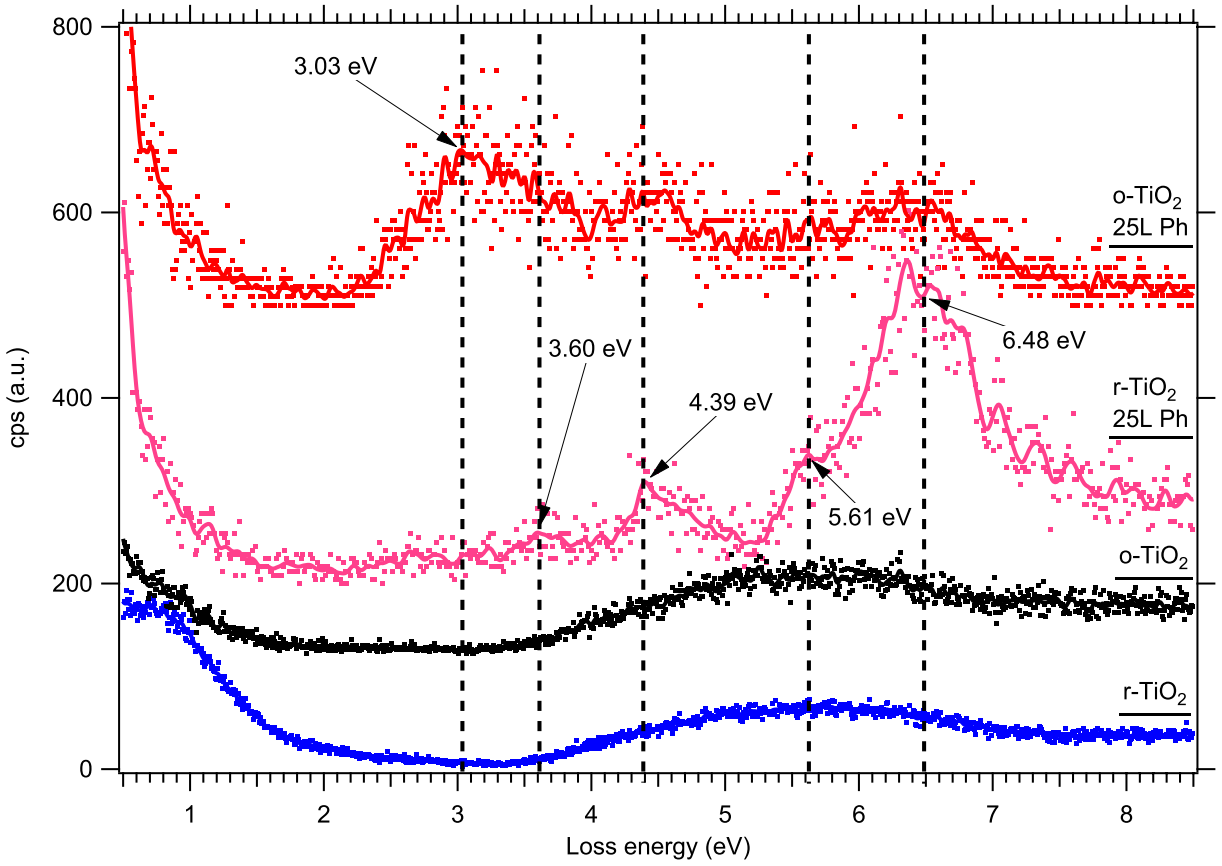

Figure 3.3 EELS data showing electronic excitations from clean and phenol-covered TiO_2(110) single crystals. From bottom to top, we show clean lightly reduced TiO_2(110), fully oxidized TiO_2(110), 25 L phenol on reduced TiO_2(110), and 25 L phenol on oxidized TiO_2(110). Phenol dosing, as well as each measurement, was done with the sample held at 90 K. The dots show the raw spectra (normalized to the elastic peak from r-TiO_2), and the solid curves show the data smoothed by a binomial algorithm. Vertical dashed lines are guides to the eye.

With a spectrum from physisorbed phenol on reduced TiO_2(110) as a guide, we can now examine the behavior of phenol deposited under EPFR-forming temperature and pressure conditions to determine any features in the electronic structure that may be hallmarks of the radical species. In Figure 3.4, we see few differences between phenol adsorbed at 90 K (pink) and the same sample allowed to warm to room temperature (black). The peak at 6.48 eV is still the most prominent peak in the spectrum (due to a π-π^* excitation from phenol), and the others from physisorbed phenol are still apparent, although in the room temperature sample they are convoluted with the usual features from the reduced TiO_2(110) – a weak peak due to oxygen vacancies at 0.8 eV and the onset of interband transitions starting at 3.4 eV. We attribute this to the desorption of all but a single layer of phenol when the sample is warmed to room temperature, so that EELS is able to probe features from both the adsorbate and substrate. Interestingly, a peak at about 2.85 eV appears in the room temperature spectrum which is absent from both the spectrum of clean TiO_2 and multilayer physisorbed phenol at 90 K. This appears at roughly the same position in energy as the anomalous peak observed from phenol adsorption at 90 K on fully oxidized TiO_2(110) in Figure 3.3 above, which may indicate some feature of the phenol-TiO_2 physisorption that is not shared by the bonding of subsequent phenol multilayers.

For our purposes, the most important data is the topmost spectrum in Figure 3.4 showing the results of 10^6 L (10^{-3} Torr, 1000 s) phenol exposed at 525 K. We now do not resolve many distinct peaks, but see a continuum of states starting at approximately 2.2 eV. The distinct peak we can see at 6.18 eV appears to correspond to the most intense allowed transition from the physisorbed phenol, which has been assigned to the $^1A_{1g} \rightarrow {}^1E_{1u}$ transition from gas phase data [76], but it is shifted 0.3 eV to lower energy with respect to the same peak measured from physisorbed phenol at both 90 K and 300 K. In combination with the EPR data shown in Figure

3.1 from phenol adsorption on particulate titania, it would appear that this shift in the π-π* excitation is the hallmark of the formation of a phenoxyl radical. We do not resolve additional peaks that might be indicative of two different radical species as suggested by Figure 3.2b, but this is consistent with the finding of a single g-value as observed in Figure 3.2a. Density functional calculations to elucidate the differences in molecular orbital structure between the phenol molecule and the phenoxyl radical are an ongoing topic of research.

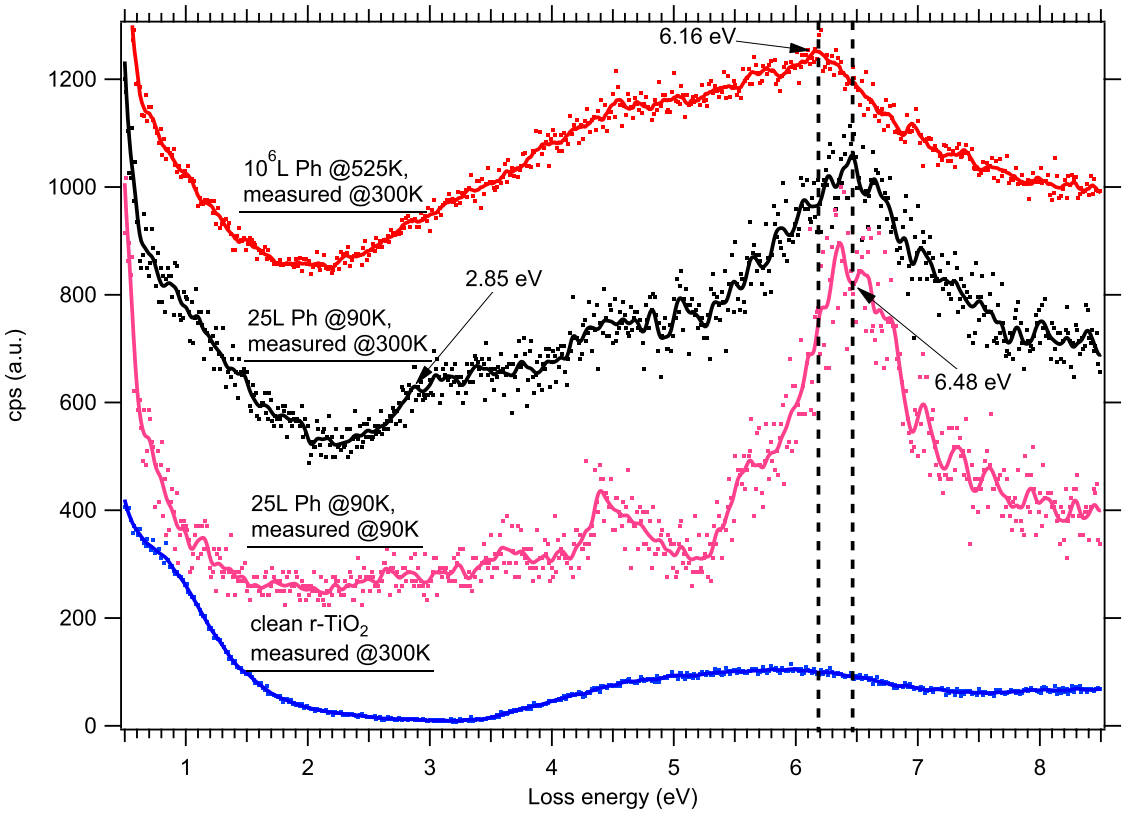

Figure 3.4 EELS data showing electronic excitations from phenol adsorbed on lightly reduced TiO_2(110) at a variety of dosing and measurement temperatures. From bottom to top, we show clean r-TiO_2(110) at 300 K, 25 L phenol on r-TiO_2(110) dosed and measured at 90 K, 25 L phenol on r-TiO_2(110) dosed at 90 K and allowed to warm to 300 K, and 10^6 L phenol dosed at 525 K and measured at 300 K. As above, dots show the raw data, and solid curves show the data smoothed by a binomial algorithm. Vertical dashed lines are guides to the eye.

Examining the low-energy region of the spectra (<1 eV loss energy) in Figure 3.4 provides a hint at what may be happening to the titania after the adsorption of phenol. The

spectrum from clean r-TiO_2(110) shows a loss peak at 0.8 eV characteristic of oxygen vacancies, as mentioned above. The spectrum of multilayer physisorbed phenol at 90 K shows much less intensity in this region, which is consistent with the lack of any observed interband transitions from titania in the spectrum – the EELS probes the multilayer adsorbate but does not "see" the substrate. In both the spectrum from physisorbed phenol at room temperature and the spectrum from 10^6 L phenol dosed at 525 K, we see substantial intensity in the spectrum below 2 eV. This may be indicative of electron transfer between the adsorbed phenol and titania, with the extra electron occupying the "defect" state that is visible in the clean spectrum. This is probed much

3.3.2b Ultrathin Al_2O_3 Grown on Single-Crystal NiAl(110)

We have similarly investigated the adsorption behavior of phenol on alumina at high temperature and pressure using EELS. Because bulk alumina is a wide band gap insulator, we prepare a model thin film of alumina by oxidizing a NiAl(110) crystal; using standard methods, this forms a well-ordered alumina film approximately 8 Å thick [72-74], which can be studied using electron spectroscopic methods that require conducting or semiconducting samples. The blue spectra in Figure 3.5 show electronic excitations typical of this ultrathin alumina film at room temperature, with a broad loss peak at approximately 1.6 eV due to defects in the film and the onset of allowed interband (band-gap) transitions starting at 7.5 eV. This is practically ideal, as it provides a window in which to observe electronic excitations from phenol, which typically lie in the region from 3 – 7 eV. It is apparent from Figure 3.5a that, after dosing 10^6 L phenol at 525 K as we did on TiO_2(110), we observe electronic losses in the alumina band gap region.

If we examine the appropriate energy region in more detail (Figure 3.5b), we observe the existence of a loss peak at 6.18 eV after the adsorption of 10^6 L phenol at 525 K, which agrees with the shifted π-π^* transition seen in the identical exposure of phenol on TiO_2(110) in Figure

3.4 above. We see also that the allowed interband transitions from the alumina thin film are no longer visible in the dosed sample, though whether this indicates an alteration in the alumina film itself or merely that it has been completely covered by phenol is not clear from these spectra alone. This new loss peak at 6.18 eV may again be attributed to the presence of a phenoxyl radical. We do not clearly resolve additional peaks that might indicate the additional presence of the o-semiquinone radical indicated by the EPR spectra presented in Figure 3.1, but this must be taken as a null result rather than a statement that no additional radical species are present. The lower radical yield over alumina shown in Figure 3.1 and Table 1 may explain our inability to resolve the presence of two unique species using EELS.

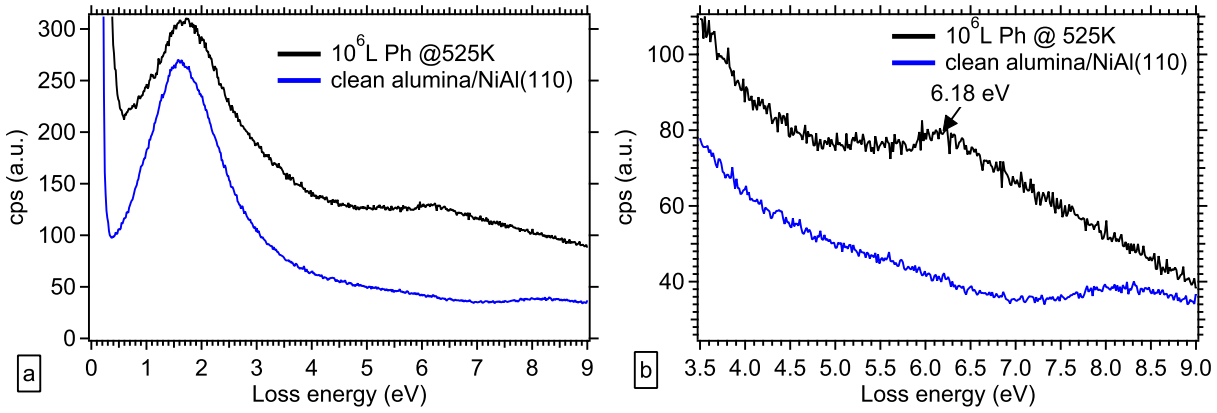

Figure 3.5 (a) EELS data showing electronic excitations on clean alumina/NiAl(110) measured at 300 K(blue, bottom) and 10^6 L phenol adsorbed on alumina/NiAl(110) at 525 K and measured at 300 K (black, top); (b) close-up of region from 3.5 – 9 eV in (a).

If we choose a lower incident beam energy and examine only the energy losses from 0-500 meV, we can resolve vibrational energy losses. The blue spectrum in Figure 3.6 shows the vibrational losses from the clean alumina thin film, with strong surface phonon loss peaks at 50, 80, and 103 meV typical of the alumina formed by oxidation of NiAl(110) [72]. After dosing phenol at 525 K (black spectrum), new features appear – several overlapping unresolved peaks between 60-100 meV, several overlapping unresolved peaks between 150-200 meV, and a strong

peak at 350 meV. With reference to infrared absorption data from liquid phenol, we assign the new peaks to the out-of-plane ring C-C bend and out-of-plane C-H bend (60-100 meV), the C-O stretch (~150 meV), the C-C ring stretch (several unresolved peaks between 170-200 meV), and the aromatic C-H stretch (strong peak at 350 meV) [77].

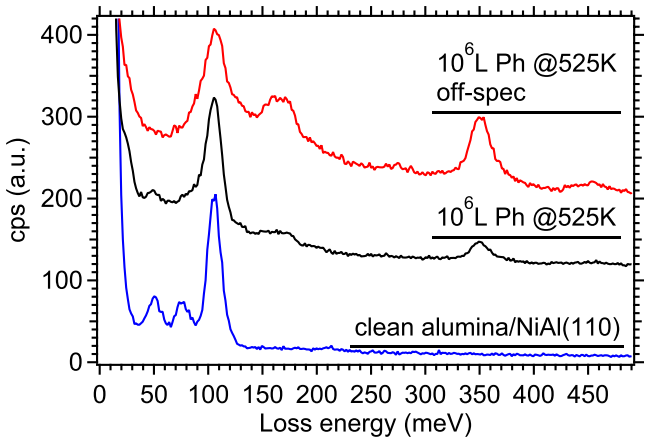

Figure 3.6 Vibrational EELS spectra of clean alumina/NiAl(110) (blue) and adsorption of 10^6 L phenol on alumina/NiAl(110) at 525 K, showing both on-specular (black) and off-specular (red) geometry. In this figure, spectra have been normalized to the height of the peak at 103 meV to more clearly show the relative intensity of vibrational peaks. All measurements were taken at room temperature.

An off-specular scan (red spectrum in Figure 3.6) shows enhanced intensity in several of the peaks, particularly the C-H stretch and the peaks between 160-200 meV, as well as a small broad peak centered at 450 meV which is usually indicative of an O-H stretch. The enhanced intensity in the peaks previously observed to be dipole-active indicates that the corresponding modes have some dipole moment parallel to the surface plane, suggesting some degree of tilt to the phenyl ring. The O-H stretching observed in the off-specular spectrum is likely due to slight surface contamination over the timescale of the experiment, as each spectrum takes approximately 12 hours to record in order to achieve an acceptable signal to noise ratio. The absence of a strong O-H peak in the on-specular data (which was taken earliest, while the sample

was presumably less contaminated) supports the proposed mechanism discussed earlier, showing chemisorption of the phenol through its hydroxyl substituent.

3.4. Conclusion

Correlating EELS measurements of electronic and vibrational structure with EPR determinations of radical species present on titania and alumina allow us to elucidate previously undetermined features of the phenoxyl radicals formed on these two oxides. With reference to the spectrum of electronic excitations from unperturbed phenol molecules physisorbed on TiO_2(110) at 90 K, we have shown a distinct shift of 0.3 eV toward lower energy in the most prominent π-π^* excitation from phenol after adsorption at 525 K, which is the temperature regime shown in the EPR experiments to form high yields of phenoxyl radicals over both TiO_2 and alumina. Given that we observe a peak at the same energy in the spectrum from phenol adsorbed at 525 K on alumina, we take this to be indicative of a unique change in the electronic structure of the phenoxyl radical versus the intact phenol molecule. EELS measurements alone do not permit us to determine the new molecular orbital structure of the phenoxyl radical, but the measurement of the shifted π-π^* transition provides a starting point for density functional calculations. Additional confirmation of chemisorption and radical formation comes from the vibrational EELS measurements of phenol on alumina, which show vibrational features of the phenol molecule save for the O-H stretching mode, which is only observed very weakly as a result of slight sample contamination, thus providing additional evidence in support of the generic mechanism of chemisorption through H_2O elimination. Neither the EPR nor the EELS measurements unambiguously point to the reduction of either metal oxide after radical formation, although there is some indication in the EELS data from phenol adsorbed on TiO_2 of the electrons transferred to the metal oxide from the phenol occupying the commonly observed

"defect" state. Photoelectron spectroscopy measurements that probe the core level electronic structure of the alumina and titania before and after phenoxyl radical formation should determine the oxidation state of the metal ion after the chemisorption of the radical. In the following chapter, we present valence band photoemission measurements of phenol adsorption on TiO_2 that specifically probe charge transfer between adsorbed phenol and the low-energy defect-induced electronic state as a function of adsorption temperature.

Chapter 4: Photoemission Studies of Phenol Adsorption on TiO_2(110)

4.1 Introduction

TiO_2 is a material of great technological interest for a variety of applications, from photocatalysis to self-cleaning surfaces to photovoltaics [58,78-82]. TiO_2 has a band gap of approximately 3.2 eV (depending on doping), so it intrinsically absorbs light in the ultraviolet portion of the spectrum. Much work on turning TiO_2 into a useful material for photovoltaics has thus focused on optimizing its absorption for visible light. Various approaches have been studied, including the embedding of metallic nanoclusters in a TiO_2 matrix to shift the intrinsic plasmon resonance of the nanoclusters to absorb at lower energies (e.g. in the range of 1-3 eV) [58], but one of the most prominent in the field of surface science has been the attempt to functionalize TiO_2 surfaces with various organic molecules which themselves absorb in the visible region. Thus, there has been considerable interest in the interaction of simple substituted benzenes such as phenol, catechol, and nitroaromatics with easily prepared TiO_2 surfaces [79,83-92], because these are construed to act as model systems for so-called dye-sensistized solar cells involving more complicated organic dyes.

Thus, although there is ample literature describing the interaction of simple aromatics with TiO_2 surfaces, the focus has been to determine whether the adsorption of these aromatics induces states within the TiO_2 band gap that could provide suitable absorption of visible light. This comes very close to dovetailing with the fundamental surface science needed to model persistent free radical formation on TiO_2, but the focus of existing photoemission studies has been mainly to determine the existence of induced band gap states at room temperature, and the detailed electronic structure of the aromatic molecules and the TiO_2 surface at elevated temperature has been neglected in experimental work. As the EPR spectroscopy referenced in

Chapter 3 has indicated that phenol adsorption on TiO_2 powders at elevated temperature generates persistent phenoxyl radicals, it is natural to extend the work presented in that chapter to photoemission studies to determine the changes in occupied electronic states of adsorbed phenol as a function of temperature.

In this Chapter, we perform photoemission measurements of phenol adsorbed at room temperature (inactive for radical formation) and 220°C (active for radical formation) on rutile TiO_2(110). Synchrotron photoemission experiments allow us to tune the incident photon energy to be as surface sensitive as possible, and allows us to exploit resonant effects to enhance or suppress the intensity of states from the underlying TiO_2, permitting us to determine to some extent the character (phenol-derived vs. Ti-derived) of new electronic states observed after adsorption. As a complement to our previous EELS studies, here we are able to study unambiguously the difference in occupied electronic states, as opposed to measuring excitations from occupied to unoccupied states. We also perform some preliminary core-level XPS studies to probe whether the adsorption of phenol is associated with a true "reduction" of Ti^{4+} to lower oxidation states, as in the proposed generic mechanism for persistent free radical formation, and has been observed directly in XANES studies of adsorption on copper oxides [9,17].

4.2 Experimental Methods

All experiments in this chapter were performed at the 5m TGM beamline at the Center for Advanced Microstructures and Devices (CAMD) in Baton Rouge, LA, described in Chapter 2. All spectra presented in this chapter have been normalized to a point on the background whose intensity solely derives from inelastic secondary electrons and not from any TiO_2 or adsorbate features in order to correct for variations in photon flux due to decaying storage ring current. (Deviations from this normalization scheme are mentioned as they occur.) The clean TiO_2(110)

surface was prepared by repeated cycles of 1.5 keV Ne^+ sputtering (30 min) and annealing to 700°C in 10^{-7} Torr O_2 (30 min) followed by cooling to room temperature in oxygen to prepare a surface free of oxygen vacancies.

Phenol was loaded into a pyrex tube attached to a standard leak valve and purified by freeze-pump-thaw cycles. High-pressure dosing (10^{-3} Torr, used for dosages of 10^6 Langmuir) was accomplished by transferring the sample into the load lock attached to the photoemission chamber, where it could be radiantly heated by means of a tungsten filament placed near the sample stage. Temperatures were measured by a type K thermocouple in contact with the sample mount. Lower doses of phenol (10^{-6} Torr or lower) were accomplished by opening the load lock to the photoemission chamber and dosing the sample in the manipulator used for photoemission measurements.

Measurements of low-level electronic excitations of the clean and dosed samples were accomplished in a second UHV system at LSU Physics consisting of a preparation chamber connected to an LK2000 EELS spectrometer, previously described in chapters 2 and 3. Sample dosing in the EELS was identical to that described in chapter 3. XPS measurements were carried out in the XPS chamber at LSU using the system described in Chapter 2; phenol dosing was accomplished using the chamber load lock as at CAMD.

4.3 Results and Discussion

Figure 4.1a depicts normal emission photoemission spectra from phenol dosed at various conditions on the stoichiometric TiO_2(110) surface. At 40 eV photon energy, two intense broad peaks are seen on the pristine surface centered around 5 and 8 eV, deriving from hybridized Ti 3*d*-O 2*p* π-bonding states and O 2*p*-Ti 3*d* σ-bonding states respectively. The intensity between 3 eV and the Fermi energy is nearly zero, indicating a nearly perfect, defect-free surface.

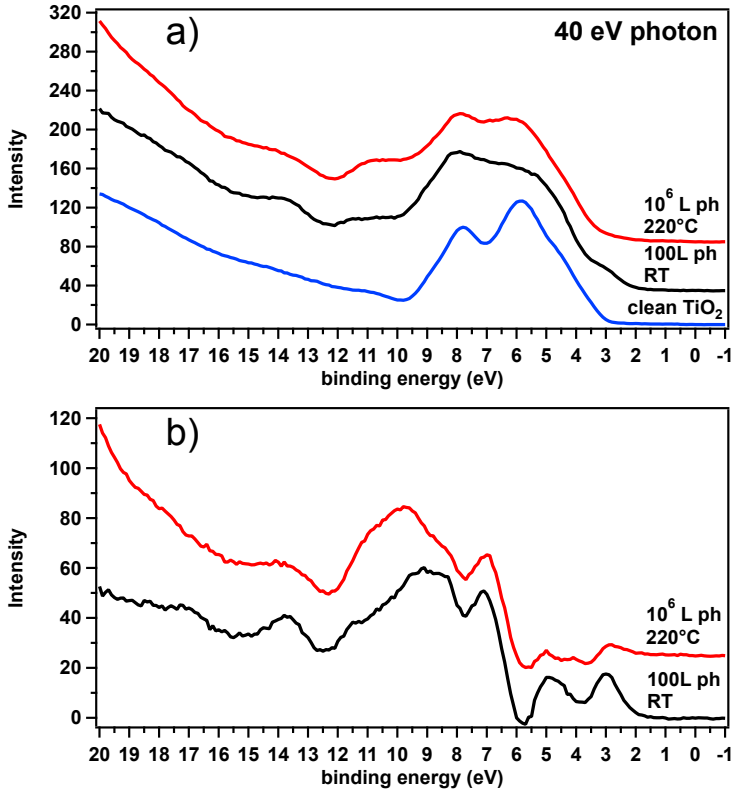

Figure 4.1 (a) Valence band photoemission spectra of clean TiO_2 (blue, bottom), 100 L phenol dosed at room temperature (black, middle), and 10^6 L phenol dosed at 220°C (red, top). Spectra have been shifted in energy to account for band bending as described in the text. (b) Difference spectra obtained from the data in (a). The procedure for generating difference spectra is described in the text. All spectra have been vertically offset for clarity.

Upon deposition of 100 L phenol at room temperature, a significant shoulder on the upper end of the valence band appears, centered at approximately 3 eV, and significant intensity with some structure appears in the region from 9-15 eV. Dosing 10^6 L phenol at 220°C results in a spectrum similar to the room temperature dose, but it is clear that the shoulder on the TiO_2 valence band has diminished, and subtle changes to the structure of the peaks between 6 and 10 eV have occurred. (To compensate for band bending, the room temperature-dosed spectrum was shifted 0.2 eV to higher binding energy, and the high temperature spectrum was shifted 0.2 eV to lower binding energy, aligning the upper edge of the respective valence bands with that of the clean spectra. In order to minimize potential complications from phenol-derived peaks

overlapping the valence band edge, this analysis was done using spectra taken at a high photon energy, minimizing the cross-section of adsorbate-derived peaks.)

Difference spectra allow us to study in more detail the phenol-derived peaks in the valence band spectra that overlap features from the underlying TiO_2. We have generated the difference spectra by scaling down the pristine spectrum by a factor of 0.65 prior to subtracting it from the respective dosed spectra; this accounts for the attenuation of emission from the substrate due to the phenol overlayer. (Qualitatively, one complete monolayer of phenol is approximately 5 Å thick assuming the plane of the phenyl ring is perpendicular to the TiO_2 surface; at the electron kinetic energies involved using an incident photon energy of 40 eV, this means that photoelectrons must travel an extra distance of approximately one mean free path length compared to photoemission from the bare titania surface, which should attenuate the photoemission spectrum from the substrate by roughly a factor of $1/e$, or ~65%.) As the total integrated intensity of the photoemission spectrum under both dosing conditions is roughly identical, it is reasonable to say that the substrate attenuation is the same under both conditions.

Figure 4.1b presents difference spectra for both dosing conditions. In the room temperature spectrum, the shoulder on the TiO_2 valence band is now revealed as a distinct peak at 3 eV, very similar to that reported for catechol on rutile TiO_2(110) though approximately 0.6 eV higher in binding energy [83,84]. A second peak at 5 eV of equal intensity is also revealed, and a high-intensity 7 eV peak is shown to be responsible for the observed "filling in" of the gap between the main TiO_2(110) valence band peaks in Figure 4.1a. The structure between 8 and 12 eV remains unresolved, but distinct peaks at 13.7 and 17 eV are made more distinct, again similar to peaks observed for catechol/TiO_2(110) though higher in binding energy. We presume these to be phenol σ orbitals.

The high-temperature difference spectrum reveals substantially lower intensity in the phenol HOMO peak and in the 5 eV peak, a potential indication that these states have been depopulated. Hints of a new state at 4 eV are seen, although it is possible that this is also present in the room temperature spectrum but hidden due to strong overlap with the peaks on either side. States between 8.5 and 12.5 eV are more intense with respect to the room temperature spectrum, although still unresolved, and the two peaks at 13.7 and 17 eV are significantly reduced in intensity and broadened out. The electronic structure of the adsorbed phenol is clearly altered as a function of deposition temperature.

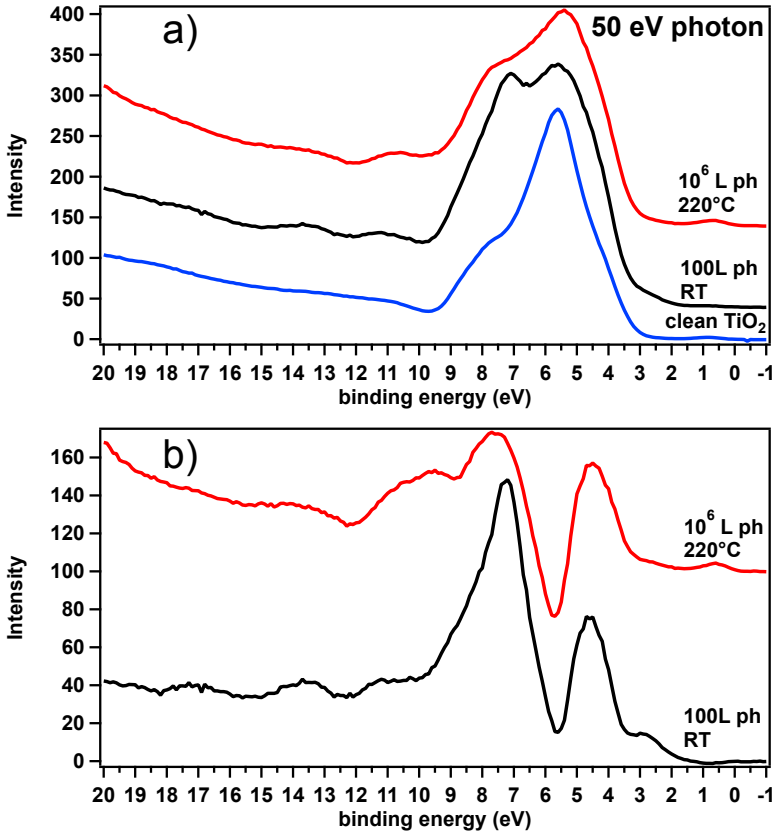

Figure 4.2 (a) Photoemission spectra (50 eV photon energy) of clean TiO_2 (blue, bottom), 100 L phenol dosed at room temperature (black, middle), and 10^6 L phenol dosed at 220°C (red, top). Spectra have been shifted to account for band bending as in Figure 4.1. (b) Difference spectra obtained from the data in (a). The procedure for generating difference spectra is identical to that in Figure 4.1. All spectra have been vertically offset for clarity.

Varying the incident photon energy allows us to exploit resonance effects to study more features of the interaction between adsorbed phenol and the TiO_2 surface. In Figure 4.2, we present spectra under the same conditions as Figure 4.1, but taken at a photon energy of 50 eV in order to exploit the resonant enhancement of Ti 3*d*-derived states [93,94] to more closely examine the phenol-induced changes in the substrate's electronic structure. Briefly, resonant photoemission is based on the constructive interference between two different excitation pathways that take the same initial state to the same final state. For example, electrons may be excited directly from a Ti 3*d* state, $3p^6 3d^n + h\nu \rightarrow 3p^6 3d^{n-1} + e^-$. Or they may be excited from a filled 3*p* state to an empty 3*d* state, followed by a 3*d* electron decaying to the 3*p* hole and another electron being emitted with the same kinetic energy: $3p^6 3d^n + h\nu \rightarrow [3p^5 3d^{n-1}]^* \rightarrow 3p^6 3d^{n-1} + e^-$.

Resonances will be observed when the incident photon energy approximately matches the separation between the energy levels involved in the resonant process ("approximate" because electron-electron interactions may modify the transition energy). The particular resonance illustrated described above has its onset at a photon energy of 47 eV and remains quite intense for a photon energy range of about 10 eV above the threshold [94]. This has the effect of enhancing the intensity of any photoemission peaks of Ti 3*d* character. Comparison with the data in Figure 4.1 taken below the resonant threshold facilitates an understanding of which states are purely adsorbate-derived, which are purely Ti-derived, and which may represent a mixture.

Figure 4.2a shows that all peaks exhibiting Ti 3*d* character are indeed greatly enhanced, resulting in a significant change in lineshape from the spectra in Figure 4.1. A small peak at 0.8 eV, usually attributed to the presence of surface oxygen vacancies [94,95], is now present in the clean spectrum (blue) and in the 220°C dose (red), but is absent after a room temperature dose (black). After both phenol doses, the additional peaks at binding energies 9.5 eV and higher are

again apparent, with roughly equal intensities as in the 40 eV spectra. It is evident again that dosing under either temperature condition contributes additional structure between approximately 6 and 10 eV, which we examine in more detail through the difference spectra in Figure 4.2b.

After subtracting the clean spectrum, the 100L room temperature dose shows the phenol HOMO at 3 eV as in the 40 eV data, but with reduced intensity due to the lower cross-section for phenol orbitals at higher photon energies. The broad peak between 3.5 and 5.5 eV (most likely several unresolved peaks, some of which are evident in the 40 eV difference spectra) is strongly enhanced a possible indication that the states involved here have some Ti 3*d* character enhanced through resonance. The peak at 7.2 eV is similarly enhanced. The remainder of the peaks at energies between 7 and 10 eV remain broad and unresolved, and the phenol-derived peaks at 13.7 and 17 eV are still apparent though diminished in intensity due to the reduced cross-section. Finally, we note that the peak at 0.8 eV usually attributed to surface oxygen vacancies is reduced in intensity with respect to the clean surface. Having already corrected for attenuation after dosing, we attribute this to the binding of phenol to surface oxygen vacancy sites, again similar to that observed from the room temperature adsorption of catechol on rutile TiO_2(110) [83,84].

The high-temperature difference spectrum at 50 eV differs from the room-temperature spectrum in ways qualitatively similar to those observed at 40 eV. Figure 4.3 shows a close-up of the highest energy range of the 50 eV difference spectra, with no offsets added, in order to facilitate direct comparison of the phenol HOMO and TiO_2 defect peaks. The phenol HOMO here is not visible as a distinct peak, the states between 8.5 and 12.5 eV are enhanced, and the higher binding energy peaks are attenuated nearly to the point of invisibility. Significantly, we find that the state at 0.8 eV is now enhanced with respect to the clean surface. The enhancement

of the defect state and depopulation of the phenol HOMO in the high-temperature dosed spectrum (open circles) is quite obvious compared to the room temperature dosed spectrum (open squares).

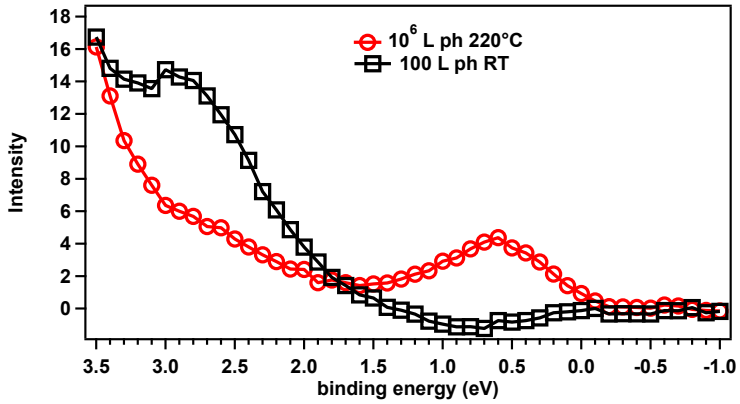

Figure 4.3 Close-up of phenol HOMO/oxygen vacancy peak region of the spectra in Figure 4.2. Here no vertical offset is added so that peak areas are more easily compared.

This is a hallmark of charge transfer from the adsorbed species to the electronic state giving rise to the defect peak. Similar effects have been observed in the growth of metal nanoparticles on rutile TiO_2(110) – sub-monolayer dosage of Ag is correlated with increasing intensity in the defect-related peak, which in combination with core-level XPS measurements implies the existence of positively charged Ag nanoclusters that have donated electrons to the defect-related electronic state in the substrate, whereas deposition of Au is associated with a depopulation of the defect state and the appearance of positively charged Au [96].

We then quite naturally would like to interrogate the mechanism behind this charge transfer, as it would seem odd for the process of transferring an electron to be thermally activated. One possible interpretation is implied by a computational study of phenol and larger aromatic molecules on clusters meant to represent the anatase TiO_2(101) surface [97]. The study found that the most favorable adsorption configuration for phenol on the cluster was actually as an *undissociated* phenol molecule, with a monodentate O_{phenol}-Ti bond and a hydrogen bond

from the OH_{phenol} to a nearby surface oxygen atom. In fact, of the bonding geometries studied, six different undissociated structures were found with more favorable adsorption energies than dissociated geometries. This makes some intuitive sense with experimental studies in which hydrogen bonding was found to control the dynamics of catechol on rutile TiO_2(110) at room temperature [86] – in this case, the catechol bonds in a bidentate configuration with both of its OH groups dissociated and the hydrogens bonded to neighboring surface oxygen atoms, but through a process of successive $O_{catechol}$-$Ti_{surface}$ bond breaking and H back-transferring from surface-bound OH groups, the catechol is able to "walk" over the surface. So it is at least plausible that at room temperature a phenol molecule might adsorb in a stable intact configuration, and raising the temperature has the effect of cleaving the O_{phenol}-H bond, which then facilitates electron transfer from phenol to the titania surface. This also may explain why the presumed σ orbital peaks that are distinct in photoemission spectra taken at room temperature are nearly absent after the high-temperature dose – these peaks arise from states with significant electron density on the OH_{phenol}, whose dissociation would certainly alter them.

High-resolution electron energy loss spectroscopy permits the study of vibrational modes and interband transitions of surfaces and adsorbates. Here, we compare our photoemission measurements to EELS data, some of which were presented in Chapter 3, to get a better understanding of what happens to the unoccupied states of phenol. Figure 4.4 shows electronic transitions of energy 0.5 – 9.0 eV from phenol ice (25 L phenol deposited at 90 K), clean TiO_2(110), and 10^6 L phenol deposited at 220°C, which is the condition that resulted in the increased intensity of the defect peak in photoemission and thus, presumably, resulted in electron transfer from the phenol.

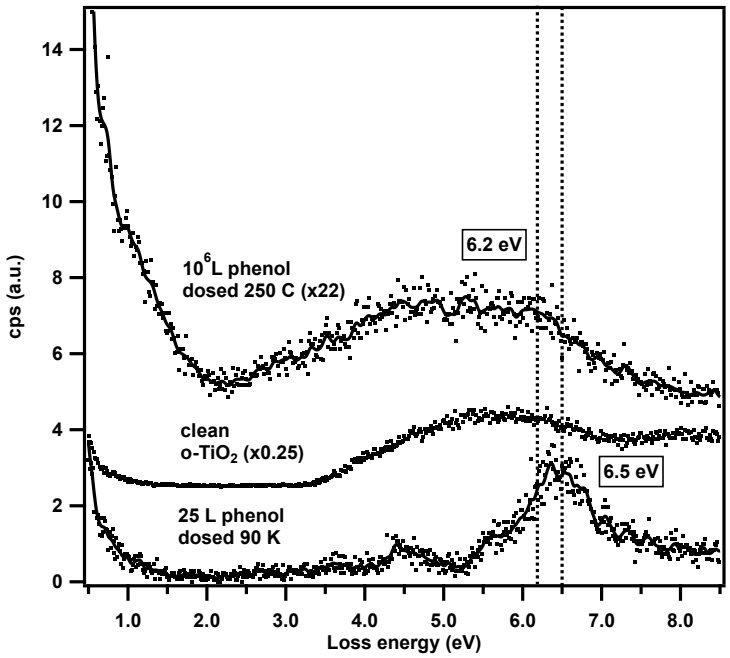

Figure 4.4. EELS spectra of low-level electronic excitations of phenol/oTiO2 and pure phenol ice. Dots are experimental data, solid lines show smoothed curves. Vertical dashed lines are guides to the eye.

The clean TiO_2(110) surface is characterized in EELS by an absence of intensity at energies lower than the bulk band gap, 3.2 eV, followed by an onset of a broad spectrum of allowed interband transitions. The presence of surface oxygen vacancies results in a broad loss feature centered around 1 eV, which arises from the same electronic state responsible for the loss peak observed in photoemission experiments. The absence of significant losses at low energies (save for vibrational losses of energy <500 meV) is an indication that the surface is almost completely free of vacancies before phenol dosage.

The spectrum of phenol ice is consistent with results in the literature from phenol in the gas phase – at 25 L exposure at 90 K, multilayer physisorption takes place and no TiO_2 features are observed in the spectrum. The three prominent visible peaks are all π-π^* transitions, and have previously been indexed from the gas phase data as arising from $^1A_{1g} \rightarrow {}^1B_{2u}$ (4.5 eV), $^1A_{1g} \rightarrow {}^1B_{1u}$ (5.6 eV), and $^1A_{1g} \rightarrow {}^1E_{1u}$ (6.5 eV) transitions, respectively.

After dosing the sample with 10^6 L phenol at 220°C, the observed EELS spectrum is radically different from either the pure phenol or pure TiO_2(110) at room temperature. Virtually no band gap is visible; there is instead a continuum of losses extending to about 2.0 eV, followed by a broad feature extending from 2.2 out to approximately 7.5 eV loss energy. The distinct peaks in the phenol spectrum at 4.5 and 6.5 eV are not readily apparent, but there are hints that the 6.5 eV peak is preserved, but shifted to lower energy by about 0.3 eV. This is consistent with our prior results for the same high-temperature dose of phenol on thin-film alumina presented in Chapter 3, which results in a distinct 6.2 eV loss peak.

The low-energy intensity in the high-temperature dosed sample (below 2.0 eV) is substantially similar to the spectrum observed on a TiO_2(110) surface that has been prepared by sputtering and vacuum annealing with no post-oxidation, resulting in a surface that is flat but relatively well-populated with oxygen vacancy sites; i.e. a surface that is partially reduced. Thus both the EELS and photoemission spectra after high-temperature phenol dosage point to an electron transfer from the phenol to the underlying titania, resulting in the population of electronic states associated with excess electron density at the surface – which is to say, they point to the formation of locally reduced Ti species and, by implication, a surface-bound phenoxyl radical.

Preliminary core-level photoemission studies, depicted in Figures 4.5 and 4.6, have also been undertaken to study the formation of reduced Ti species after phenol dosage. The Ti 2*p* doublet is quite sensitive to the oxidation state of Ti, with the Ti $2p_{3/2}$ peak shifting roughly 5 eV between metallic Ti^0 and Ti^{4+} as in TiO_2 [98-100]. The formation of reduced Ti species at the surface of a bulk TiO_2 sample should be apparent as a shoulder on the low binding energy side of the main TiO_2 peaks.

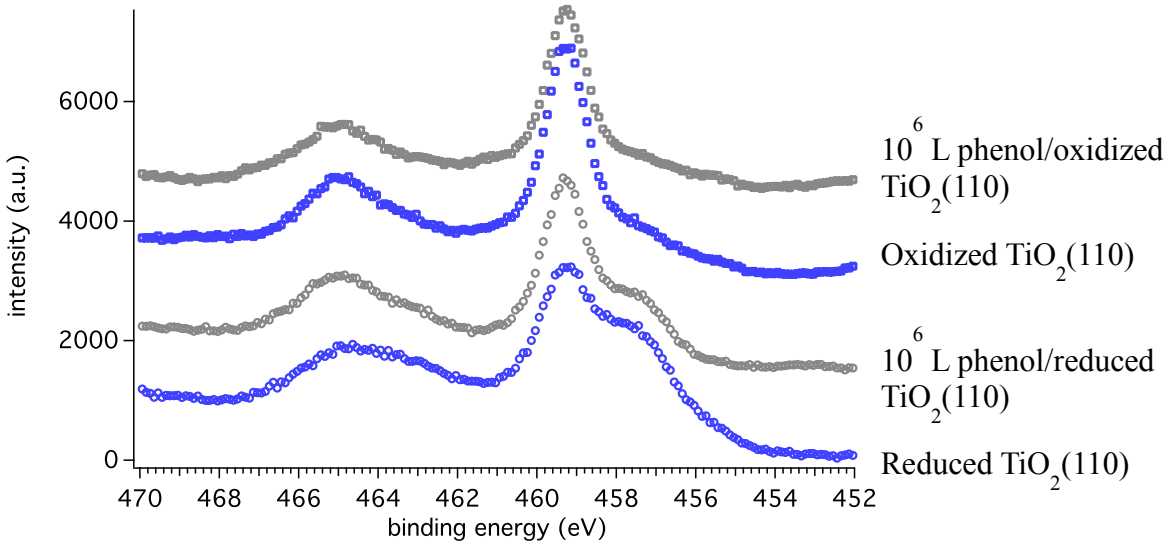

Figure 4.5 Ti 2*p* XPS results from phenol adsorption on various surface preparations of TiO_2(110). From bottom to top, the figure shows heavily reduced TiO_2(110) without phenol (blue circles), reduced TiO_2 after dosing 10^6 L phenol at RT (gray circles), oxidized TiO_2(110) (blue squares), and oxidized TiO_2 after dosing 10^6 L phenol at RT (gray squares). Spectra are normalized so that the height of the Ti^{4+} $2p_{3/2}$ peak at 459.3 eV above a zero point on the low binding energy side is the same in all spectra. Backgrounds have not been subtracted, but offsets have been added for clarity.

Figure 4.5 shows Ti 2*p* XPS taken under various conditions. As an extreme limit, we initially prepared a TiO_2 sample by sputtering without subsequent annealing to restore surface oxygen vacancies, resulting in a severely reduced sample exhibiting a broad shoulder on the main Ti^{4+} peak containing contributions from several different oxidation states of reduced titania (bottom spectrum, blue circles, in Figure 4.5). After dosing with 10^6 L phenol at room temperature, we find that the shoulder intensity decreases significantly (gray circles in Figure 4.5), which actually indicates sample *oxidation* rather reduction. Performing the same dosing on a sample that was initially sputtered and annealed in oxygen, resulting in a surface substantially free of oxygen vacancies (blue squares in Figure 4.5) resulted in a substantially unchanged sample after the same phenol dose at room temperature (gray squares in Figure 4.5).

To describe this effect in a semiquantitative fashion, we can fit peaks to the experimental spectra in Figure 4.5 according to the procedure described in Ref. [100]. In brief, we fit Voigt-

type peaks (see Appendix B for peak fitting details) at the known binding energies for Ti^{4+} $2p_{3/2}$ (459.3 eV) and Ti^{0} $2p_{3/2}$ (454.1 eV), and fit evenly spaced peaks at 1.3 eV intervals in between these two values to account for the Ti^{3+}, Ti^{2+}, and Ti^{+} oxidation states that are present in a heavily reduced sample. The even spacing of peaks is merely an approximation based on the different formal charges assigned to each Ti ion, and should not be viewed as a representation of the "true" chemical shifts or peak shapes arising from each oxidation state – but at minimum, this is a useful way to divide up the area in the XPS spectrum that does not come from Ti^{4+} ions at the surface or in the bulk. We then plot the ratios of the intensity of each interpolated peak to that of the Ti^{4+} $2p_{3/2}$ peak in each spectrum, by way of normalization; the results are displayed in Figure 4.6 to illustrate the trend.

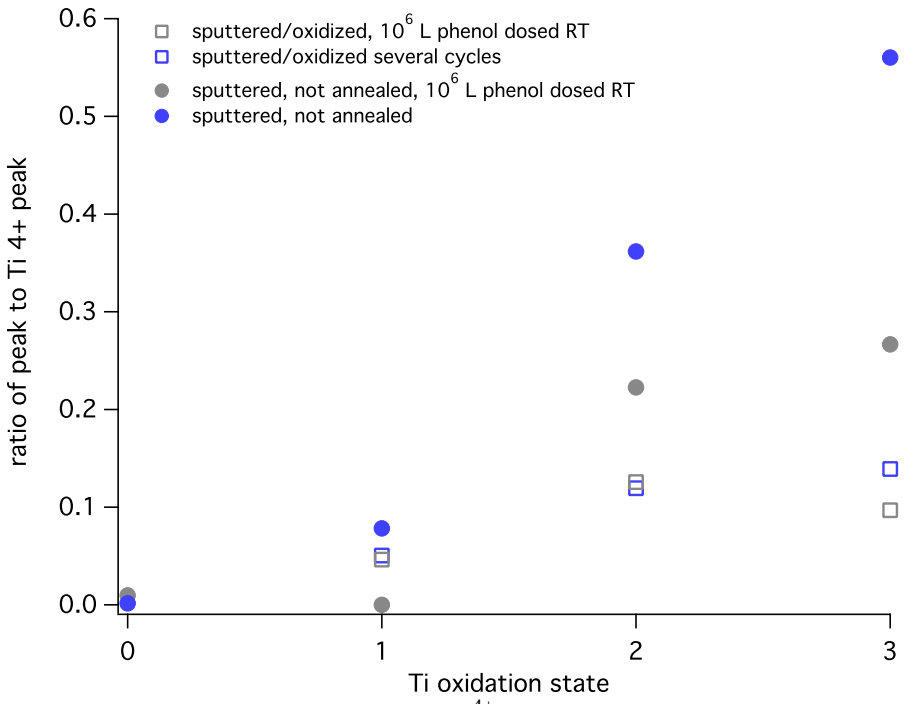

Figure 4.6 Ratios of lower oxidation states to Ti^{4+} for each spectrum plotted in Figure 4.5.

On the reduced sample, the intensity of the fitted peaks corresponding to Ti^{3+}, Ti^{2+}, and Ti^{1+} are all significantly larger, by roughly a factor of 2, relative to the Ti^{4+} peak in the undosed sample (blue circles in Figure 4.6) than in the dosed sample (gray circles). Similarly, one can see

in the oxidized sample that the Ti^{3+} intensity does drop noticeably between the undosed sample (blue squares) and the dosed sample (gray squares), although the effect is quite small.

To determine what organic species are present after dosing, we examine the C 1*s* level. In both C 1*s* spectra in Figure 4.7, we observe peaks seemingly characteristic of a phenol or phenoxy species – one peak for the five equivalent ring carbons (binding energies of 285.2 eV from the reduced sample, 285.0 eV from the oxidized sample), and one for the single carbon on the ring bound to oxygen (binding energy 286.4 eV on both). We also, however, observe a weak shoulder at a lower binding energy (approximately 282.9 eV in the reduced sample, 282.7 eV in the oxidized) and what appear to be several peaks at higher binding energies (roughly 289.4 eV and 290.7 eV in the oxidized sample; approximately the same energies, although poorly resolved in the reduced sample) that do not seem to correspond to the π-π*shakeup from intact phenol.

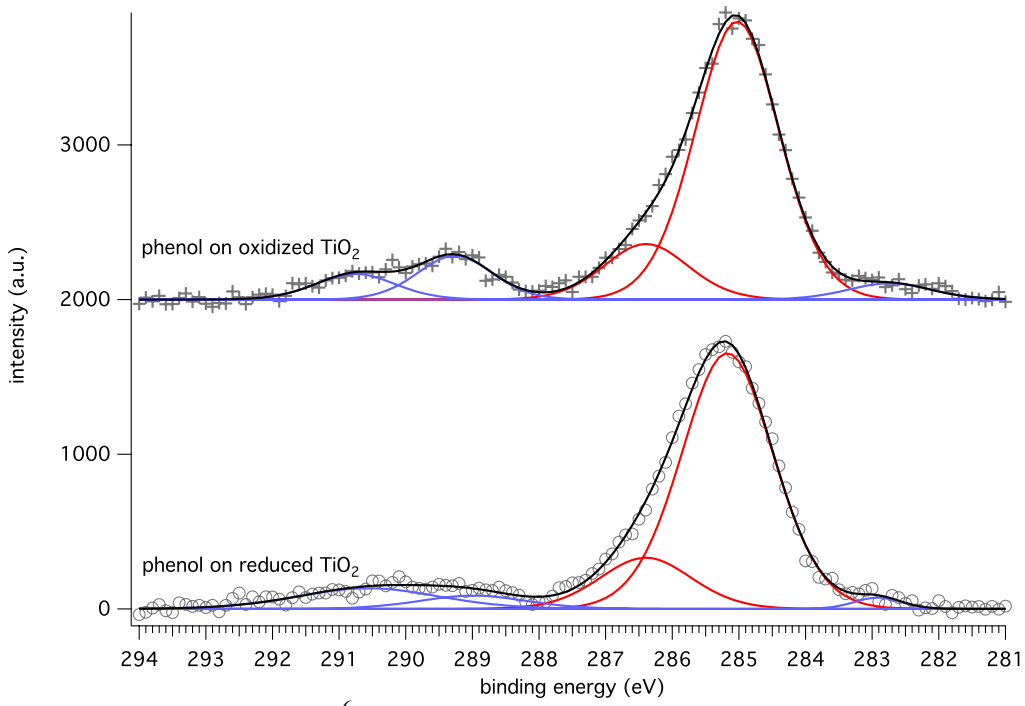

Figure 4.7 C 1*s* spectra from 10^6 L phenol adsorbed on reduced and oxidized TiO_2. Symbols represent the experimental data, the red curves are fitted peaks attributed to phenoxy species, blue curves are additional peaks, and the black curve is the fit envelope. Linear backgrounds have been subtracted from all spectra, and offsets have been added for clarity.

One possible explanation for both the oxidation of the TiO_2 after phenol dose and the extra XPS peaks that are seemingly unrelated to phenol is that phenol initially adsorbs dissociatively on the reduced titania, oxidizing surface vacancies, and after some saturation coverage then adsorbs as intact phenol or phenoxyl species, resulting in the expected phenol peaks. The "extra" unattributed peaks would then be various decomposition products.

However, an alternate, and more probable, explanation for the anomalous oxidation of the TiO_2 after a high-pressure phenol dose at room temperature actually does not involve the phenol at all. The high pressure dosing is accomplished by transferring the TiO_2 into the UHV system's load lock, which has a base pressure of approximately 5 x 10^{-6} Torr, four orders of magnitude higher than the main UHV system. The residual gas in the load lock includes significant partial pressures of water, CO, CO_2, and various other species. The adsorption behavior of various gases on TiO_2 faces is quite complex and generally depends very sensitively upon the particular exposed surface and the existence of surface defects (Ref. [19] presents a review of many such experiments), but it is not unreasonable to expect that exposure of a defective TiO_2 surface to high pressures of H_2O and other species ("high pressures" relative to UHV) could lead to surface oxidation before phenol is dosed in the load lock. Even assuming that only 60s pass between the sample transfer and introduction of phenol (definitely an underestimate), the sample receives a dose of (60 s) * (5 x 10^{-6} Torr) = 300 L of background gas – enough to adsorb significantly even with a low sticking coefficient.

We argue, however, that this is not the case for samples heated to 220°C in the load lock prior to phenol dosage – it has been shown, for example, that maintaining a clean TiO_2 surface at 400 K is enough to prevent H_2O adsorption from background gas in UHV conditions [101], at least for short periods of time, and temperature programmed desorption studies of H_2O on

TiO_2(110) have shown total desorption of H_2O at temperatures lower than 220°C [102,103]. Thus the samples dosed with 10^6 L phenol at high temperature (as in Figs. 4.1 – 4.4) are not likely to have taken up significant amounts of contamination during their exposure to relatively higher pressures of background gases. And as features from the underlying TiO_2 are still visible even after 10^6 L doses of phenol, it is reasonably obvious that multilayer phenol adsorption does not occur at room temperature. This is consistent with studies of related species such as catechol [83,84,86] or nitroaromatics [90] on rutile TiO_2(110), which saturate after < 5 L doses of the respective gas phase molecules. Future studies should not need to rely on 10^6 L doses in order to simulate atmospheric conditions; the surface simply saturates after much, much lower exposures.

4.4 Conclusions

We have studied the occupied electronic states of the phenol/TiO_2(110) system as a function of phenol dosing temperature, and correlated our photoemission studies with HREELS measurements of the low-lying electronic excitations of the system. We find that after saturation doses of phenol at room temperature, the resulting photoemission spectrum exhibits features of intact chemisorbed phenol, similar to previous studies of aromatics on TiO_2, with the phenol HOMO located just above the top of the TiO_2 valence band at approximately 3 eV. Clearly identifiable phenol σ states are visible at binding energies > 13 eV, and states involving mixtures of phenol π states and TiO_2 orbitals are visible as broad unresolved bands from 6-12 eV. After dosing at 220°C, by contrast, we observe a significant suppression of the phenol HOMO (or possible shift to higher binding energy such that it overlaps with other peaks and cannot be individually resolved here), and phenol σ orbitals, accompanied by an enhancement of the Ti 3*d*-derived "defect" peak at 0.8 eV. We interpret this as a signal that charge is transferred from the phenol molecule into the TiO_2 surface, forming a stable phenoxyl radical associated with a

locally “reduced” titania species. We interpret this as a direct observation in photoemission of radical formation after chemisorption of phenol at elevated temperature. A possible interpretation, based on calculations of phenol adsorbed on TiO_2 clusters, is that the room temperature adsorption actually involves an intact phenol molecule with a hydrogen bond to a nearby surface oxygen atom, while raising the temperatre facilitates breaking the O–H bond.

HREELS studies of phenol dosed at 220°C show almost no band gap on the dosed sample, compared to a freshly prepared TiO_2 surface which shows nearly zero intensity between 1.0 – 3.2 eV loss energy, and shows excitations suggestive of a narrowing of the phenol HOMO-LUMO peak. In combination with the photoemission data, this suggests that not only does the phenoxy radical HOMO shift to lower energy with respect to chemisorbed phenol, the LUMO must also shift to commensurately lower energy in order for the HOMO-LUMO energy difference to stay constant or decrease. Core-level XPS of room-temperature dosed phenol shows no evidence of bulk reduction – in fact, exactly the opposite – but does suggest that the use of our high-pressure dosing method at room temperature is not appropriate to maintain a TiO_2 sample free of hydroxyl or organic contamination.

Chapter 5: Nanoclusters for Catalysis: Au/*h*-BN/Rh(111)

5.1 Introduction

One possibility for tailoring the size, shape, and distribution of Au nanoparticles for catalytic reactions of interest is through deposition onto a patterned substrate. Hexagonal boron nitride (*h*-BN) thin films grown epitaxially on single-crystal transition metal surfaces show unique promise as such a template for various reasons. First, the growth of single-layer *h*-BN on transition metal surfaces by pyrolysis of borazine is easily accomplished [48], and the self-limiting nature of the growth process guarantees precise control of the *h*-BN film thickness and morphology. The resulting monolayer films show thermal stability and chemical inactivity up to 600°C [104]. Finally, *h*-BN films can form a variety of self-assembled nanostructures that vary with the choice of transition metal substrate, from a (1x1) monolayer on Ni(111) [47] to a highly corrugated structure on Rh(111) and Ru(0001) [48-50]. In general, the binding of *h*-BN to transition metal surfaces is influenced by the lattice match of the metal surface and the *h*-BN film and the degree of hybridization between metal *d*-bands and *h*-BN π* bands [53,105-109]. Hence, Ni(111), which has a nearly perfect lattice match to the *h*-BN and partially unfilled *d*-bands, shows a relatively strongly bound commensurate *h*-BN monolayer [110], while Cu(111) shows a much weaker binding of the *h*-BN monolayer [105]. Of the 4*d* elements, Ru(0001) and Rh(111) have a large lattice mismatch to the *h*-BN (8.2% and 7.6%, respectively), but unfilled *d* bands that should result in strongly bound *h*-BN layers. Finally, *h*-BN on transition metal surfaces is free of oxygen and can help avoid ambiguities in the interpretation of the nature of the active site in CO oxidation on Au nanocatalysts [111,112].

Thus, rather than adopting a strongly bound (1x1) monolayer, the *h*-BN films grown on these 4*d* surfaces have become widely referred to as a "nanomesh" structure, with hexagonal

"pores" of diameter 2 nm surrounded by "wires" sitting farther away from the Rh surface, with an overall periodicity of 3.2 nm, corresponding to a unit cell consisting of a 12x12 substrate against a 13x13 *h*-BN superstructure [50,113]. Spectroscopic techniques show splitting of the *h*-BN σ and π bands [46] and of core-level N 1*s* and B 1*s* states [109] of the nanomesh on both Ru(0001) and Rh(111), which was initially attributed to the formation of a double *h*-BN layer [48], but was later recognized to be a consequence of the "nanomesh" structure of an *h*-BN monolayer. As a result of the preference for strong binding to the metal surface competing with the lattice mismatch, the strongly bound *h*-BN "pore" regions are in fact chemically distinct from the "wire" regions. The resulting periodic structure of varying chemical environments provides a template that may facilitate the nucleation of nanoparticles on the order of the pore size. Buffer layer assisted growth has been used to deposit Co nanoparticles in such a fashion, with the resulting nanoparticles shown to be electronically decoupled from the underlying Rh(111) [56,57]. A comprehensive understanding of how the deposition and growth conditions affect the size and number density of metal nanoclusters formed on template surfaces can enable an entire class of new nanomaterials suited for model catalytic studies [114-116].

Goriachko *et al*. studied the formation of larger Au clusters on *h*-BN/Ru(0001) with STM, observing at room temperature both the nucleation of clusters in the pores and the formation of larger two-dimensional islands that extend over several pores and display the same pore-wire corrugation as the nanomesh [54], akin to the 2D Au islands formed on graphene moiré/Ru(0001) [35,38]. Ng *et al*. used synchrotron-based ARPES, XPS, and NEXAFS to probe sub-monolayer Au on *h*-BN/Rh(111) deposited at room temperature and annealed up to 875 K, inferring nucleation of 2D Au clusters within the *h*-BN pores at room temperature, diffusion of Au between pores resulting in the formation of 3D clusters starting at 575 K, and eventual Au-

Rh surface alloying at 875 K [55]. DFT studies of single- and few-atom Au clusters in the *h*-BN nanomesh show a strong preference for an Au adatom to bind in the pores [117], with very high barriers to diffusion between pores [117] and a net negative charge on the Au cluster s[118]. So far, multi-atom Au clusters have yet to be directly modeled and optimized on the full *h*-BN/Rh(111) pore-wire structure using DFT.

In this chapter, we examine the templated nucleation and growth of Au nanoclusters on the *h*-BN nanomesh supported on Rh(111) using STM and XPS, and mention the results of density functional calculations performed by collaborator Ye Xu from the LSU Department of Chemical Engineering that provide microscopic insights into the formation and charge state of nanoparticles that we observe experimentally.

5.2 Experimental Methods

STM and XPS experiments were performed in an ultra-high vacuum system with a base pressure of $1x10^{-10}$ Torr consisting of two chambers connected by a gate valve. The sample preparation chamber is equipped with a sputter gun, LEED (Specs ErLEED 150), leak valves to dose various gases, and an Omicron VT STM XA, while the other chamber contains an Omicron XM1000 monochromatic X-ray source and SPECS PHOIBOS 150 hemispherical analyzer for high-resolution XPS experiments.

The Rh(111) single crystal was cleaned by repeated cycles of 15 minutes of Ne^+ sputtering and flashing by e-beam annealing to 1175 K. Surface cleanliness was monitored with LEED and XPS. After a clean surface was obtained, *h*-BN films were grown by thermal decomposition of borazine $(HBNH)_3$ (liquid in a glass tube attached to a standard leak valve, purified by several freeze-pump thaw cycles) at a pressure of $1x10^{-7}$ Torr for 20 minutes (total dose 120 Langmuir) [48,49]. This dosing procedure resulted in a complete, clean, well-ordered

h-BN film as monitored by LEED, XPS, and STM. Films kept in UHV conditions for long periods of time proved resistant to adsorption of oxygen- or carbon-containing species within the sensitivity of XPS.

Au was evaporated on samples *in situ* in the STM from a home-built thermal evaporator (high-purity Au wire wrapped around a tungsten filament) installed in one of the 2 ¾" ports in the Omicron VT STM XA system. Sample temperature during evaporation was monitored using a Pt-100 resistor mounted just above the sample stage in the STM; using the STM's liquid N_2 flow cryostat, an ultimate sample temperature of 115 K can be realized. The evaporator filament was kept warm for extended periods prior to sample cooling and Au evaporation in order to minimize outgassing and prevent physisorption of unwanted species onto the cold sample. Au dosage was calibrated by evaporating Au onto a clean Ru(0001) sample (Au on Ru(0001) is known to grow as single-layer islands at submonolayer coverages [119]) and determining the percentage of the Ru surface covered using STM.

STM experiments were performed using homemade electrochemically etched tungsten tips. The tunneling voltage and current were set to 1 V and 100 pA, respectively, to minimize interactions between the tip and Au clusters, as the tip was observed to pick up and drag clusters along the surface using lower voltages or higher currents. Ordinarily these tunneling conditions result in bright "wires" and dark "pores" appearing in images of the clean *h*-BN film, with the image contrast matching the actual geometric structure of the film; however, on occasion adsorbed species on the tip caused an observed contrast reversal, with dark wires and bright pores. (This contrast reversal is a consequence of imaging unoccupied rather than occupied states of the *h*-BN film [113].) Our observations of the height and lateral size of Au clusters were not affected by these imaging conditions, however.

For each sample, XPS survey spectra were taken using a pass energy of 40 eV to ensure correct sample alignment and to check for any contamination. High-resolution spectra of B 1*s*, N 1*s*, and Au 4*f* peaks were recorded using a pass energy of 20 eV. Spectra were fitted using the built-in routines in CasaXPS; the details of the fits are discussed in the appropriate portions of the Results section below.

5.3 Results and Discussion

5.3.1 STM Results

We begin by examining the growth of Au clusters on the *h*-BN/Rh(111) surface under a variety of deposition conditions, varying the substrate temperature during deposition as well as during measurement. We first study the deposition of sub-monolayer amounts of Au in order to investigate the nucleation behavior of small clusters, then turn to the deposition of larger amounts of Au in order to study the templated growth of larger nanoparticles.

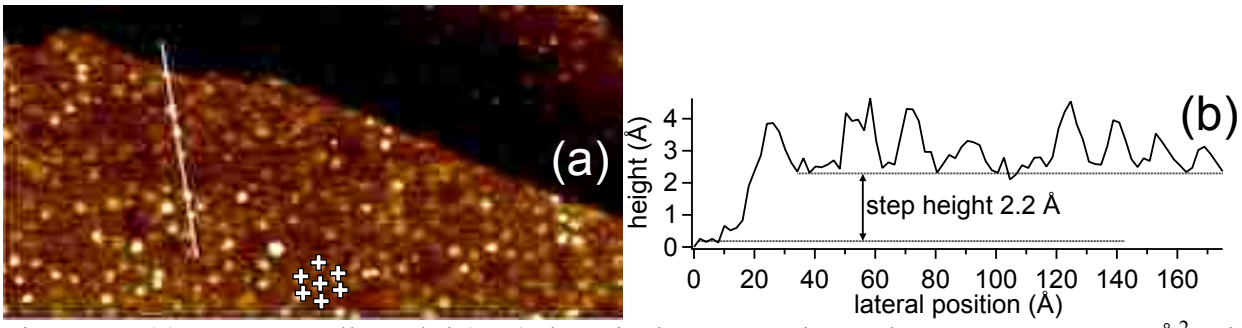

Figure 5.1 (a) 0.3 ML Au/*h*-BN/Rh(111) deposited at 115 K, imaged at 115 K, 500x250 Å^2. Tip voltage +1 V, tunneling current 100 pA. (b) height profile along the line indicated in a).

Figure 5.1a shows an STM image of 0.16 ML Au deposited with the sample temperature held at 115K, and imaged at 115K. The line profile in Figure 5.1b corresponds to the indicated line in the image. The step edge running diagonally from top left to middle right in the image is included in the height profile. We measure the step height as approximately 2.2 Å, taking the average difference in the *z*-direction from the bottom of a pore on the bottom step to the bottom of a pore in the top step. This is in excellent agreement with a monatomic Rh(111) step-height

distance [120]. Although the full nanomesh structure is not apparent due to tip effects, the hexagonal pore-wire structure is visible (indicated by crosses in Figure 5.1a). Due to presumed adsorbates on the tip, pores are imaged as bright spots and wires as dark lines, as referenced above. Au clusters in the pores are brighter than the unfilled pores. The line scan across several clusters indicates that these are all approximately 1.5 Å high (relative to the bottom of a pore), indicating that they most likely consist of a single layer of Au. Under these conditions, we imaged no clusters that unambiguously consisted of more than one Au layer. This uniform growth mode was previously inferred from photoemission and NEXAFS studies of similar Au coverage on *h*-BN/Rh(111) at room temperature [55]; here we show unambiguously that after deposition at 115 K, Au exists exclusively in monoatomic islands within the nanomesh pores.

Figure 5.2a shows the same sample as Figure 5.1a, warmed to room temperature and imaged at room temperature. In addition to monolayer clusters inside the pores of the *h*-BN nanomesh, larger clusters are also apparent. Due to the choice of color scale (simultaneously showing the small nanomesh corrugation and the relatively taller clusters), the difference in cluster heights is only readily apparent by examining line profiles.

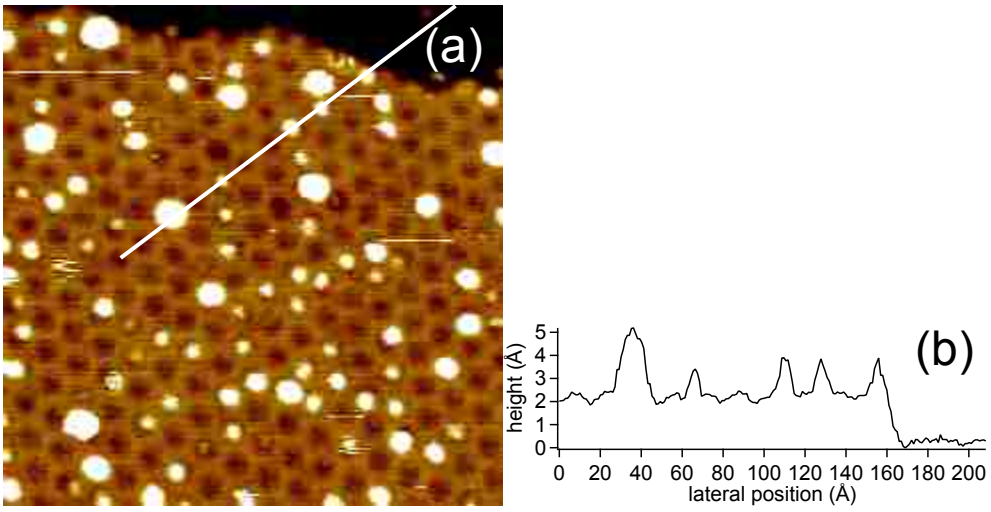

Figure 5.2 (a) 0.16 ML Au/hBN/Rh(111) deposited at 115 K, imaged at 300K, 250 x 250 Å^2. Tip voltage +1 V, tunneling current 100 pA. (b) Height profile along the line indicated in (a).

The indicated line scan in Figure 5.2b shows that the small clusters still maintain the 1.5 Å height observed in the 115K image, but additionally we see larger clusters of height 3 Å (e.g. the leftmost cluster in the profile in Figure 5.2b), corresponding to a bilayer of Au. These bilayer clusters are also imaged as having larger lateral sizes – the bilayer cluster in Figure 5.2b measures approximately 21 Å across, compared to the 8-11 Å for the single-layer clusters in the same line scan. In this image, there also exist three clusters that appear to be even taller than a bilayer, but these populate less than 5% of the nanomesh pores.

In Figure 5.2a, we find that of the filled pores, approximately 80% are filled with single-layer clusters at room temperature, with the rest containing bilayer and the few trilayer clusters noted above. The majority of the nanomesh pores, approximately 63%, are still totally empty at this coverage. Raising the temperature from 115 K to 300 K has evidently enabled some diffusion of Au between pores, but the vast majority of the single-layer clusters remain where they initially nucleated.

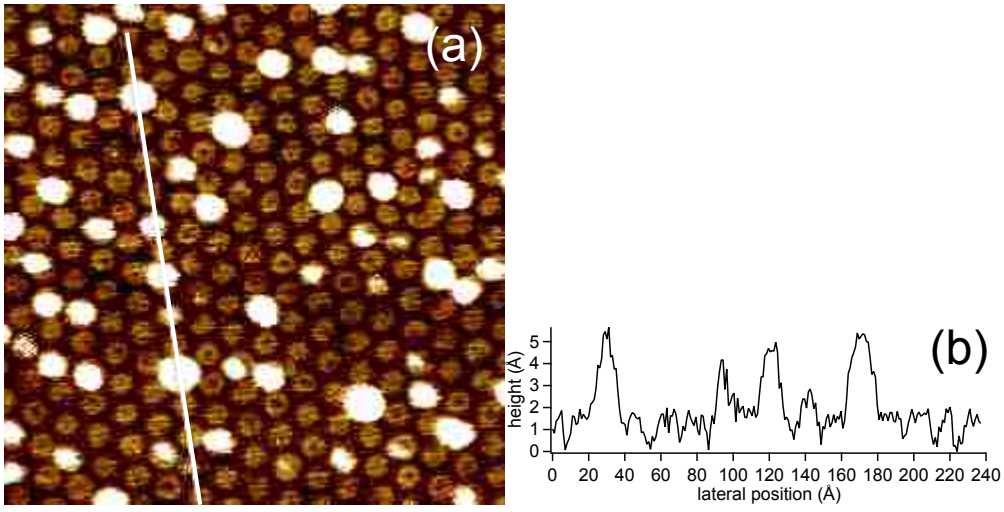

Figure 5.3 (a) 0.16 ML Au/*h*-BN/Rh(111) deposited at 300 K, imaged at 300 K, 250 x 250 $Å^2$. Tip voltage +1 V, tunneling current 100 pA. (b) Height profile along the line indicated in (a).

Figure 5.3a shows again 0.16 ML Au, but deposited and imaged at room temperature. The indicated line scan in Figure 5.3b shows that typical clusters deposited at room temperature

are somewhat larger than the equivalent amount of Au deposited at 115 K and warmed to room temperature. The relative occupation of single-layer versus bilayer or larger clusters is drastically different from the sample examined in Figure 5.2 – here approximately 40% of the clusters are single-layer and 60% bilayer or larger.

In contrast to studies of sub-ML Au/*h*-BN/Ru(0001) [113] and Au/graphene/Ru(0001) [35], we observe only the nucleation of small clusters confined to the nanomesh pores, and see no evidence of so-called "replica islands" – single-layer islands extending over several pores (or repeat distances of the graphene moiré) that maintain the corrugation of the underlying nanomesh or moiré structure. One possible explanation is the relatively weaker binding between *h*-BN on Rh(111) versus Ru(0001). This suggests that the 2D island morphology previously observed on *h*-BN and graphene is principally controlled by the underlying Ru(0001) rather than the *h*-BN monolayer acting as a template. The lesser degree of hybridization between electronic states of the *h*-BN film and the underlying metal results in a greater decoupling of deposited Au from the underlying metal, resulting in the exclusive growth of clusters rather than 2D islands that attempt to maintain the registry of the transition metal surface.

Having seen that the initial stages of Au cluster growth occur exclusively by nucleation within the *h*-BN pores, it is natural to examine the subsequent growth of clusters covering a larger percentage of the surface. Figure 5.4 depicts the results of 5 ML Au deposited on *h*-BN/Rh(111) at 115 K, and subsequently warmed to room temperature and imaged. Figure 5.4a and 5.4d show a representative 1000x1000 Å area of the sample and a histogram showing the distribution of cluster diameters within that area, while Figure 5.5b shows a 500x500 Å area with a line scan across several clusters depicted in 5.4e. The 2000x2000 Å area shown in Figure 5.5c demonstrates the monodispersed nature of the Au clusters over a large area of the surface.

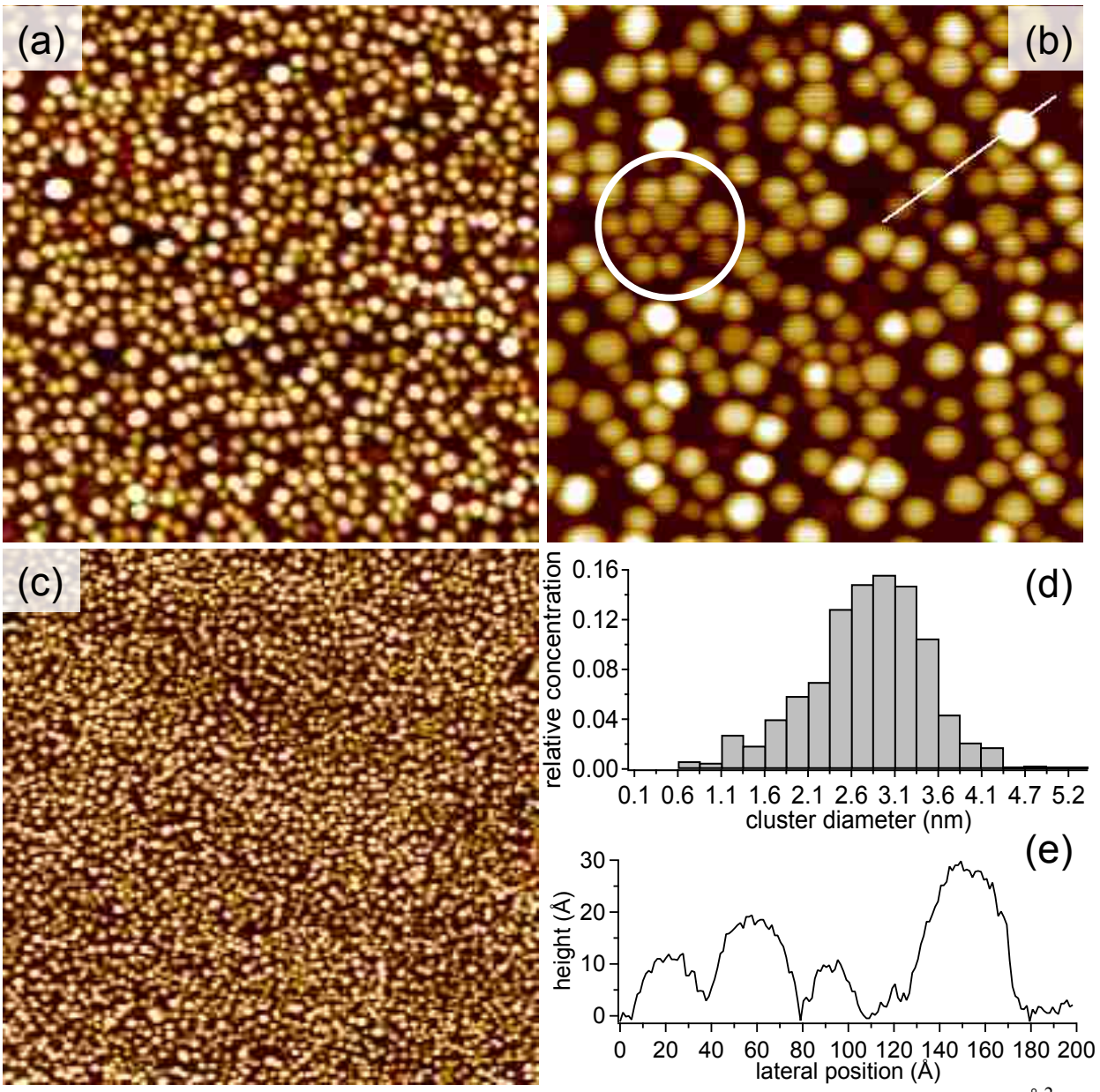

Figure 5.4. (a) 5 ML Au/*h*-BN/Rh(111) deposited at 115K, imaged at 300 K, 1000 x 1000 Å^2. (b) 5 ML Au/*h*-BN/Rh(111) deposited at 115 K, imaged at 300 K, 500 x 500 Å^2. (c) 5 ML Au/*h*-BN/Rh(111) deposited at 115 K, imaged at 300 K, 2000 x 2000 Å^2 showing large-scale cluster dispersion. (d) Histogram depicting distribution of Au cluster diameters in (a). (e) line profile along the line indicated in (b).

The cluster diameter distribution in Figure 5.4d is peaked at approximately 28 Å and shows very few clusters larger than 32 Å across – in other words, virtually no clusters are larger than a single unit cell of the *h*-BN nanomesh. (Tip convolution effects likely result in measured cluster diameters that are somewhat larger than the actual values). The 500×500 Å image in

Figure 5b) and corresponding line scan in 5e) show representative heights and diameters of several Au clusters – in general, the line profile shows roughly ellipsoidal clusters, with heights approximately 10-25 Å. The clusters indicated by the white circle in Figure 5b) show that the hexagonal spacing is roughly maintained, although again tip effects result in a perceived separation between clusters that is slightly smaller than the width of the nanomesh "wire". Figure 5c) demonstrates the uniformity of the clusters across a larger (2000×2000 Å) region of the *h*-BN film. The number density of clusters imaged in Figure 5 is approximately 0.08 clusters/nm^2, compared to an ideal value of 0.11 clusters/nm^2 (exactly one cluster per pore), or roughly 70% of the density of a "perfect" cluster distribution. Thus even with Au coverages > 1 ML, the *h*-BN template facilitates the growth of dense cluster arrays rather than very large individual clusters.

5.3.2 XPS Results

With XPS, we are able to examine the core-level electronic structure of the *h*-BN film and the deposited Au nanoparticles as a function of Au dosage. In this way, we may experimentally probe for signs of charge transfer to or from the Au and examine the intrinsic metallic properties of the nanoparticles (final-state effects related to core hole screening) as a function of particle size.

Due to instrumental limitations, we are unable to measure XPS spectra of a sample held at 115 K after deposition, so are unable to examine the exclusively single-layer clusters imaged in Figure 1. Due to overlap between the Rh 4*s* and Au 4*f* peaks (the Rh 4*s* binding energy is 81.4 eV[68], and the peak has a strong tail at higher binding energy overlapping the Au $4f_{7/2}$ peak), it is clearest to present the Au 4*f* XPS data (open circles in the figure) as difference spectra, subtracting a spectrum from a freshly-made *h*-BN/Rh(111) sample from the Au-dosed spectra to remove the Rh 4*s* peak. Additional linear backgrounds have been subtracted from the difference

spectra and from the single-crystal reference spectrum before fitting. The Rh-derived peaks in all of our spectra show no significant changes as a function of Au dosage other than attenuation. In light of the above observation of a lack of "replica islands" as seen for Au/*h*-BN/Ru(0001), this may be taken as another indication of a very weak or nonexistent interaction between the Au and the Rh underlying the *h*-BN film.

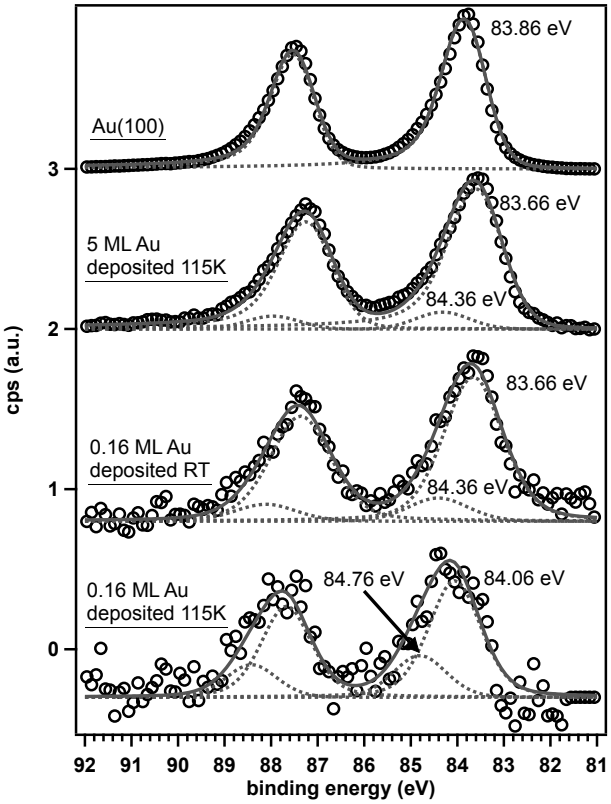

Figure 5.5 Au 4*f* difference XPS with fits. From bottom to top, we show 0.16 ML Au deposited at 115 K, 0.16 ML Au deposited at RT, 5 ML Au deposited at 115 K, and an Au(100) single crystal for reference. All spectra were acquired at room temperature. Open circles show the difference spectra resulting from subtracting a pristine *h*-BN/Rh(111) spectrum from each Au-dosed spectrum, individual fit components are shown as dashed lines, and overall fit envelopes are shown as solid lines.

The bottom-most spectrum in Figure 5.5 shows Au 4*f* XPS from 0.16 ML Au deposited at 115K and subsequently warmed to room temperature (as imaged in Figure 5.2). The best fit to the data is obtained by fitting the Au 4*f* lines with two pairs of peaks with the appropriate spin-

orbit splitting, indicated by the dashed curves in the figure. With reference to an Au single crystal measured in the same XPS system (topmost spectrum in Figure 5.5), the binding energy for the more intense peak is shifted slightly higher (0.2 eV), and the less intense peak is shifted considerably higher (0.9 eV). If attributed to an initial state effect, this would suggest that some of the Au clusters are positively charged, but in light of the B 1*s* and N 1*s* data presented in Figure 5.6 as well as the DFT results presented below, we instead attribute this shift to final-state effects, with reduced screening in the reduced-dimensional Au clusters causing a shift to higher apparent binding energy. We therefore attribute the less intense Au 4*f* peaks (at 84.76 and 88.46 eV) to the single-layer Au clusters imaged in Figure 5.2, and the more intense set of peaks to the bilayer clusters. Supporting this interpretation is the fact that the spectra are best fit with peaks of a Gaussian/Lorentzian product functional form rather than an asymmetric Doniach-Sunjic form characteristic of bulk metallic systems or of nanoparticles large enough to show bulk-like screening properties [121].

In light of this interpretation of peak shifts due to final-state effects and multiplets arising from nanoparticles of distinctly different sizes, we can consistently explain all the features of the spectra in Figure 5.5. The second spectrum from the bottom, corresponding to 0.16 ML Au deposited and imaged at room temperature (imaged in Figure 5.3), shows a similar structure, but with relatively less intensity in the higher binding energy peak, and with both peaks shifted to somewhat lower binding energy with respect to that for 0.16 ML Au deposited at 115 K. This suggests that the larger clusters observed in STM after room temperature deposition show some evolution towards more bulk-like electronic structure, with the very smallest single-layer clusters still present contributing the higher binding energy component. We still obtain better fits using pairs of symmetric peaks (Gaussian/Lorentzian products) rather than asymmetric (Doniach-

Sunjic) lineshapes characteristic of metallic Au, which again is consistent with the observed size distribution. In contrast, the spectrum from 5 ML Au deposited at 115 K and measured at RT, corresponding to Figure 5.4, fits an asymmetric lineshape extremely well, with only a very small symmetric component at higher binding energy, again presumably corresponding to nanoparticles at the smaller end of the size distribution. The only deviation from bulk-like behavior in the dominant component in the 1 ML Au spectrum is again a small (0.2 eV) shift toward lower binding energy with respect to bulk Au. Given that the clusters deposited under these conditions are overwhelmingly several layers tall and several nm in diameter, final-state effects are not likely to play a large role in the observed peak shift, and the shift to lower binding energy is consistent with a small negative charge residing on the Au clusters.

Figure 5.6a and 5.6b show B 1*s* and N 1*s* XPS spectra, respectively, which gives some insight into charge transfer between the *h*-BN support and the deposited Au. The bottom-most spectrum in each panel shows a freshly prepared *h*-BN film just after deposition, and subsequent spectra, appropriately labeled, show spectra corresponding to each Au dose imaged in Figs. 5.2-5.4. Both B 1*s* and N 1*s* are fit well with a single symmetric peak at binding energies of 190.46 and 398.26 eV respectively. These are nearly identical to binding energies (referenced to the Fermi level) reported for BN films on Pd(111) [46], and agree within at most ±1.2 eV with binding energies reported for BN on Ni(111), Pt(111), and Ru(0001) [46,49]. Synchrotron XPS experiments have indicated that both the B and N core-level peaks are split into two components with a small separation in energy (approximately 0.4 and 0.7 eV, respectively) [109] due to the differing chemical environments of the pores and wires of the nanomesh structure, exactly analogous to the splitting of σ and π bands in valence band photoemission [107]. The reduced resolution, surface sensitivity, and photon flux of laboratory XPS compared to a synchrotron

experiment results in the apparent single-peak structure here. Au deposition induces no chemical shift in either peak and minimal linewidth broadening or narrowing.

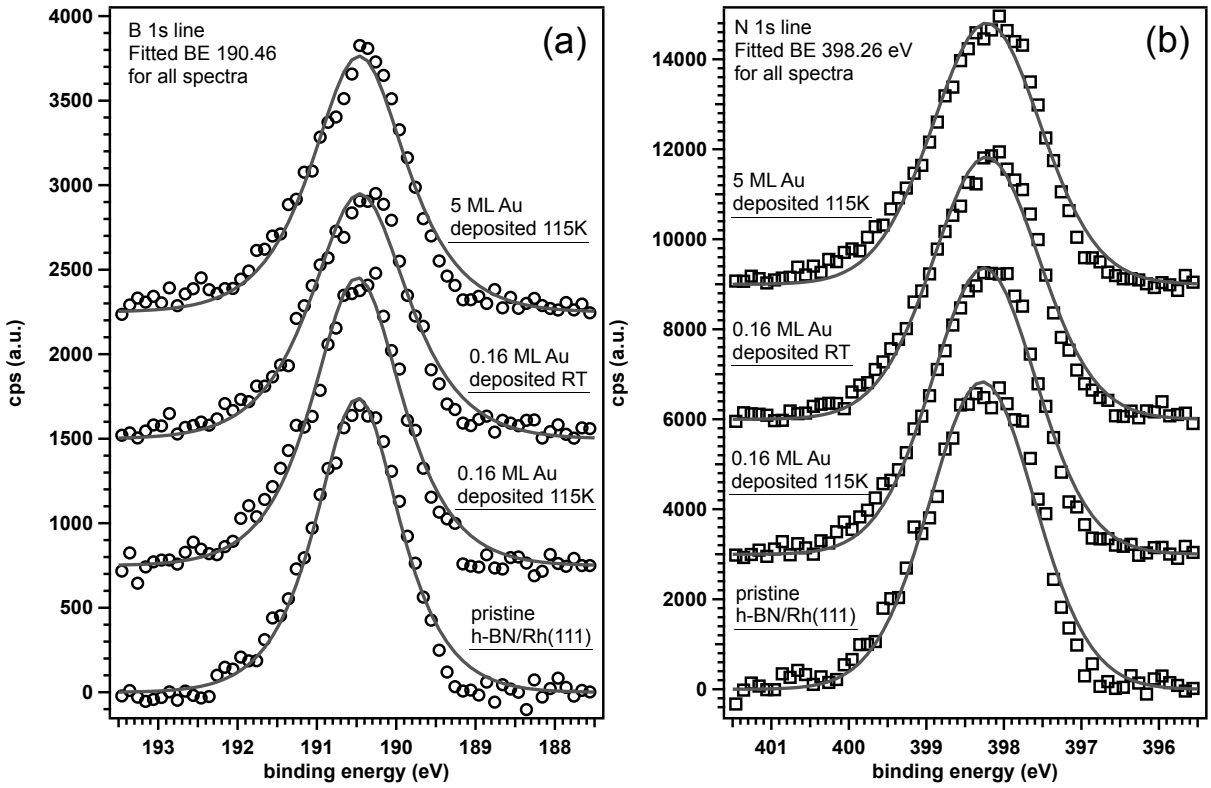

Figure 5.6 (a) B 1*s* XPS after the Au doses depicted in Figure 5.5. (b) N 1*s* XPS after the Au doses depicted in Figure 5.5.

We therefore are confident in our interpretation of the Au 4*f* XPS in Figure 5.5 as being dominated by final-state effects related to the reduced screening of core holes induced by the restricted nanoparticle size. The DFT results discussed below suggest that particularly the single-layer Au clusters do become negatively charged, but the amount of charge transfer from the BN film as reflected in chemical shifts or additional B and N core level peaks is beyond our ability to detect with laboratory XPS. The STM data presented in Figure 5.2-5.4 above show that the vast majority of the surface remains uncovered by Au at sub-monolayer coverages, so the percentage of available B or N sites from which charge could be transferred is correspondingly small. The already low cross-section for B 1*s* and N 1*s* at the available photon energy combined with the

fraction of a monolayer of atomic sites participating in charge transfer therefore likely renders chemical shifts in these peaks invisible to this experiment regardless of whether they actually occur. A prior EXAFS study of the N K-edge after 0.2 ML Au deposition on *h*-BN/Rh(111) showed no change in lineshape from a clean *h*-BN film either at room temperature or after annealing up to 600°C, indicating that if charge transfer to Au happens at room temperature, it is likely that charge is primarily transferred from boron [55]. This is consistent with the result one would expect from a simple electronegativity argument.

Density functional calculations performed by our collaborators in general show good qualitative agreement with the STM and XPS results presented here. The *h*-BN film on Rh(111) was modeled with a (13x13) *h*-BN monolayer on top of a (12x12) Rh(111) three-layer slab, with a total of 169 B, 169 N, and 432 Rh atoms in the unit cell. DFT calculations performed using various functionals severely overestimate the corrugation of the *h*-BN monolayer, if the STM data is taken to be a true representation of the geometric structure of the film. While we consistently measure a pore-wire corrugation of approximately 0.5 Å, DFT arrives at much larger values regardless of functional – 2.512 Å (LDA), 2.204 Å (GGA-PBE), and 2.356 Å (optB86b-vdW-DF) – and similarly overestimates the heights of Au clusters calculated using the optB86-vdW-DF functional, giving a height of 3.4 Å for a single-layer cluster and 6.28 Å for the bilayer. DFT does reproduce the growth mode of clusters as occurring solely within the nanomesh pores, and shows stable monolayer and bilayer clusters, with a monolayer/bilayer size transition happening as the Au cluster grows beyond ~30 atoms – the point at which at which it becomes unfavorable for Au atoms to "climb the walls" of the nanomesh wires and add to the periphery of a monolayer cluster. Bader charge analysis of single Au adatoms, few-Au-atom single-layer clusters, and a 51-atom bilayer cluster qualitatively reproduces the charge trends

reported in XPS, with a single Au adatom showing a charge of -0.462*e* and larger clusters showing an average negative charge per Au atom that decreases monotonically with cluster size.

5.4 Conclusions

In summary, we have studied the nucleation and growth of Au on the *h*-BN/Rh(111) surface using STM, and XPS. Deposition of sub-monolayer amounts of Au results in mostly single-layer and bilayer Au clusters confined to the pores of the *h*-BN nanomesh, with the principal difference between deposition at 115 K and 300 K being the change in relative proportion of monolayer and bilayer clusters formed, with monolayer clusters predominating at low temperature. Deposition of larger amounts of Au results in the formation of well-dispersed clusters mainly < 30 Å across and < 25 Å tall, with cluster diameters restricted by the pores of the nanomesh. XPS results show strong influence of final-state effects for sub-monolayer doses of Au, with suggestions of negative charging of bilayer and larger clusters. DFT results demonstrate the size threshold of the monolayer/bilayer transition consistent with the STM observations, and provide insight into the distribution of negative charge within 30-atom (monolayer) and 51-atom (bilayer) clusters. These well-dispersed, negatively charged Au nanoclusters with a relatively narrow distribution of diameter and height suggests that the clusters formed in the present study should show catalytic activity for CO oxidation. The difference in cluster growth modes (exclusively 3D clusters rather than 2D islands maintaining the nanomesh corrugation) with respect to Au deposited on *h*-BN/Ru(0001) and graphene/Ru(0001) suggests that the Au and *h*-BN cannot be considered free or pseudo-free; the underlying metal substrate plays a role in determining the Au morphology and thus the catalytic activity.

Chapter 6: Nanoclusters for Catalysis: Au/ZnO(10$\bar{1}$0), Cu/ZnO(10$\bar{1}$0)

6.1 Introduction

Catalysts consisting of Cu or Au supported on ZnO have been widely used in a variety of hydrogenation activities, especially methanol synthesis, for the past several decades [122-126]. In various experiments involving the hydrogenation of CO_2 to methanol with Au/ZnO catalysts, Au particle size has been shown to affect the methanol yield, with smaller Au particles giving higher methanol productivity per exposed Au surface area [122-126]. Cu on ZnO(10$\bar{1}$0) has previously been studied with STM [127] and valence band photoemission [128], which indicate that Cu grows almost exclusively as 3D clusters even at very low coverage, and that the clusters are positively charged because of cluster-substrate interactions. Other work with Cu/ZnO catalysts suggests that Cu-Zn surface alloys may be a catalytically active species for methanol synthesis [123], with a Zn/Cu(111) model catalyst showing high activity for methanol synthesis from CO_2, and model Cu/ZnO catalysts showing Cu-Zn alloy formation after high-temperature reduction of the ZnO substrate. To date, little core level spectroscopy exists for Cu clusters on ZnO(10$\bar{1}$0) that might indicate Cu-Zn alloying in the as-deposited clusters, or that would explain the reported charging effects, and almost no surface science data exists for model Au/ ZnO(10$\bar{1}$0) systems that would explain the reported dependence of methanol yield on Au particle size.

This chapter previously appeared as M. C. Patterson, X. Nie, F. Wang, R. L. Kurtz, S. B. Sinnott, A. Asthagiri, and P. T. Sprunger, "Growth and Structure of Cu and Au on the Nonpolar ZnO(10$\bar{1}$0) Surface," J. Phys. Chem. C **117**, 18386 (2013). It is reprinted by permission of the American Chemical Society per the Rightslink by Copyright Clearance Center service, "Permission for this particular request is granted for print and electronic formats, and translations, at no charge."

In this chapter, we use XPS to examine the core level electronic structure of Cu and Au clusters on ZnO($10\bar{1}0$), previously studied with STM and EELS [58], to elucidate features of their electronic structure that may make them suitable models for practical Cu/ZnO and Au/ZnO catalysts. Collaborators Aravind Asthagiri and Xiaowa Nie have performed density functional calculations to interrogate the diffusion behavior, nucleation sites, and charge state of Cu and Au adatoms and few-atom clusters, which we also will briefly summarize.

6.2 Experimental Methods

ZnO($10\bar{1}0$) single crystals were purchased from MTI Corporation. Sample surfaces were cleaned by cycles of Ne ion sputtering (30 min) and vacuum annealing to 1000 °C (30 min). This far exceeds the temperature necessary to desorb both surface and bulk hydrogen [129], and ensures that any effects of hydrogen in the selvage region is minimized. Sample cleanliness was checked with LEED and XPS; clear and sharp (1×1) LEED patterns, and no contamination from carbon or other species visible in XPS, were observed after sputtering and vacuum annealing. In addition to STM and XPS, high-resolution EELS data (using an LK2000 EELS spectrometer) shows an absence of adsorbed water and/or hydroxyls (vibrational peak at ~450 meV loss energy) on the freshly cleaned surface. Before deposition, all evaporators were fully outgassed, and filaments were kept at a lower temperature than the evaporation temperature in order to ensure the Cu/Au evaporated was clean and without contamination. Deposition rates were calibrated by evaporating Cu/Au onto a clean Ru(0001) crystal (both Cu and Au are known to grow as single-layer islands at submonolayer coverages on Ru(0001) [119,130]) and determining the percentage of the surface covered using STM. The experimental STM and XPS results reported are for Cu/Au deposited under the same conditions (temperature, flux, angle, background pressure) on the same and/or identically prepared ZnO substrates.

The details of STM measurements are presented in Ref. [58]; tunneling voltages and currents were set in the range of 0.5-3V and 0.3-1.5nA respectively, depending on the surface conditions. (No new STM data is reported for this chapter; all images presented here are courtesy of Fei Wang.) XPS measurements were performed at room temperature using the system described in Chapter 2. To eliminate any effects due to sample charging, the energy scale for XPS spectra of metals deposited on ZnO was corrected by setting the Zn $2p_{3/2}$ line to a binding energy of 1021.7 eV and the O 1*s* line to a binding energy of 530.4 eV (following the procedure described by Wöll [131]), whereas reference spectra taken from Cu(111) and Au(100) single crystals did not need such correction. Zn 2*p*, Cu 2*p*, O 1*s*, and Zn 3*p* spectra were fitted in CasaXPS using a Gaussian/Lorentzian product lineshape, while the Au 4*f* spectra were fitted using a hybrid Doniach-Sunjic lineshape convoluted with a Gaussian/Lorentzian sum. The full details of DFT calculations are presented in Ref. [59]; we will not reproduce them here, but present Figure 6.1 below as an illustration of the ZnO surface unit cell used in the calculations.

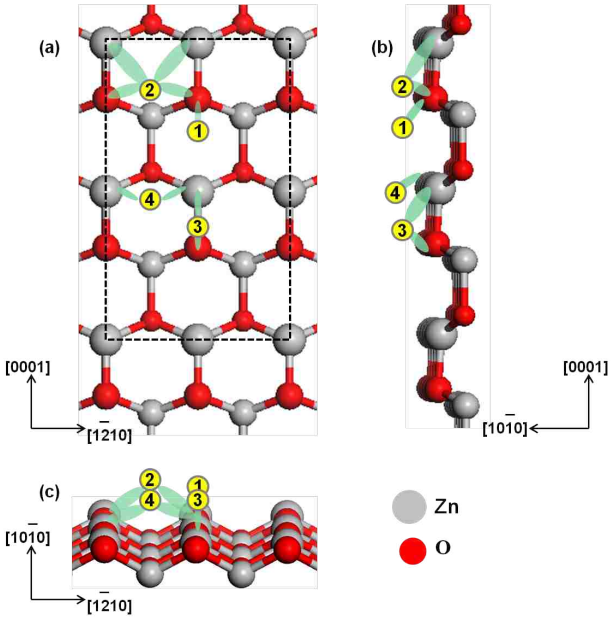

Figure 6.1**.** Various perspectives of the ZnO($10\bar{1}0$) surface with the dashed box indicating the 2×2 surface unit cell. The four unique adsorption minima for Cu and Au identified from DFT calculations are represented by yellow circles. From Ref. [59], all DFT calculations performed by Aravind Asthagiri and Xiaowa Nie.

6.3 Results and Discussion

6.3.1 STM Results

Figure 6.2a shows an STM image of 0.2ML Cu deposited on ZnO($10\bar{1}0$) at room temperature. It is clearly seen that a 3D cluster growth mode (Volmer-Weber growth mode) is adopted for very low Cu coverage at room temperature. Cu clusters preferentially nucleate at step edges perpendicular to the [$1\bar{2}10$] direction, with some small clusters formed on the terraces while almost no Cu clusters can be seen on the step edges along the [$1\bar{2}10$] direction. Assuming that the ZnO surface as prepared is nearly perfect, the nucleation mechanism for clusters on terraces rather than step edges was explained by Diebold *et al* as the Cu atoms meeting during diffusion and then nucleating, forming nucleation sites on the terrace [127]. Most of the Cu clusters have a size of ~50 Å in diameter and ~7 Å in height. The 7 Å height indicates that the clusters are mostly formed with three layers of Cu atoms.

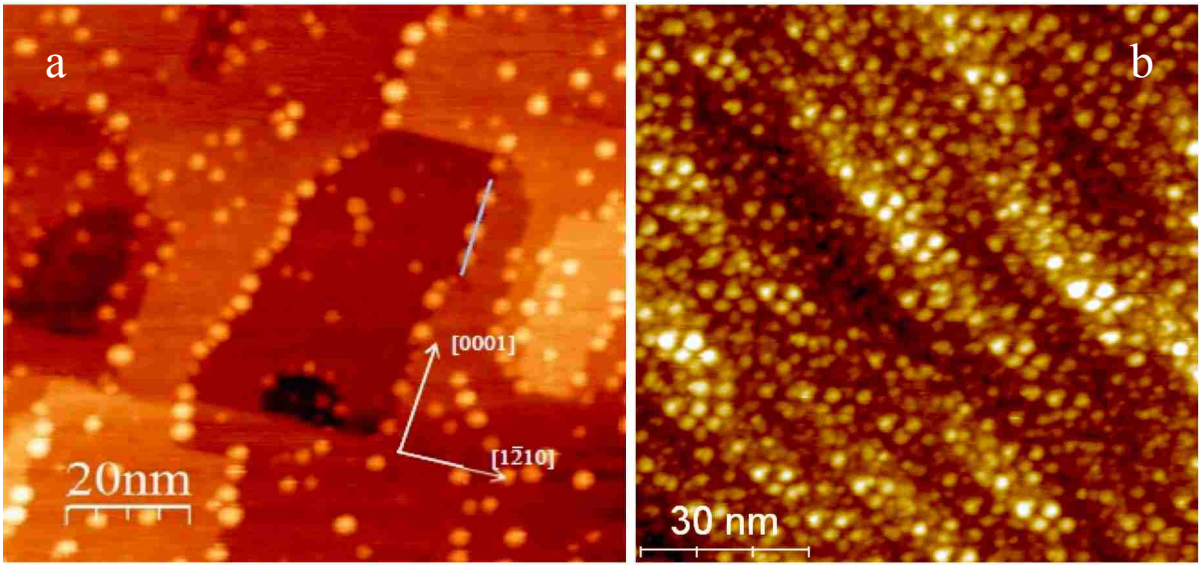

Figure 6.2 STM image (a) of 0.2 ML Cu growth on ZnO($10\bar{1}0$) surface at RT (b) of 2 ML Cu growth at RT. From Ref. [58], courtesy of Fei Wang.

Figure 6.2b shows the results of 2 ML Cu deposited at room temperature. The biggest change is in the number density of clusters; the whole surface is now covered with Cu. The

average cluster size did not change appreciably – the largest clusters are around ~50 Å in diameter and ~12 Å in height, indicating that the clusters did not grow laterally, but added one or two more layers of Cu atoms in height.

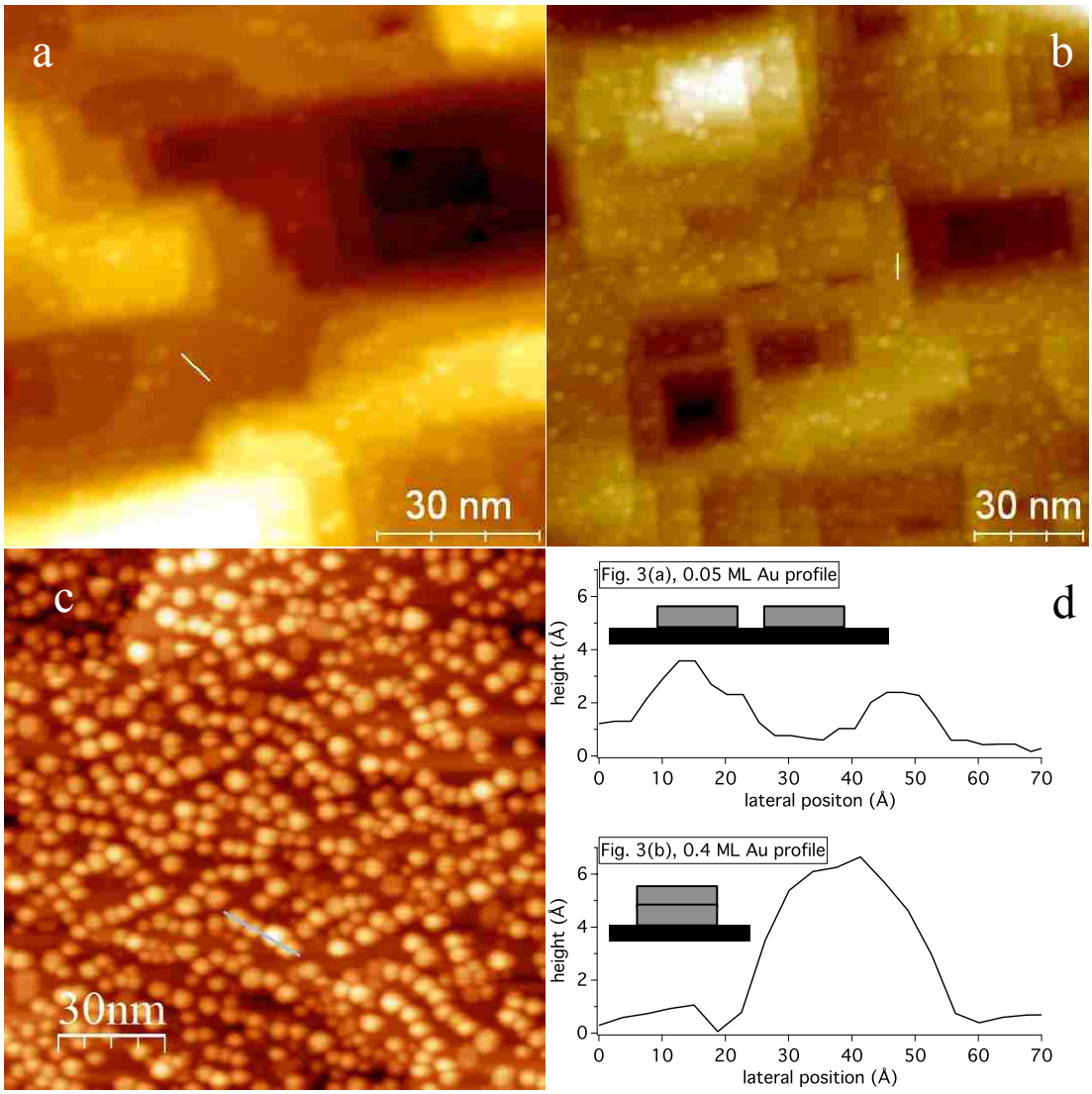

Figure 6.3 STM images of (a) 0.05 ML Au on ZnO($10\bar{1}0$) at room temperature, (b) 0.4 ML Au on ZnO($10\bar{1}0$) at room temperature, (c) 3 ML Au on ZnO($10\bar{1}0$) at room temperature, (d) height profiles of clusters along the indicated lines in (a) (top) and (b) (bottom), with schematics showing Au cluster morphology. From Ref. [59]; (a) through (c) courtesy of Fei Wang.

In contrast to the 3D growth and preferred step edge nucleation displayed by Cu at low coverages, STM studies of Au on ZnO($10\bar{1}0$) show a distinctly different morphology. Figure 6.3

shows STM images of various coverages of Au at room temperature. It is clearly seen that depositing 0.05 ML Au results in many small, 2-D shaped Au islands dispersed randomly over the surface with an average size of ~30 Å across and ~3 Å high; a sample line profile across one island is shown in Figure 6.3d. This 3 Å height represents just one layer of Au, which means a truly 2D growth mode is adopted for << 1 ML Au on ZnO($10\bar{1}0$).

Increasing the Au coverage increases the Au island density as well as island size. For 0.4 ML Au, the height of islands ranges from 3 Å to 9 Å, and most of them are less than 7 Å high, as shown in the second line profile in Figure 6.3d. The existing 2D Au islands already present from the prior 0.05ML Au deposition do not act as nucleation sites for new Au atoms arriving on the surface. The new Au atoms tend to find unoccupied sites as new nucleation sites. After an island grows to a critical size of 30-40 Å across by 7 Å high, more Au atoms will not stick to the island, and instead new islands will be formed. After the small Au islands cover a large portion of the surface, no new nucleation sites will be created, and the existing Au islands increase in size. As Figure 6.3c shows, at a coverage of 2ML, 3D Au clusters of ~70 Å across and ~15 Å high are well distributed all over the surface. The diameter is much bigger than height at this size, meaning the clusters are oblate disks and are still not spherical.

6.3.2 XPS Results

Figure 6.4a shows XPS results for increasing Cu coverage on ZnO($10\bar{1}0$), corresponding to the STM images of 0.2 ML and 2 ML Cu deposited on ZnO($10\bar{1}0$) shown in Figure 6.2. Qualitatively, the spectra are similar to those of a bulk Cu(111) single crystal, shown at the top of the plot. In the 0.2 ML Cu sample, the $2p_{3/2}$ peak shows a shift of 0.5 eV toward higher binding energy with respect to the bulk Cu, whereas the 2 ML Cu sample agrees well (<0.2 eV difference) with the measured bulk binding energy. Furthermore, the $2p_{3/2}$ peak narrows from a

full width at half maximum of 1.80 eV in the 0.2 ML sample to 1.47 eV in the 2 ML sample. (Because of the different pass energies used when taking spectra, these cannot be directly compared to the peak width from bulk Cu.)

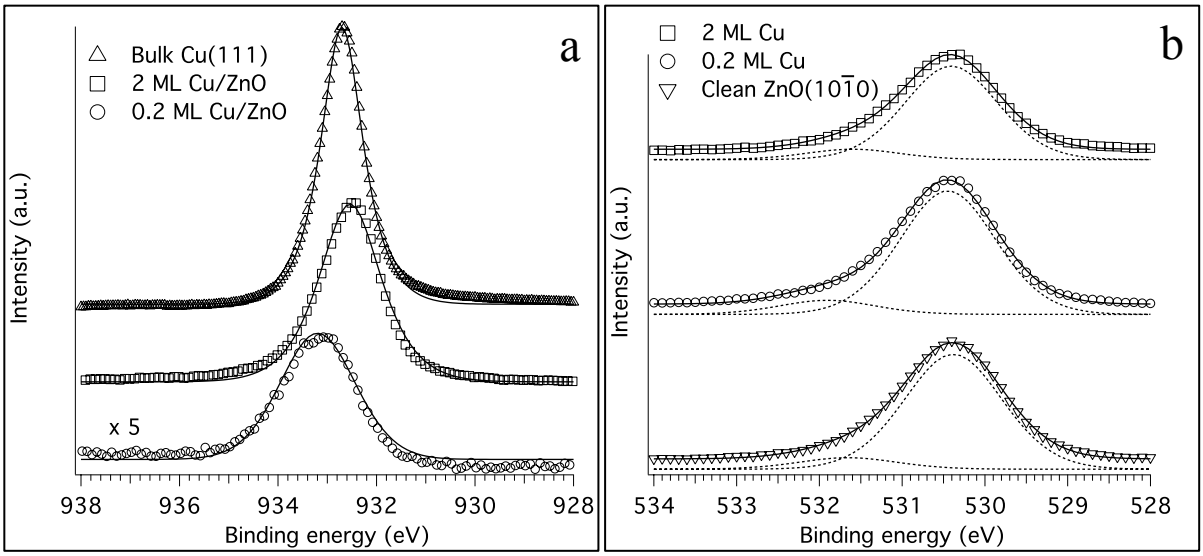

Figure 6.4. (a) Cu $2p_{3/2}$ spectra for 0.2 ML Cu on ZnO(10$\bar{1}$0), 2 ML Cu on ZnO(10$\bar{1}$0), and a Cu(111) single crystal for reference. The Cu(111) spectrum was recorded using a pass energy of 10 eV; others used a pass energy of 20 eV. Shirley backgrounds have been subtracted from all data. Open symbols show the experimental data, solid lines show the fit envelope. (b) O 1*s* spectra for clean ZnO(10$\bar{1}$0), 0.2 ML Cu, and 2 ML Cu on ZnO(10$\bar{1}$0). Shirley backgrounds have been subtracted from all spectra. Open symbols show experimental data, dotted lines show the individual fit components, solid lines show the fit envelope. From Ref. [59].

The shifted binding energies and broadened peaks might indicate that the Cu deposited on ZnO(10$\bar{1}$0) is oxidized, resembling CuO more than metallic Cu at low coverages; however, the high-intensity shakeup peaks at approximately 941 eV and 944 eV expected of CuO are absent in the 0.2 ML sample [132]. Also, the energy difference ΔE between the $2p_{3/2}$ and $2p_{1/2}$ levels remains basically constant instead of increasing as it should if the Cu in the 0.2 ML sample is in the form of CuO and the Cu in the 2 ML sample is metallic Cu [98]. (ΔE_{bulk} = 19.85 eV, ΔE_{2ML} = 19.89 eV, $\Delta E_{0.2ML}$ = 19.90 eV). The rigid shift in the spectra from 0.2 ML Cu on ZnO(10$\bar{1}$0) is better explained as an initial-state effect due to charge transfer from the Cu to the underlying ZnO, causing the bilayer Cu clusters formed at 0.2 ML coverage to become positively

charged, thus showing higher binding energies than a neutral cluster. The Bader charge analysis performed by our collaborators on few-atom Cu clusters is in qualitative agreement with this analysis. Both our XPS results and the DFT calculations are consistent with the angle-resolved photoemission study of Cu on ZnO($10\bar{1}0$) by Ozawa *et al,* which showed through analysis of the Cu-induced Zn 3*d* band bending that evaporation of sub-monolayer coverage of Cu resulted in positively charged Cu clusters on the surface [128].

In the O 1*s* core level spectra shown in Figure 6.4b, we see evidence of two oxygen-derived peaks. The component at lower binding energy has been constrained to a binding energy of 530.4 eV in order to set the overall energy scale, as mentioned above. Both peaks were fit with Gaussian/Lorentzian product blends with identical linewidths. Slight attenuation with increasing Cu coverage is observed, but no new peaks form that would be indicative of CuO or Cu_2O formation. Both peaks attenuate at the same rate, indicating that both result from bulk oxygen rather than surface effects. We therefore attribute the higher binding energy peak to oxygen from $Zn(OH)_2$ in the near-surface region.

Figure 6.5 shows XPS results for increasing coverage of Au on ZnO($10\bar{1}0$). It is apparent that the Zn 3*p* and Au 4*f* core levels significantly overlap in binding energy (From the literature, $BE_{Zn\ 3p1/2}$ = 91.4 eV [68] and $BE_{Zn\ 3p3/2}$ = 88.6 eV [68]; from the bulk Au crystal measurement, $BE_{Au\ 4f5/2}$ = 87.56 eV $BE_{Au\ 4f7/2}$ = 83.86 eV) such that it is difficult to distinguish the Zn $3p_{3/2}$ and Au $4f_{5/2}$ levels at very low coverages of Au; nonetheless, as the figure shows, all components can be fitted. Two clear trends emerge from this set of data.

First, the Au 4*f* binding energies shift toward lower binding energies at higher coverages. As shown in Figure 6.5a, the Au $4f_{7/2}$ binding energy agrees well with the measured bulk binding energy (<0.1 eV difference) for all Au coverages except 0.25 ML, in which the $4f_{7/2}$ binding

energy is shifted 0.3 eV to higher binding energy relative to bulk Au. If we examine this in light of the STM data in Figure 6.3, we see that the small, mostly 2D clusters formed at low Au coverage show higher binding energies than the larger 3D particles formed at high Au coverage. This may be partially attributable to initial-state effects, similar to those observed above for Cu. Additionally, final-state effects also play a role in increasing the apparent 4*f* electron binding energy; few-atom clusters have fewer electrons available to screen core holes, so the Coulomb interaction between the emitted photoelectron and the core hole leads to a higher binding energy relative to bulk Au [133]. This is more likely to play a role for the Au islands than the Cu, as the smallest Au islands examined by XPS are considerably smaller than the smallest Cu. (As shown in Figs. 6.2a and 6.3a, the smallest typical Cu cluster examined is ~50 Å in diameter and ~5 Å tall, whereas the smallest typical Au island examined is only ~30 Å in diameter by 3 Å tall.)

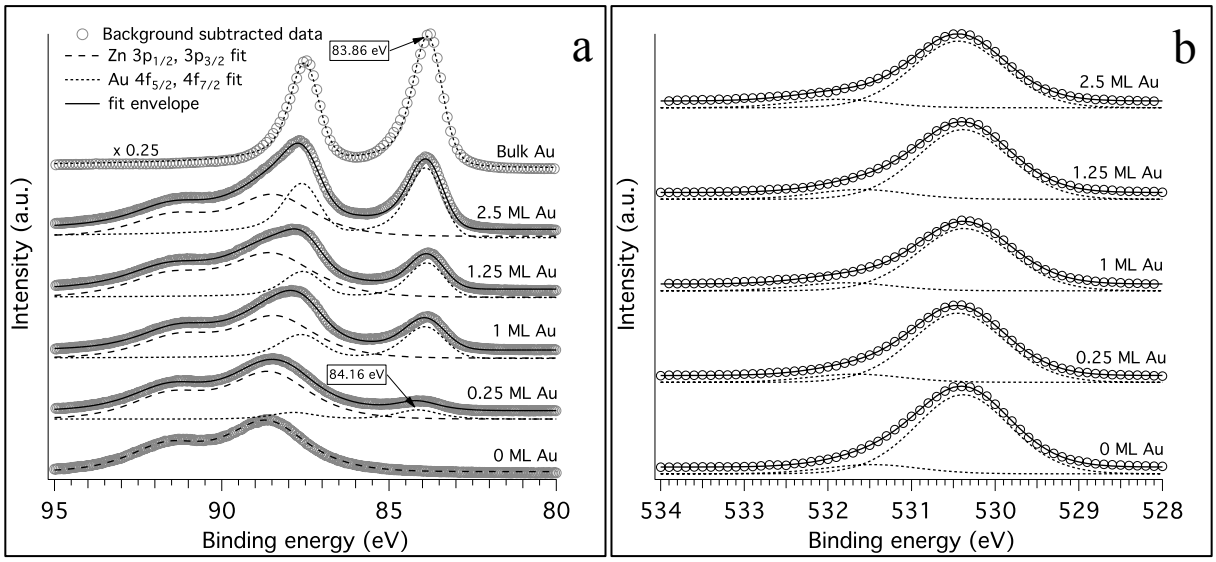

Figure 6.5 (a) Zn 3*p* and Au 4*f* core level spectra for clean ZnO(10$\bar{1}$0) and 0.25, 1, 1.25, and 2.5 ML Au on ZnO(10$\bar{1}$0), and from an Au(100) single crystal for reference. Linear backgrounds have been subtracted from all spectra. The indicated binding energies on the plot are the fitted Au $4f_{7/2}$ peak positions. (b) O 1*s* spectra for clean ZnO(10$\bar{1}$0) and 0.25, 1, 1.25, and 2.5 ML Au on ZnO(10$\bar{1}$0). Shirley backgrounds have been subtracted from all spectra. Open symbols are experimental data, dotted lines are the individual fit components, and solid lines are the fit envelopes. From Ref. [59].

Second, we see also that the asymmetry of the Au 4*f* peaks changes as a function of coverage. As mentioned above, the Au peaks were fit with a convolution of a hybrid Doniach-Sunjic with a Gaussian/Lorentzian sum, but the best fits to the experimental data are obtained when the asymmetry parameter a of the hybrid Doniach-Sunjic lineshape is allowed to vary. The Au 4*f* peaks for 0.25 ML, 1 ML, 1.25 ML, and 2.5 ML are best fit with a hybrid Doniach-Sunjic convoluted with a Gaussian/Lorentzian sum using asymmetry parameters of $\alpha = 0$ (symmetric peak), 0.04, 0.05, and 0.1, respectively. The reference spectrum from a bulk Au(100) single crystal is also fit well using the same function with $\alpha = 0.1$. Asymmetry in XPS peaks is characteristic of metallic systems, including bulk Au. Since the spectra corresponding to smaller 2D clusters show much less asymmetry, this implies that these clusters are less metallic than the large 3D clusters formed at high Au coverage [121]. We see a clear evolution towards bulk-like Au behavior, with the intermediate degree of asymmetry seen in the spectra of 1 ML and 1.25 ML Au on ZnO($10\bar{1}0$) reflecting the evolution of cluster morphology from truly 2D, single-layer clusters formed at very low coverage toward 3D multilayer clusters at high coverage.

We again see two oxygen-derived peaks in the O 1*s* core-level spectra of Au deposited on ZnO($10\bar{1}0$), shown in Figure 6.5b, which are qualitatively similar to the O 1*s* spectra taken after Cu deposition in Figure 6.4b. These peaks were fitted according to the same procedure as those in Figure 6.4(b), and they show the same behavior as a function of Au deposition as during Cu deposition. Again, the peak at higher binding energy is therefore attributed to bulk $Zn(OH)_2$.

We shall only summarize the relevant DFT results obtained by our collaborators in this chapter; for the full details of calculations, the reader should refer to Ref. [59]. In brief, calculations were performed to determine the most stable binding site for a single Cu and Au

adatom, the diffusion behavior of single adatoms over the surface, the morphology of 10- and 16-atom Cu and Au clusters, and the charge state of the 10- and 16-atom clusters.

For a single Cu adatom, site 2 depicted in Figure 6.1 and Figure 6.6 is calculated to be the most stable adsorption site, bonded on top of an oxygen atom (in approximately the same configuration as a Zn atom would be if another ZnO plane were placed on top of the surface). For a single Au adatom, the most stable site is site 1, between two Zn atoms. The four labeled sites are the unique local adsorption minima, and Table 6.1 shows the calculated migration barriers between sites. It is apparent that, while diffusion barriers along the principal symmetry directions are roughly equivalent for Au, Cu faces a much stronger barrier to diffuse in the [0001] (diffusion between site 3 to 1) direction than in the $[1\,\bar{2}\,10]$ (diffusion from site 2 to 3), with the largest barrier involved in crossing the trough running along the $[10\,\bar{1}\,0]$ direction. This qualitatively agrees with the experimentally observed preferred nucleation of Cu clusters along step edges perpendicular to the $[1\,\bar{2}\,10]$ direction – adatoms are able to diffuse rapidly along that direction until they encounter the barrier of a step. The isotropic diffusion barriers faced by Au, in contrast, also agree qualitatively with the STM data showing a uniform distribution of Au.

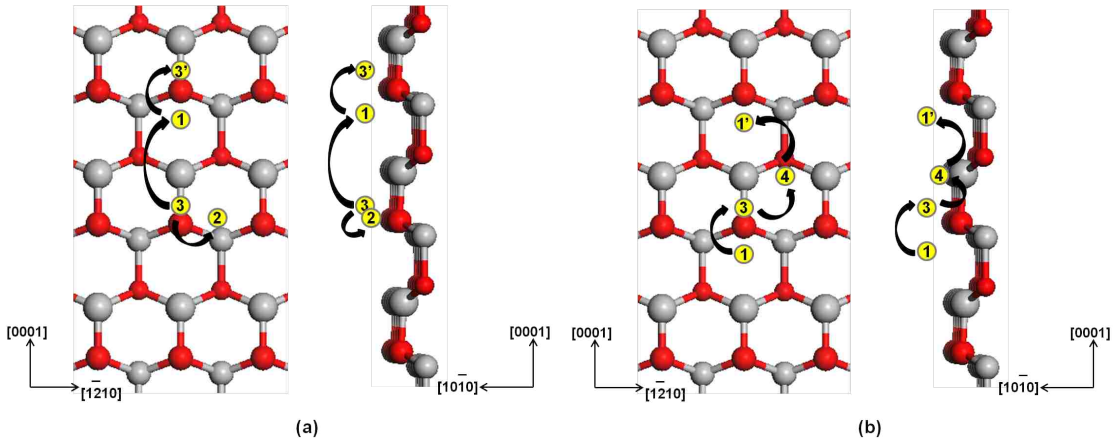

Figure 6.6 Diffusion paths for (a) Cu and (b) Au on the ZnO$(10\,\bar{1}\,0)$ along the $[1\,\bar{2}\,10]$ and [0001] directions, from Ref. [59], courtesy of Aravind Asthagiri and Xiaowa Nie.

Table 6.1. Migration barriers for single metal atom diffusion among the designated adsorption sites on the (4×4) ZnO($10\bar{1}0$) surface. From Ref. [59], courtesy of Aravind Asthagiri and Xiaowa Nie.

Cu			Au		
Diffusion Path	E_a-forward	E_a-backward	Diffusion Path	E_a-forward	E_a-backward
(3) to (2)	0.02 eV	0.29 eV	(1) to (3)	0.28 eV	0.11 eV
(3) to (1)	0.85 eV	1.04 eV	(3) to (4)	0.06 eV	0.11 eV
(1) to (3')	0.24 eV	0.05 eV	(4) to (1')	0.10 eV	0.23 eV

Figure 6.7 shows the optimized 16-atom Cu and Au clusters in both single-layer and bilayer configurations. Matching the experimental results, Au was shown to favor a single-layer structure and Cu a bilayer; in both cases, the more stable structure was preferred by a considerable energy difference of ~0.06 eV/atom, or ~1 eV/cluster. The preference for planar bonding in Au is attributed to strong *s-d* hybridization which causes more directional bonding and leads to reduced coordination compared to earlier transition metals such as Cu [134] [135].

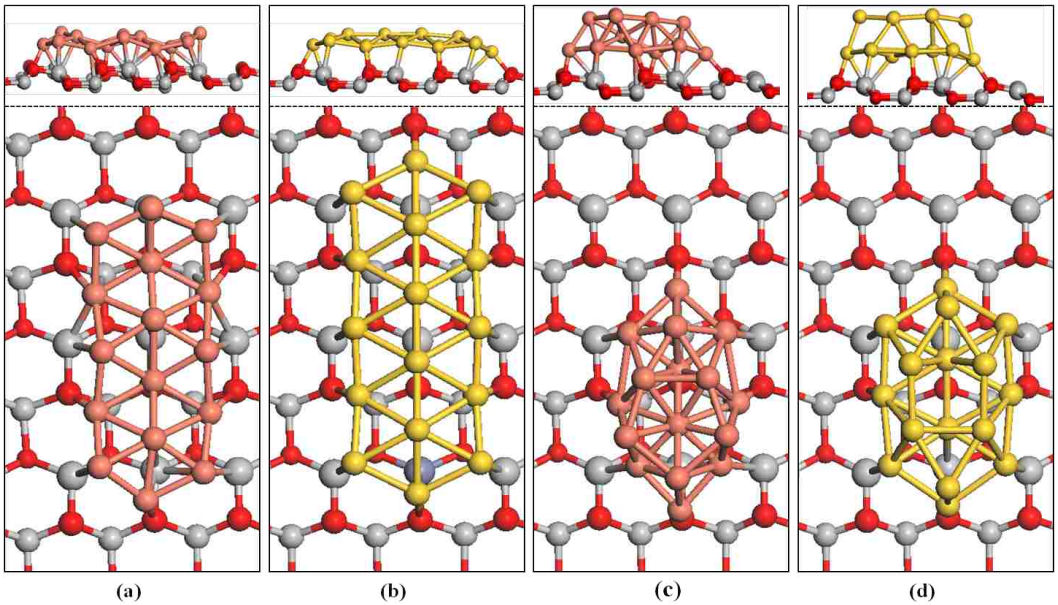

Figure 6.7. Top and side views of the optimized configurations of 16 atom Cu clusters in (a) single-layer and (c) bi-layer on the (4×4) ZnO($10\bar{1}0$) surface. Similar configurations for 16 atom Au clusters shown in (b) and (d). From Ref. [59], courtesy of Aravind Asthagiri and Xiaowa Nie.

Bader charge analysis was applied to study the metal charge states in the clusters and the resulting charges are presented in Table 6.2. While there is variation in the Bader charges within the metal cluster, the total and average (per atom) charges shown in Table 6.2 are in qualitative agreement with the XPS results presented above, with the Cu_{16} clusters showing an order of magnitude larger positive charge than the Au_{16} clusters. Furthermore, it is apparent that the charge per Cu atom in the stable 3D configuration only slowly decreases as the total number of atoms in the cluster increases, which may help to explain why the Cu clusters probed by XPS and STM still show evidence of positive charging despite being considerably larger than the clusters examined with DFT. In contrast, the average charge per Au atom in the larger 10-and 16-atom clusters is nearly zero, which qualitatively agrees with our XPS results indicating that the positive charge on an Au cluster decreases as the cluster size increases.

Table 6.2. Total charge for the 16-atom Cu and Au clusters in the most favorable cluster configuration for each species, as well as the average charge per atom (in units of the electron charge) in each cluster. From Ref. [59], courtesy of Aravind Asthagiri and Xiaowa Nie.

cluster size	Total Bader charge		Average Bader charge per atom	
	Cu-3D	Au-2D	Cu-3D	Au-2D
1	-	0.0006	-	0.00
2	-	0.0084	-	0.00
3	0.534	-0.0315	0.18	-0.01
4	0.512	-0.0884	0.13	-0.02
5	0.5075	-0.1015	0.10	-0.02
10	1.2064	0.0076	0.12	0.00
16	1.3567	0.1792	0.08	0.01

6.4. Conclusions

STM studies show that Cu nucleates 3D clusters on the ZnO($10\bar{1}0$) surface at all levels of coverage, with preferential nucleation at step edges along the [$1\bar{2}10$] direction evident for submonolayer coverages of Cu. In contrast, Au at low exposures (<0.4 ML) grows as well-dispersed single-layer islands with no preferred nucleation sites; at intermediate exposures shows a mixture of single-layer, bilayer, and some trilayer islands; and at >1 ML coverage shows a mainly 3D morphology. XPS results from these clusters show that the Cu clusters are metallic at the coverages examined, with some shifts in binding energy due to charge transfer from Cu to the substrate. The Au 4*f* spectra clearly show a trend of increasing metallicity, with small single-layer islands showing nonmetallic features and larger 3D clusters showing bulk-like features.

DFT studies show, in agreement with the STM data, a preference for Cu to nucleate as 3D clusters and Au to nucleate as single-layer 2D islands. Calculations of diffusion barriers also agree well with the STM images. Cu shows preferred rapid diffusion parallel to [$1\bar{2}10$] step edges, explaining the preferred cluster nucleation on step edges along the [0001] direction, but Au shows more isotropic diffusion, leading to more uniformly dispersed Au islands. Charge analysis also helps explain some of the features of the Cu 2*p* XPS spectra, showing positive charges on Cu at a lower coverage, which leads to higher binding energies for the Cu 2*p* peaks of Cu clusters on ZnO($10\bar{1}0$) relative to those of bulk metallic Cu. At room temperature, no evidence is found of either Cu oxidation or Cu-Zn alloying.

Chapter 7: Summary

Overall, this dissertation contains two major results. First, we have extended studies of persistent free radical formation from phenol on metal oxides to the realm of surface science, examining phenol adsorption on single-crystal TiO_2(110) and Al_2O_3/NiAl(110) as reasonable model systems for the realistic titania and alumina powders on which most previous studies of radical formation and lifetime have occurred. We have attempted to maintain a connection with realistic environmental conditions by attempting to dose quantities of phenol (~10^6 L) at much higher pressures (~10^{-2} Torr) than we ordinarily would attempt in a UHV system, but have found through EELS and photoemission studies that both the titania and alumina surfaces are apparently passivated after the adsorption of a single phenol layer at room temperature, and show no evidence even of additional physisorbed phenol, let alone significant multilayer formation. With EELS, we have shown that there is a narrowing of the HOMO-LUMO gap in species adsorbed at 220°C compared to species adsorbed at room temperature or at 90 K, which we take to be a hallmark of a phenoxy radical as opposed to a chemisorbed phenol species. Vibrational spectra of phenol adsorbed at high temperature on alumina definitively shows that the high-temperature adsorption leaves the phenyl ring and C-O bonds intact. Photoemission studies of phenol/TiO_2(110) have directly shown charge transfer from adsorbed phenol into the TiO_2 surface, populating a state in the TiO_2 associated with surface oxygen vacancies, confirming for at least one case the proposed generic mechanism of radical formation by charge transfer to a metal oxide, locally reducing the oxide. Evidently, the accessibility of this well-characterized "defect" state facilitates the electron transfer and traps the resulting electron. In this case, UHV studies of materials using surface science techniques have led to an understanding of the fundamental processes involved in these radical formation reactions that experiments closer to

"realistic" conditions have not yet shown. Further studies of the geometry of phenol adsorption as a function of temperature by STM, LEED, and/or DFT would greatly deepen our understanding of the observed dependence of radical formation on adsorption temperature.

Second, we have shown that the *h*-BN nanomesh can act as a patterned substrate for Au nanoparticles of diameter 30 Å or less, with Au adatoms strongly preferring to bind in the nanomesh pores rather than on top of the wires, even after each pore is filled with clusters several atomic layers thick. The observed thickness of the Au clusters varies as a function of both temperature and total amount of Au deposited, with sub-ML dosages of Au deposited at 115 K showing a primarily single-layer cluster morphology, sub-ML dosages at room temperature showing a mixture of monolayer, bilayer, and a few even taller clusters, and multiple monolayers of Au demonstrating a reasonably broad range of cluster heights. XPS measurements have shown that single-layer clusters exhibit distinctly nonmetallic character due to the reduced dimensionality; strong final-state effects dominate the measured spectra, obscuring any influence that might come from charging of the nanoparticles, but spectra for larger doses of Au show evidence of both metallic character and positive charging, which is consistent with prior DFT studies of few-atom Au on *h*-BN. Although XPS shows no change in the Rh(111) substrate underlying the *h*-BN film after Au deposition, the Au morphology observed on *h*-BN/Rh(111) is different from that previously observed for *h*-BN/Ru(0001), implying that the degree of coupling between the clusters and the underlying metal can still exert some influence – so not only can the Au clusters not be considered in isolation of the *h*-BN, the Au/*h*-BN system cannot truly be considered isolated from the Rh(111). By way of contrast, we have observed that although Au on ZnO($10\,\bar{1}\,0$) shows a similar morphology to Au on *h*-BN/Rh(111) (nanometer-diameter single-layer islands), XPS results show that the Au on ZnO is *positively* charged, emphasizing again the

role of support effects in the preparation of catalytic systems. Cu on ZnO($10\bar{1}0$) also shows evidence of positive charging, but a 3D growth morphology and preferential nucleation sites even for very small coverages, even though both Cu/ZnO and Au/ZnO have been shown to be active for the hydrogenation of CO_2 to methanol – emphasizing, if nothing else, the idea that considering any one material property in isolation is clearly insufficient to explain any kind of catalytic behavior.

In terms of the work presented here on phenol/TiO_2 and phenol/alumina, an immediate hope is that it may serve as a guide for density functional calculations that may elucidate microscopic details of the mechanism of radical formation, including bonding geometries, transition states, and energetics. STM studies of adsorbed phenol as a function of temperature would also greatly add to our understanding of bonding geometries, and in the case of phenol/TiO_2 could potentially determine whether electrons transferred to the titania are trapped and localized. Furthermore, similar surface science studies could be performed on other oxides of interest – Fe_2O_3, NiO, and CuO are all environmentally relevant, and have their own unique properties that may play a role in the formation of EPFRs.

Having shown that well-dispersed, nanosized, negatively charged Au clusters may be supported on the *h*-BN nanomesh, the natural question to ask is whether they show any adsorption of CO, as CO oxidation is one of the reactions of interest that motivated this study. The adsorption of probe molecules would also itself help to confirm the charge state of the nanoclusters by measuring any shift in its intrinsic vibrational modes after adsorption on the nanoparticles. Studies of Au on *h*-BN on a variety of other transition metals would also provide better insight into metal substrate's effects on nanoparticle morphology and charge state, as the differences between Au/*h*-BN/Ru(0001) and Au/*h*-BN/Rh(111) have hinted may be considerable.

References

[1] P. Neta and R. H. Schuler, Radiation Research **64**, 233 (1975).

[2] P. Neta and R. H. Schuler, J. Am. Chem. Soc. **97**, 912 (1975).

[3] P. Neta and R. W. Fessenden, J. Phys. Chem. **78**, 523 (1974).

[4] P. W. Cains, L. J. McCausland, A. R. Fernandes, and P. Dyke, Environ. Sci. Technol. **31**, 776 (1997).

[5] T. Takasuga, T. Makino, K. Tsubota, and N. Takeda, Chemosphere **40**, 1003 (2000).

[6] S. Nganai, S. Lomnicki, and B. Dellinger, Environ. Sci. Technol. **43**, 368 (2009).

[7] S. Lomnicki, H. Truong, and B. Dellinger, Chemosphere **73**, 629 (2008).

[8] S. Nganai, S. M. Lomnicki, and B. Dellinger, Environ. Sci. Technol. **45**, 1034 (2011).

[9] G. R. Farquar, S. Alderman, E. Poliakoff, and B. Dellinger, Environ. Sci. Technol. **37**, 931 (2003).

[10] S. Lomnicki, H. Truong, E. Vejerano, and B. Dellinger, Environ. Sci. Technol. **42**, 4982 (2008).

[11] E. Vejerano, S. Lomnicki, and B. Dellinger, Environ. Sci. Technol. **45**, 589 (2011).

[12] L. Khachatryan, E. Vejerano, S. Lomnicki, and B. Dellinger, Environ. Sci. Technol. **45**, 8559 (2011).

[13] L. Khachatryan and B. Dellinger, Environ. Sci. Technol. **45**, 9232 (2011).

[14] B. Fahmy, L. Ding, D. You, S. Lomnicki, B. Dellinger, and S. A. Cormier, Environmental Toxicology and Pharmacology **29**, 173 (2010).

[15] S. Balakrishna, S. Lomnicki, K. M. McAvey, R. B. Cole, B. Dellinger, and S. A. Cormier, Particle and Fibre Toxicology **6**, 11 (2009).

[16] W. S. Seames, Fuel Processing Technology **81**, 109 (2003).

[17] S. L. Alderman, G. R. Farquar, E. D. Poliakoff, and B. Dellinger, Environ. Sci. Technol. **39**, 7396 (2005).

[18] S. Lomnicki and B. Dellinger, J. Phys. Chem. A **107**, 4387 (2003).

[19] U. Diebold, Surface Science Reports **48**, 53 (2003).

[20] J. A. Kelber, Surface Science Reports **62**, 271 (2007).

[21] B. Hammer and J. K. Nørskov, Nature **376**, 238 (1995).

[22] M. Valden, X. Lai, and D. W. Goodman, Science **281**, 1647 (1998).

[23] M. Haruta, Catalysis Today **36**, 153 (1997).

[24] M. Haruta, N. Yamada, T. Kobayashi, and S. Ijima, Journal of Catalysis **115**, 301 (1989).

[25] M. Haruta, S. Tsubota, T. Kobayashi, H. Kageyama, M. J. Genet, and B. Delmon, Journal of Catalysis **144**, 175 (1993).

[26] D. W. Goodman, Catal Lett **99**, 1 (2005).

[27] N. Spiridis, R. P. Socha, B. Handke, J. Haber, M. Szczepanik, and J. Korecki, Catalysis Today **169**, 24 (2011).

[28] M. Amft and N. V. Skorodumova, Phys. Rev. B **81**, 195443 (2010).

[29] J. Guzman and B. C. Gates, J. Am. Chem. Soc. **126**, 2672 (2004).

[30] Z. Yang, R. Wu, Q. Zhang, and D. Goodman, Phys. Rev. B **65**, 155407 (2002).

[31] X.-Q. Gong, A. Selloni, O. Dulub, P. Jacobson, and U. Diebold, J. Am. Chem. Soc. **130**, 370 (2008).

[32] L. Vilhelmsen and B. Hammer, Phys. Rev. Lett. **108**, 126101 (2012).

[33] S. Z. Butler, S. M. Hollen, L. Cao, Y. Cui, J. A. Gupta, H. R. Gutiérrez, T. F. Heinz, S. S. Hong, J. Huang, A. F. Ismach, E. Johnston-Halperin, M. Kuno, V. V. Plashnitsa, R. D. Robinson, R. S. Ruoff, S. Salahuddin, J. Shan, L. Shi, M. G. Spencer, M. Terrones, W. Windl, and J. E. Goldberger, ACS Nano **7**, 2898 (2013).

[34] L. Semidey-Flecha, D. Teng, B. F. Habenicht, D. S. Sholl, and Y. Xu, J. Chem. Phys. **138**, 184710 (2013).

[35] L. Liu, Z. Zhou, Q. Guo, Z. Yan, Y. Yao, and D. W. Goodman, Surface Science **605**, L47 (2011).

[36] B. Wang and M.-L. Bocquet, J. Phys. Chem. Lett. 2341 (2011).

[37] Q. Liao, H. J. Zhang, K. Wu, H. Y. Li, S. N. Bao, and P. He, Nanotechnology **22**, 125303 (2011).

[38] Y. Xu, L. Semidey-Flecha, L. Liu, Z. Zhou, and D. Wayne Goodman, Faraday Discuss. **152**, 267 (2011).

[39] Z. Zhou, F. Gao, and D. W. Goodman, Surface Science **604**, L31 (2010).

[40] O. V. Yazyev and A. Pasquarello, Phys. Rev. B **82**, 045407 (2010).

[41] C. Oshima and A. Nagashima, J. Phys.: Condens. Matter **9**, 1 (1999).

[42] A. H. Castro Neto, N. M. R. Peres, K. S. Novoselov, and A. K. Geim, Rev. Mod. Phys. **81**, 109 (2009).

[43] Z. Sun, S. K. Hämäläinen, J. Sainio, J. Lahtinen, D. Vanmaekelbergh, and P. Liljeroth, arXiv **cond-mat.mtrl-sci**, (2010).

[44] A. Preobrajenski, M. Ng, A. Vinogradov, and N. Mårtensson, Phys. Rev. B **78**, (2008).

[45] M. C. Wu, Q. Xu, and D. W. Goodman, J. Phys. Chem. **98**, 5104 (1994).

[46] A. Nagashima, N. Tejima, Y. Gamou, T. Kawai, and C. Oshima, Phys. Rev. Lett. **75**, 3918 (1995).

[47] W. Auwärter, T. J. Kreutz, T. Greber, and J. Osterwalder, Surface Science **429**, 229 (1999).

[48] M. Corso, W. Auwärter, M. Muntwiler, A. Tamai, T. Greber, and J. Osterwalder, Science **303**, 217 (2004).

[49] A. Goriachko, He, M. Knapp, H. Over, M. Corso, T. Brugger, S. Berner, J. Osterwalder, and T. Greber, Langmuir **23**, 2928 (2007).

[50] R. Laskowski, P. Blaha, T. Gallauner, and K. Schwarz, Phys. Rev. Lett. **98**, 106802 (2007).

[51] Y. Shi, C. Hamsen, X. Jia, K. K. Kim, A. Reina, M. Hofmann, A. L. Hsu, K. Zhang, H. Li, Z.-Y. Juang, M. S. Dresselhaus, L.-J. Li, and J. Kong, Nano Lett. **10**, 4134 (2010).

[52] P. Sutter, J. Lahiri, P. Albrecht, and E. Sutter, ACS Nano **5**, 7303 (2011).

[53] A. B. Preobrajenski, M. A. Nesterov, M. L. Ng, A. S. Vinogradov, and N. Mårtensson, Chemical Physics Letters **446**, 119 (2007).

[54] A. Goriachko, Y. B. He, and H. Over, J. Phys. Chem. C **112**, 8147 (2008).

[55] M. L. Ng, A. B. Preobrajenski, A. S. Vinogradov, and N. Mårtensson, Surface Science **602**, 1250 (2008).

[56] J. Zhang, V. Sessi, C. Michaelis, I. Brihuega, J. Honolka, K. Kern, R. Skomski, X. Chen, G. Rojas, and A. Enders, Phys. Rev. B **78**, 165430 (2008).

[57] I. Brihuega, C. H. Michaelis, J. Zhang, S. Bose, V. Sessi, J. Honolka, M. Alexander Schneider, A. Enders, and K. Kern, Surface Science **602**, L95 (2008).

[58] F. Wang, Structural and Electronic Properties of Noble Metals on Metal Oxide Surfaces, Louisiana State University, 2011.

[59] M. C. Patterson, X. Nie, F. Wang, R. L. Kurtz, S. B. Sinnott, A. Asthagiri, and P. T. Sprunger, J. Phys. Chem. C **117**, 18386 (2013).

[60] H. Ibach, *Physics of Surfaces and Interfaces* (Springer, Berlin; New York, 2006).

[61] P. Hofmann, *Surface Physics: an Introduction* (Philip Hofmann, 2013).

[62] Omicron NanoTechnology GmbH, editor, *VT STM XA / QPlus User's Guide*, 3rd ed. (2008).

[63] J. Tersoff and D. R. Hamann, Phys. Rev. Lett. **50**, 1998 (1983).

[64] E. Merzbacher, *Quantum Mechanics*, 3rd ed. (John Wiley & Sons, Inc., New York, 1998).

[65] E. W. Plummer and W. Eberhardt, in *Advances in Chemical Physics* (John Wiley & Sons, Inc., Hoboken, NJ, USA, 1982), pp. 533–656.

[66] S. Hüfner, editor, *Very High Resolution Photoelectron Spectroscopy* (Springer Berlin Heidelberg, Berlin, Heidelberg, 2007).

[67] Omicron NanoTechnology GmbH, editor, *DAR 400 & XM 1000: Sources for X-Ray Photoelectron Spectroscopy* (2011).

[68] A. C. Thompson and D. Vaughan, editors, *X-Ray Data Booklet*, 2nd ed. (Lawrence Berkeley National Laboratory, Berkeley, CA 94720, 2001).

[69] O. Kizilkaya, R. W. Jiles, M. C. Patterson, C. A. Thibodeaux, E. D. Poliakoff, P. T. Sprunger, R. L. Kurtz, and E. Morikawa, J. Phys.: Conf. Ser. **493**, 012024 (2014).

[70] C. A. McFerrin, R. W. Hall, and B. Dellinger, Journal of Molecular Structure: THEOCHEM **848**, 16 (2008).

[71] A. L. N. dela Cruz, W. Gehling, S. Lomnicki, R. Cook, and B. Dellinger, Environ. Sci. Technol. **45**, 6356 (2011).

[72] R. M. Jaeger, H. Kuhlenbeck, H.-J. Freund, M. Wuttig, W. Hoffmann, R. Franchy, and

H. Ibach, Surface Science **259**, 235 (1991).

[73] M. Yoshitake, B. Mebarki, and T. Lay, Surface Science **511**, L313 (2002).

[74] W. Song and M. Yoshitake, Applied Surface Science **241**, 164 (2005).

[75] S. C. Street, Q. Guo, C. Xu, and D. W. Goodman, J. Phys. Chem. **100**, 17599 (1996).

[76] T. Ari, H. Güven, and N. Ecevit, Journal of Electron Spectroscopy and Related Phenomena **73**, 13 (1995).

[77] R. M. Silverstein, G. C. Bassler, and T. C. Morrill, *Spectrometric Identification of Organic Compounds*, 5 ed. (John Wiley & Sons, Inc., New York, 1991).

[78] Z.-Y. Chen, Y. Hu, T.-C. Liu, C.-L. Huang, and T.-S. Jeng, Thin Solid Films **517**, 4998 (2009).

[79] P. Persson, R. Bergström, and S. Lunell, J. Phys. Chem. B **104**, 10348 (2000).

[80] A. L. Linsebigler, G. Lu, and J. T. Yates, Chem. Rev. **95**, 735 (1995).

[81] T. L. Thompson and J. T. Yates, Chem. Rev. **106**, 4428 (2006).

[82] B. O'Regan and M. Grätzel, Nature **353**, 737 (1991).

[83] K. L. Syres, A. G. Thomas, W. R. Flavell, B. F. Spencer, F. Bondino, M. Malvestuto, A. Preobrajenski, and M. Grätzel, J. Phys. Chem. C **116**, 23515 (2012).

[84] S.-C. Li, J.-G. Wang, P. Jacobson, X. Q. Gong, A. Selloni, and U. Diebold, J. Am. Chem. Soc. **131**, 980 (2009).

[85] L.-M. Liu, S.-C. Li, H. Cheng, U. Diebold, and A. Selloni, J. Am. Chem. Soc. **133**, 7816 (2011).

[86] S. C. Li, L. N. Chu, X. Q. Gong, and U. Diebold, Science **328**, 882 (2010).

[87] R. Sánchez-de-Armas, M. A. San-Miguel, J. Oviedo, A. Márquez, and J. F. Sanz, Phys. Chem. Chem. Phys. **13**, 1506 (2011).

[88] S.-C. Li, Y. Losovyj, and U. Diebold, Langmuir **27**, 8600 (2011).

[89] S. Rangan, J.-P. Theisen, E. Bersch, and R. A. Bartynski, Applied Surface Science **256**, 4829 (2010).

[90] S.-C. Li, Y. Losovyj, V. K. Paliwal, and U. Diebold, J. Phys. Chem. C **115**, 10173 (2011).

[91] S.-C. Li and U. Diebold, J. Am. Chem. Soc. **132**, 64 (2010).

[92] J. P. P. Ramalho and F. Illas, Chemical Physics Letters **501**, 379 (2011).

[93] E. Hebenstreit, W. Hebenstreit, H. Geisler, S. Thornburg, C. Ventrice, D. Hite, P. Sprunger, and U. Diebold, Phys. Rev. B **64**, (2001).

[94] A. Thomas, W. Flavell, A. Mallick, A. Kumarasinghe, D. Tsoutsou, N. Khan, C. Chatwin, S. Rayner, G. Smith, R. Stockbauer, S. Warren, T. Johal, S. Patel, D. Holland, A. Taleb, and F. Wiame, Phys. Rev. B **75**, 035105 (2007).

[95] C. Di Valentin, G. Pacchioni, and A. Selloni, Phys. Rev. Lett. **97**, 166803 (2006).

[96] E. Lira, J. Ø. Hansen, L. R. Merte, P. T. Sprunger, Z. Li, F. Besenbacher, and S. Wendt, Top Catal **56**, 1460 (2013).

[97] A. Lenz, M. Karlsson, and L. Ojamäe, J. Phys.: Conf. Ser. **117**, 012020 (2008).

[98] G. E. Muhlenberg, editor, *Handbook of X-Ray Photoelectron Spectroscopy* (Perkin-Elmer Corporation, 1979).

[99] U. Diebold and T. Madey, Surface Science Spectra **4**, (1996).

[100] J. Mayer, U. Diebold, T. Madey, and E. Garfunkel, Journal of Electron Spectroscopy and Related Phenomena **73**, 1 (1995).

[101] R. L. Kurtz, R. Stock-Bauer, T. E. Msdey, E. Román, and J. De Segovia, Surface Science **218**, 178 (1989).

[102] D. Brinkley, M. Dietrich, T. Engel, P. Farrall, G. Gantner, A. Schafer, and A. Szuchmacher, Surface Science **395**, 292 (1998).

[103] M. A. Henderson, Surface Science **355**, 151 (1996).

[104] A. Goriachko, A. A. Zakharov, and H. Over, J. Phys. Chem. C **112**, 10423 (2008).

[105] A. B. Preobrajenski, A. S. Vinogradov, and N. Mårtensson, Surface Science **582**, 21 (2005).

[106] R. Laskowski, P. Blaha, and K. Schwarz, Phys. Rev. B **78**, 045409 (2008).

[107] A. Preobrajenski, S. Krasnikov, A. Vinogradov, M. Ng, T. Käämbre, A. Cafolla, and N. Mårtensson, Phys. Rev. B **77**, 085421 (2008).

[108] R. Laskowski and P. Blaha, Phys. Rev. B **81**, 075418 (2010).

[109] A. Preobrajenski, A. Vinogradov, M. Ng, E. Ćavar, R. Westerström, A. Mikkelsen, E. Lundgren, and N. Mårtensson, Phys. Rev. B **75**, 245412 (2007).

[110] A. Preobrajenski, A. Vinogradov, and N. Mårtensson, Phys. Rev. B **70**, 165404 (2004).

[111] N. Lopez, T. V. W. Janssents, B. S. Clausen, Y. Xu, M. Mavrikakis, T. Bligaard, and J. K. Nørskov, Journal of Catalysis **223**, 232 (2004).

[112] L. Molina and B. Hammer, Phys. Rev. Lett. **90**, 206102 (2003).

[113] R. Laskowski and P. Blaha, J. Phys.: Condens. Matter **20**, 064207 (2008).

[114] A. T. N'Diaye, T. Gerber, C. Busse, J. Mysliveček, J. Coraux, and T. Michely, New J. Phys. **11**, 103045 (2009).

[115] B. F. Habenicht, D. Teng, L. Semidey-Flecha, D. S. Sholl, and Y. Xu, Top Catal **57**, 69 (2013).

[116] B. F. Habenicht, Y. Xu, and L. Liu, in *Theoretical Perspectives* (John Wiley & Sons, Ltd, Chichester, UK, 2013), pp. 425–446.

[117] H. P. Koch, R. Laskowski, P. Blaha, and K. Schwarz, Phys. Rev. B **84**, 245410 (2011).

[118] H. P. Koch, R. Laskowski, P. Blaha, and K. Schwarz, Phys. Rev. B **86**, 155404 (2012).

[119] R. Hwang, J. Schröder, C. Günther, and R. Behm, Phys. Rev. Lett. **67**, 3279 (1991).

[120] N. W. Ashcroft and N. D. Mermin, *Solid State Physics* (Saunders College, 1976).

[121] S. Doniach and M. Sunjic, Journal of Physics C: Solid State Physics **3**, 285 (1970).

[122] Y. Choi, K. Futagami, T. Fujitani, and J. Nakamura, Applied Catalysis a: General **208**, 163 (2001).

[123] T. Fujitani and J. Nakamura, Applied Catalysis a: General **191**, 111 (2000).

[124] H. Sakurai and M. Haruta, Applied Catalysis a: General **127**, 93 (1995).

[125] H. Sakurai and M. Haruta, Catalysis Today **29**, 361 (1996).

[126] J. Strunk, K. Kähler, X. Xia, M. Comotti, F. Schüth, T. Reinecke, and M. Muhler, Applied Catalysis a: General **359**, 121 (2009).

[127] O. Dulub, L. A. Boatner, and U. Diebold, Surface Science **504**, 271 (2002).

[128] K. Ozawa, T. Sato, Y. Oba, and K. Edamoto, J. Phys. Chem. C **111**, 4256 (2007).

[129] W. H. Doh, P. C. Roy, and C. M. Kim, Langmuir **26**, 16278 (2010).

[130] J. E. Houston, C. H. F. Peden, D. S. Blair, and D. W. Goodman, Surface Science **167**, 427 (1986).

[131] C. Wöll, Progress in Surface Science **82**, 55 (2007).

[132] G. Panzner, B. Egert, and H. P. Schmidt, Surface Science **151**, 400 (1985).

[133] G. Wertheim, S. DiCenzo, and S. Youngquist, Phys. Rev. Lett. **51**, 2310 (1983).

[134] H. M. Lee, M. Ge, B. R. Sahu, P. Tarakeshwar, and K. S. Kim, J. Phys. Chem. B **107**, 9994 (2003).

[135] S. A. Serapian, M. J. Bearpark, and F. Bresme, Nanoscale **5**, 6445 (2013).

[136] D. Shirley, Phys. Rev. B **5**, 4709 (1972).

Appendix A: Statements of Permission

Chapter 3 previously appeared as M. C. Patterson, N. D. Keilbart, L. W. Kiruri, C. A. Thibodeaux, S. Lomnicki, R. L. Kurtz, E. D. Poliakoff, B. Dellinger, and P. T. Sprunger, "EPFR formation from phenol adsorption on Al_2O_3 and TiO_2: EPR and EELS studies," Chemical Physics **422**, 277 (2013). It is reprinted by permission of Elsevier, per their Author Rights document (http://www.elsevier.com/journal-authors/author-rights-and-responsibilities): "Authors can use either their accepted author manuscript or final published article for… inclusion in a thesis or dissertation"

Chapter 6 previously appeared as M. C. Patterson, X. Nie, F. Wang, R. L. Kurtz, S. B. Sinnott, A. Asthagiri, and P. T. Sprunger, "Growth and Structure of Cu and Au on the Nonpolar $ZnO(10\bar{1}0)$ Surface," J. Phys. Chem. C **117**, 18386 (2013). It is reprinted by permission of the American Chemical Society per the Rightslink by Copyright Clearance Center service, "Permission for this particular request is granted for print and electronic formats, and translations, at no charge."

Appendix B: XPS Peak Fitting

It is worth briefly describing here the procedures used for background subtraction and peak fitting to experimentally obtained XPS data. The basis of the technique is the photoelectric effect – samples are irradiated with photons of a known energy, which causes electrons to be ejected from the sample with kinetic energies given by the relationship

$$KE = h\nu - BE - \Phi_A \qquad \text{(B.1)}$$

where $h\nu$ is the energy of the incident photon (here 1486.6 eV), and Φ_A is the analyzer work function, which is known. In this way, the binding energies of various different electronic states in materials can be determined by measuring the kinetic energies of ejected electrons. We may idealize the binding energies of electrons in a solid as infinitesimally sharp lines on top of a flat background, but many effects lead to both peak broadening and complicated backgrounds. One expects intrinsic broadening of peaks (usually assumed to be Lorentzian in nature) due to the lifetime of the core hole left behind after an electron is ejected; the width of the peak $\Delta E_{lifetime}$ varies inversely with the core hole lifetime according to the uncertainty principle. The energy resolution of the analyzer, $\Delta E_{analyzer}$, is determined by the experimenter and is usually taken to be Gaussian in nature; in general, one achieves higher energy resolution (but lower count rates, leading to much longer data acquisition times) by decreasing the analyzer pass energy and entrance/exit slit size. Finally, even a monochromatized X-ray source has some finite linewidth ΔE_{source}, which in the case of our system is a constant of 0.3 eV. In addition, XPS peaks are sometimes inherently asymmetric in nature – for metals, in particular, asymmetry is often observed due to the response of conduction electrons to the core hole [121], leading to the excitation of low-energy electron-hole pairs and resulting in a high binding energy "tail" on

metallic XPS peaks. The peaks observed in XPS thus represent convolutions of all these various effects, which must be taken into account when fitting data.

In the spectra presented below, all of the fitting and background removal has been done using the built-in tools in CasaXPS. For simplicity's sake, linear backgrounds have generally been subtracted from all spectra; this is typically not a bad approximation for insulating or semiconducting materials. Peaks from nonmetallic elements/samples have been fit using approximations to a Voigt lineshape, which is the convolution of a Gaussian (for broadening due to analyzer/source) and Lorentzian (for intrinsic linewidth) function. As there is no analytic form for the Voigt lineshape, CasaXPS approximates it with the user's choice of a weighted product or sum of Gaussian and Lorentzian peaks of the same width. We typically choose the Gaussian/Lorentzian product form:

$$GL(x,m,E,F) = \frac{\exp\left[-4\ln 2(1-m)\frac{(x-E)^2}{F^2}\right]}{1+4m\frac{(x-E)^2}{F^2}} \qquad \text{(B.2)}$$

In each case, E is the energy of the center of the peak, and F is the width (both of which are usually free parameters) and the parameter m controls mixing – $m = 0$ corresponds to a pure Gaussian in both cases, $m = 1$ to a pure Lorentzian. Metallic peaks displaying inherent asymmetry are fit with a Doniach-Sunjic lineshape [121] numerically convoluted with a Gaussian/Lorentzian product, which is a reasonable approximation to the "true" lineshape.

Background subtraction can be handled in a variety of different ways. For materials that are relatively insulating (or at least possess some reasonable band gap, such as ZnO), a reasonable assumption is that the background intensity does not vary significantly over the region one wishes to fit a peak, and so the subtraction of a linear background from the peak-fitting region is a valid and easily implemented approximation to the "true" background shape.

Another approach is given by Shirley and carries his name [136]. The background is assumed to originate from valence band electrons inelastically scattered within the material before leaving the sample. The correction has the shape of a smoothed step function, where the "step" falls at or near the center of the peak of interest, and is calculated by subtracting from the measured spectrum at every point a quantity proportional to the integrated area under the spectrum up to that point. (Typically, start and end points are set at relatively "flat" portions of the background before and after peaks of interest.) This iterative process is still relatively simple to implement in software, but sometimes fails or returns unphysical results if the data set is particularly noisy (i.e. the integrated areas are small and change sign rapidly). This has the effect of reducing or entirely removing some kinds of asymmetry in XPS peaks, so the experimenter needs to take care if, as in Chapters 5 and 6, the asymmetry of fitted peaks carries some information about the physics of the system.

Vita

Matthew Patterson is a native of Baton Rouge, Louisiana. He received a Bachelor of Arts in Physics from Rice University in Houston, Texas in 2007. He entered Louisiana State University in 2007 to pursue the Ph. D. in physics.